UNIVERSIDADE FEDERAL DO RIO GRANDE DO SUL

PROGRAMA DE PÓS-GRADUAÇÃO EM FÍSICA

Ion implantation and ion irradiation effects on nuclear and thermoelectric materials

Mariana de Mello Timm

Porto Alegre, July 2019.

UNIVERSIDADE FEDERAL DO RIO GRANDE DO SUL

INSTITUTO DE FÍSICA

PROGRAMA DE PÓS-GRADUAÇÃO EM FÍSICA

Ion implantation and ion irradiation effects on nuclear and thermoelectric materials[1]

Mariana de Mello Timm

Thesis submitted to *Programa de Pós-Graduação em Física* at *Universidade Federal do Rio Grande do Sul* as a partial requirement for the degree of Doctor of Sciences

Supervisor: Prof. Dr. Paulo Fernando Papaléo Fichtner

Porto Alegre, July 2019.

[1] This work was financially supported by *Conselho Nacional de Desenvolvimento Científico e Tecnológico* (CNPq) and *Coordenação de Aperfeiçoamento de Pessoal de Nível Superior* (CAPES) – Finance Code 001

In memory of my father, Celso

Acknowledgements

I would like to express my deep gratitude to my supervisor, Prof. Paulo Fichtner, for his patient guidance, enthusiastic encouragement and useful critiques of this research work. His guidance helped me in all the time of research and writing of this thesis. I could not have imagined having a better supervisor and mentor for my Ph.D. study.

I would also like to express my great appreciation to Dr. Erwan Oliviero, without whom my internship in France would not have been possible. Thank you for finding me a place in the lab in Montpellier, for teaching me how to use the TEM and for always showing your positive outlook and confidence in my research and academic skills.

I am extremely grateful to Prof. Nicole Fréty, for her valuable guidance and encouragement. I appreciate her contributions of time and ideas to make our work productive and stimulating. Thank you for accepting me as your student and for making our collaboration a very fruitful one.

My sincere thanks also goes to all the technicians at the Ion Implantation Laboratory, especially Agostinho, Miro, Leandro and Kovalick, whose willingness (and patience) to help the students with all our complicated experiments is beyond measure.

I would especially like to thank Fabrice, Fred, Martine and Véro for all their *gentilesse* with me. My short period in France would not have been so special without your everyday company. *Merci beaucoup*!

I thank my fellow labmates Bárbara, Ítalo, Gabriel, Francine, Franciele, Matheus, Willian, Juliana and Zacarias for the stimulating discussions, for all the help with the experimental procedures and, more importantly, for the companionship during the last four years.

My special thanks goes also to Felipe, Amanda, Vinícius, Lucas, Rafael, Demétrius and Stock, friends that "physics" gave me ten years ago and whose friendship made all these years a lot more pleasant. I must also give a sincere thanks to Amanda, for being the Best Frau Forever. And to Felipe, who has always been there during the best and worst times.

Finally, I am also extremely grateful to my mother, Ana, and my brothers, Daniel and Celso, for their love and support throughout all these years.

Abstract

In this thesis the study of ion implantation and ion irradiation effects on microstructure and physical properties of nuclear and thermoelectric materials will be presented. Materials that are constantly exposed to radiation in nuclear reactor cores present serious degradation of their mechanical properties, especially to corrosion and swelling. The damage created by neutron irradiation in these materials can be simulated by ion irradiation. On the other hand, the enhancement of the figure of merit of thermoelectric materials can be achieved with the tailoring of the electrical and heat transport properties of semiconductors. In this case, ion implantation can be used to introduce electrically active defects or dopants that will increase the electrical conductivity or to generate interfaces that will serve as scattering centers for the phonons, reducing the thermal conductivity. The present work investigates the ion irradiation effects on the nucleation and growth of cavities, Ar bubbles and on the evolution of precipitate phases in solution-annealed AISI 316L austenitic stainless steels alloys and the ion implantation effects on microstructure and electrical resistivity of chromium (di)silicide ($CrSi_2$) amorphous thin films.

Within the nuclear material study, thin, polished and solution-annealed AISI 316L samples were implanted with Ar *plateau* and then annealed to accelerate the Ar bubble nucleation. Then, along with control samples without Ar, they were irradiated with 5 MeV Au ions at 550 ºC at two different ion fluxes. Another identical set of samples was irradiated with 3.5 MeV Ag ions at 550 ºC. The irradiation experiments were performed until they achieved irradiation fluences equivalent to damage levels of ≈ 20 and 40 dpa. The results show that the precipitation of $M_{23}C_6$ and MC carbide phases and Ar bubble growth is directly related to the vacancy saturation in the matrix. Regarding the thermoelectric material study, Al and Ne ion implantations were performed in 280 nm thick $CrSi_2$ samples. Al implantations were conducted to achieve two ion concentrations, one of 0.008 at.% and the other one of 0.64 at.%, conducted to equal the damage level produced by Ne implantation. Room temperature Al and Ne implantations induced the decrease in electrical resistivity, while Ne and Al (0.64 at. %) implantations held at 250 ºC resulted in a significant increase in electrical resistivity. The results show a strong relation to the level of damage induced by ion implantation.

For all the studies, the samples were characterized via Transmission Electron

Microscopy (TEM), Selected Area Diffraction (SAD) and Energy Dispersive X-Ray Spectroscopy (EDX).

Resumo

Nesta tese serão apresentados os estudos relativos aos efeitos da implantação e da irradiação iônica sobre a microestrutura e propriedades físicas de materiais nucleares e termoelétricos. Materiais que estão constantemente expostos à radiação em reatores nucleares apresentam uma séria degradação de suas propriedades mecânicas, principalmente devido à corrosão e inchaço. Os danos gerados pela irradiação de nêutrons nesses materiais podem ser simulados por irradiação iônica. Por outro lado, o melhoramento da figura de mérito dos materiais termoelétricos pode ser obtido através da manipulação das propriedades de transporte elétrico e térmico dos semicondutores. Neste caso, a implantação iônica pode ser usada para introduzir defeitos eletricamente ativos ou dopantes que aumentarão a condutividade elétrica ou para produzir interfaces que servirão como centros espalhadores para os fônons, diminuindo a condutividade térmica. Este trabalho apresenta uma investigação sobre os efeitos da irradiação de íons na nucleação e crescimento de cavidades, bolhas de Ar e evolução de fases precipitadas em ligas solubilizadas de aço austenítico AISI 316L e também uma investigação sobre os efeitos da implantação de íons na microestrutura e resistividade elétrica em filmes amorfos de (di)siliceto de cromo ($CrSi_2$).

No estudo do material nuclear, amostras de AISI 316L solubilizado foram implantadas com um *plateau* de Ar e recozidas para acelerar o processo de nucleação de bolhas de Ar. Então, juntamente a amostras-controle sem Ar, foram irradiadas com íons e Au de 5 MeV de energia a 550 ºC sob dois fluxos de irradiação diferentes. Outr conjunto idêntico de amostras foi irradiado com íons de Ag de 3.5 MeV de energia a 550 ºC. Os experimentos de irradiação foram conduzidos até fluências equivalentes a níveis de dano de ≈ 20 e 40 dpa. Os resultados mostram que a precipitação de carbetos do tipo $M_{23}C_6$ e MC e o crescimento de bolhas de Ar estão diretamente relacionados à saturação de vacâncias na matriz. Em relação ao estudo do material termoelétrico, implantações de íons de Al e Ne foram realizadas em filmes de $CrSi_2$ de 280 nm de espessura. Duas implantações de íons de Al foram realizadas, uma atingindo uma concentração de 0.008 at.% de Al e outra de 0.64 at.% de Al, realizada para igualar o nível de dano produzido pela implantação de íon de Ne. As implantações de Ne e Al conduzidas a temperatura ambiente induziram a diminuição da resistividade elétrica do CrSi2, enquanto as implantações de Ne e Al (0.64 at.%) realizadas a 250 ºC resultaram

num aumento significativo da resistividade elétrica. Os resultados mostram uma forte relação com o nível de dano induzido por implantação iônica.

Para todos os estudos, as amostras foram analisadas com as técnicas de Microscopia Eletrônica de Transmissão (MET), Difração de Área Selecionada (SAD) e Espectroscopia de raios X por dispersão em energia (EDX).

Contents

CHAPTER 1

Introduction

The increasing demand for technologies capable of delivering a large amount of clean energy has boosted the development of several scientific areas, such as the research of photovoltaic cells and batteries for the capture and storing of solar and wind power, as well as research related to the development of efficient materials for nuclear fusion and thermoelectricity. In fact, besides from the publicity given to the several latest enhancements of semiconductor materials that are critical to photovoltaics engineering, some important advances in less-known technologies have still not reached the public eye. Thermoelectric materials *i.e.*, materials that can transform heat into electricity, for example, are timidly attracting renewed scientific interest after the achievement of promising results with the increase of thermoelectric properties in low-cost and low or non-toxic materials such as polymers and oxide-based compounds [1–3].

Thermoelectricity can have a key role on the harnessing of the waste energy produced in power plants of any kind. In the energy conversion process, there will always be an amount of energy that will be wasted. In some cases, the efficiency of energy conversion processes, like in solar cell systems, may range from 6 to 40%. Natural gas has an average efficiency of 50% while coal produces energy at almost 59%. Wind power operates with 32% efficiency. On the other hand, hydroelectric and nuclear powers have an average capacity factor of 90% [4]. In most energy conversion systems, energy will be wasted in the form of heat. This fact has spurred electricity generation industries, for example, to consider new technologies for the recovery of waste heat. In this sense, thermoelectricity can offer an advantageous means of transforming heat into electricity mainly because thermoelectric devices are small, with no moving parts (thus requiring low maintenance), and they also have long life and reliability [5,6]. Nevertheless, thermoelectricity has remained a niche technology, since it is still considered to be too inefficient and costly for large-scale applications. Since

the efficiency of thermoelectric devices relies mostly on the kind of materials used in their fabrication, the search for the optimization of thermoelectric properties in either conventional thermoelectric materials, such as PbTe and Bi_2Te_3, as in new ones, such as skutterudites, clathrates and half-Heusler compounds, has dominated this domain of study in the last few years [7,8]. Furthermore, all the advances in the manufacture of high performance nanostructured materials that occurred in the last few decades have presented a new path to be explored on the enhancement of materials for their use in the technologies that aim to produce and recover energy in a more efficient while still sustainable way.

In the wake of the new efforts to combat the emission of CO_2 and to cut off the use of fossil fuels and other non-renewable natural resources, nuclear fission has remained as the least popular, most controversial and most feared means of attaining the goal of clean energy production.

Despite the intense debate over nuclear waste and fears of major environmental disasters such as those at Chernobyl and Fukushima, large-scale nuclear reactor power generation remains one of the most efficient and safest in the world [9,10]. Indeed, accidents with nonnuclear power plants can be as detrimental to the environment and human health as the leaking of radiation from nuclear power plants. Major accidents caused by the rupture of hydroelectric dams, for example, have occurred in China, USA and Italy, causing the death of hundreds of people and the destruction of terrestrial and aquatic biodiversity for several hundreds of kilometers [11–13]. Furthermore, a large investment in the expansion of solar and wind farms could also bring environmental impacts to vast areas of forest and farmland.

It is clear, however, that nuclear technology has still many features that need to be refined. The common nuclear power plants that are built nowadays require about 20.5 km^2 of land to accommodate the nuclear power station itself, its exclusion zone, its enrichment plant, ore processing, and supporting infrastructure. Nuclear reactors need to be located near a massive body of coolant water, but away from dense population zones and natural disaster zones. Furthermore, most of the power plants need to be decommissioned after around 60 years of use due to the swelling and creep caused in the materials exposed to radiation inside the plant [14]. Indeed, the need to transform this type of energy generation into something more viable in both the environmental and

economic bias has led to a major breakthrough in the production of Small Modular Reactors (SMR), which generally work from the same mechanisms as a large power plant, but require less infrastructure for their construction and offer more efficiency in containment mechanisms [15]. In this way, the improvement of nuclear technology is increasingly sought through an in-depth study of the effects that the high dose of radiation can cause on the materials of the reactor and the search for ways to limit the damage caused by irradiation.

The aim of this thesis is to study the mechanisms governing defect formation and evolution under ion implantation and irradiation and its effects on the microstructure and physical properties of materials used in thermoelectric and nuclear technologies. Besides the fact that both technologies are used for energy generation, these subjects seem to have little in common, since the materials used in nuclear fuel clad applications (mostly stainless steels and zirconium alloys) function in a quite different manner than those used in thermoelectric application (mostly semiconductors). However, these two technologies have been shown to work especially well together. The Radioisotope Thermoeletric Generators (RTGs) are electrical generators with no moving parts composed by an array of thermocouples that convert the heat released by the decay of a radioactive material into electricity by the Seebeck effect. Such generators can provide long-life power sources in harsh or inaccessible environments, as in satellites or space-probes. In fact, these RTGs have been used by NASA in missions on the Moon (they powered the scientific experiments left on the Moon by the crews of Apollo 12 through 17), on Mars (in the two Viking landers) and in outer-planetary explorations (in Pioneer 10, Pioneer 11, Voyager 1, Voyager 2, Galileo, Ulysses, Cassini, New Horizons space-probes), where energy supply by solar panels were impractical [16,17]. RTGs were also used in remote arctic monitoring sites.

With all the possibilities provided by these two technologies, either in combined or in isolated applications, it is of great importance to deeply understand how the materials involved in the energy generation processes respond to experiments that aim to enhance their physical characteristics and/or solve intrinsic problems. In this sense, ion implantation and ion irradiation are powerful techniques that can be employed in the study of both thermoelectric and nuclear materials. In thermoelectric materials, experiments with energetic ions can be used to change the charge carrier concentration

and increase the electrical conductivity and to introduce point and extended defects that will serve as scattering centers, thus reducing the phonon contribution to thermal conductivity [18–21]. In nuclear materials, energetic ions can be used as a simpler way to simulate neutron irradiation, since it is possible to induce the formation of the same structural defects (extended defects, bubbles and precipitates) formed by the intense radiation of neutrons and other particles in the materials that are in contact with the fuel rods. These defects are known to impair the mechanical properties of the material, generating swelling and mechanically weakening the material, with consequent decrease in the useful life of the part [22–25].

The present thesis encompasses the use of ion implantation and ion irradiation techniques to induce microstructural changes in both thermoelectric and nuclear materials and analyze how these changes can affect their physical properties. A study of the microstructural changes induced by ion implantation in $CrSi_2$ semiconductor thin films and their consequences on the electrical resistivity of this promising thermoelectric material is realized. The formation of inert gas bubbles is also attempted as a mean to reduce the heat conductivity, a necessary feature to improve the thermoelectric conversion efficiency. In the case of nuclear materials, the formation and growth of inert gas bubbles is a deleterious effect connected to embrittlement and swelling. Ion irradiation effects are also studied in connection to the formation of precipitate systems in AISI 316L austenitic stainless steel matrix. For both studies, several experiments were carried out covering different implantation/irradiation parameters, such as the ion species used, implantation/irradiation fluence and implantation/irradiation flux.

This thesis will be structured as follows: Chapter 2 presents an account about the main aspects of nuclear and thermoelectric materials while Chapter 3 will focus on the theoretical basis of ion-solid interactions. In Chapter 4, the experimental techniques and procedures used in this work will be presented. Chapter 5 shows the results and discussions regarding the formation and growth of bubbles and the formation and identification of precipitates in AISI 316L. In Chapter 6, it will be presented the results about ion implantation experiments in $CrSi_2$ thin films. Finally, Chapter 7 will present the conclusion about the studies previously discussed.

References

[1] R. Santos, A. Yamini, Recent progress in magnesium-based thermoelectric materials, J. Mater. Chem. A. 6 (2018) 3328–3341. doi:10.1039/c7ta10415d.

[2] H. Yao, Z. Fan, H. Cheng, X. Guan, C. Wang, K. Sun, Recent Development of Thermoelectric Polymers and Composites, Macromol. Rapid Commun. 39 (2018) 1–22. doi:10.1002/marc.201700727.

[3] A. Nozariasbmarz, A. Agarwal, Z.A. Coutant, M.J. Hall, J. Liu, R. Liu, A. Malhotra, P. Norouzzadeh, C. Ozturk, V.P. Ramesh, Y. Sargolzaeiaval, F. Suarez, D. Vashaee, Thermoelectric silicides : A review, Jpn. J. Appl. Phys. 56 (2017).

[4] Energy Conversion Efficiency, https://en.wikipedia.org/wiki/Energy_conversion_efficiency (accessed May 14, 2019).

[5] B. Orr, A. Akbarzadeh, Prospects of waste heat recovery and power generation using thermoelectric generators, Energy Procedia. 110 (2017) 250–255. doi:10.1016/j.egypro.2017.03.135.

[6] E. Koukharenko, J. Kuleshova, M. Fowler, A. Ali, Y. Chen, V. Vasiraju, Towards a nanostructured thermoelectric generator using ion-track lithography, J. Micromech. Microeng. 18 (2008). doi:10.1088/0960-1317/18/10/104015.

[7] G.J. Snyder, E.S. Toberer, Complex thermoelectric materials, Nat. Mater. 7 (2008) 105–114.

[8] H. Zhu, J. Mao, Y. Li, J. Sun, Y. Wang, Q. Zhu, G. Li, Q. Song, J. Zhou, Y. Fu, R. He, T. Tong, Z. Liu, W. Ren, L. You, Z. Wang, J. Luo, A. Sotnikov, J. Bao, K. Nielsch, G. Chen, D.J. Singh, Z. Ren, Discovery of TaFeSb-based half-Heuslers with high thermoelectric performance, Nat. Commun. (2019) 1–8. doi:10.1038/s41467-018-08223-5.

[9] J.S. Goldstein, S.A. Qvist, Only Nuclear Energy Can Save the Planet, Wall Str. J.

(2019) 1–4.

[10] B.W. Brook, A. Alonso, D.A. Meneley, J. Misak, T. Blees, J.B. Van Erp, Why nuclear energy is sustainable and has to be part of the energy mix, Sustain. Mater. Technol. 1–2 (2014) 8–16. doi:10.1016/j.susmat.2014.11.001.

[11] Banqiao Dam, (n.d.). https://en.wikipedia.org/wiki/Banqiao_Dam (accessed May 21, 2019).

[12] Val di Stava dam collapse, (n.d.). https://en.wikipedia.org/wiki/Val_di_Stava_dam_collapse (accessed May 21, 2019).

[13] South Fork Dam, (n.d.). https://en.wikipedia.org/wiki/South_Fork_Dam (accessed May 21, 2019).

[14] D. Abbott, Is Nuclear Power Globally Scalable?, Proc. IEEE. 99 (2011).

[15] IAEA, Status of Small Reactor Designs Without On-Site Refuelling, 2007.

[16] Power and Thermal Systems, (n.d.). https://rps.nasa.gov/power-and-thermal-systems/power-systems/current/ (accessed May 21, 2019).

[17] Radioisotope Thermoelectric Generator,. https://en.wikipedia.org/wiki/Radioisotope_thermoelectric_generator#Terrestrial (accessed May 16, 2019).

[18] D. Haase, M. Schmid, W. Kürner, A. Dörnen, V. Härle, F. Scholz, M. Burkard, H. Schweizer, Deep-level defects and n-type-carrier concentration in nitrogen implanted GaN, Appl. Phys. Lett. 69 (1996) 2525–2527. doi:10.1063/1.117727.

[19] S.C. Binari, H.B. Dietrich, G. Kelner, L.B. Rowland, K. Doverspike, D.K. Wickenden, H, He, and N implant isolation of n-type GaN, J. Appl. Phys. 78 (2002) 3008–3011. doi:10.1063/1.360712.

[20] S.O. Kucheyev, H. Boudinov, J.S. Williams, C. Jagadish, G. Li, Effect of irradiation temperature and ion flux on electrical isolation of GaN, J. Appl. Phys. 91 (2002) 4117–4120. doi:10.1063/1.1455154.

[21] N. Tureson, M. Marteau, T. Cabioch, N. Van Nong, J. Jensen, J. Lu, G. Greczynski, D. Fournier, N. Singh, A. Soni, L. Belliard, P. LEklund, A. e Febvrier, Effect of ion-implantation-induced defects and Mg dopants on the thermoelectric properties of ScN, Phys. Rev. B. 98 (2018) 1–9. doi:10.1103/physrevb.98.205307.

[22] G.S. Was, Z. Jiao, E. Getto, K. Sun, A.M. Monterrosa, S.A. Maloy, O. Anderoglu, B.H. Sencer, M. Hackett, Emulation of reactor irradiation damage using ion beams, Scr. Mater. 88 (2014) 33–36. doi:10.1016/j.scriptamat.2014.06.003.

[23] Z. Jiao, G.S. Was, Novel features of radiation-induced segregation and radiation-induced precipitation in austenitic stainless steels, Acta Mater. 59 (2011) 1220–1238. doi:10.1016/j.actamat.2010.10.055.

[24] L.K. Mansur, Correlation of neutron and heavy-ion damage. II. The predicted temperature shift if swelling with changes in radiation dose rate, J. Nucl. Mater. 78 (1978) 156–160. doi:10.1016/0022-3115(78)90514-7.

[25] S.D. Harkness, C.Y. Li, A study of void formation in fast neutron-irradiated metals, Met. Trans. 2 (1971) 1457–1470.

CHAPTER 2

Nuclear and thermoelectric materials

The development of high-performance materials for energy generation, containment and storage has become a key factor for a more sustainable management of the ever-growing demand for electrical power. Depending on the applicability, certain physical properties of the used materials will have to be analyzed and enhanced in order to boost safety, long term use or the energy conversion efficiency on the specific applications. In nuclear technology, besides from the fissile materials like uranium and plutonium pellets that sustain the chain reactions that will generate energy, other materials are needed to moderate the reaction and prevent the leakage of radiation. These latter materials need to be radiation tolerant while maintaining good mechanical and corrosion resistance, for example. In the case of thermoelectric technology, the materials that will be used to convert heat into electricity need to have good electric transport properties and poor thermal conductivity and, for the case of combined nuclear-thermopower applications, also maintain its integrity in a radiation harsh environment.

This chapter will focus on the explanation of some of the main aspects of the two types of materials studied in this thesis. This introduction is relevant for the discussion of the results obtained as triggered by ion implantation/irradiation effects. For nuclear materials, a more general description of their usage in nuclear reactors will be given, followed by an account about the AISI 316L complex alloy, which is a stainless steel class usually implemented or considered as a model case material in nuclear technology. For thermoelectric materials, a brief account of the atomic structure and how it affects the electrical and thermal properties will be made, followed by a description of the candidate material for thermoelectricity used in this work, chromium (di)silicide, $CrSi_2$.

2.1 Nuclear materials

A nuclear reactor is a complex device composed by many elements. Figure 2.1 depicts an illustration of its main components. The core of a nuclear reactor is composed of the fuel element (usually UO_2 pellets) protected by a cladding material. The fuel rods are in a medium that acts as a moderator of the reaction. The moderator deaccelerates the neutrons in order to sustain the fission reaction of thermal neutrons ($0.003\ eV < E < 0.4\ eV$). Involving the moderator, there is the reflective material, which has the function of reflecting the neutrons back to the center of the reactor core, preventing leakage and increasing the neutron flow. The role of the radiation shielding, as the name implies, is to protect the exterior of the reactor from potential neutron and gamma radiation leaks, so this material needs to be highly neutron-absorbing. Finally, the control rods serve to absorb a portion of the neutrons, and thus control the reaction of nuclear fission by keeping it at steady state, thus avoiding a supercritical chain reaction. The liquid (or gas) cooler is an important part of the core, as it helps to remove the heat generated by the fission reaction.

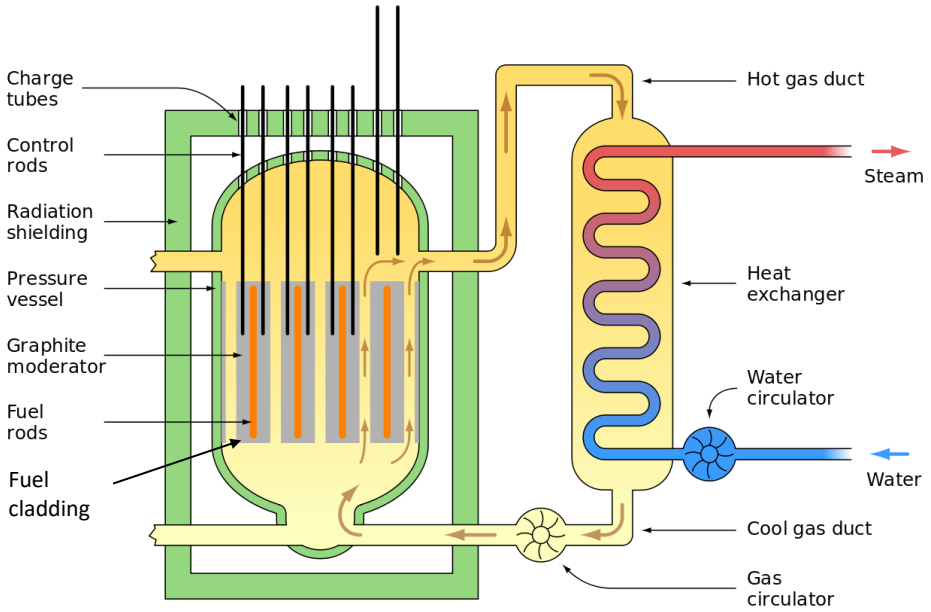

Fig. 2.1 Schematic diagram of an early Magnox nuclear reactor with a cylindrical, steel, pressure vessel. The heat exchanger is outside the concrete radiation shielding. Image taken from [1]

Generally speaking, the fuel cladding is an important safety barrier in fission nuclear reactors, as it restrains most of the radioactive fission products within its volume. However, the damage produced by energetic particle irradiation originated from the fission reactions occurring in the fuel rods changes the mechanical and chemical properties of these materials, reducing its lifetime and potentially leading to a serious compromise of the reactor core system. Thus, the fuel cladding material must have low neutron absorption to allow the interaction between adjacent fuel rods and it must also have high mechanical and chemical stability at high temperatures since it is continuously exposed to corrosion through reactions with the medium. Nowadays, the usual choice for fuel cladding material are Zirconium alloys due to their high resistance to neutron radiation. Stainless steels are also a common choice for fuel cladding material, mainly due to being economically viable and having the mechanical properties needed for this kind of application [2].

Austenitic stainless steels are a class of materials extremely important for nuclear reactor technology, as well as one of the engineering alloys most used in nuclear reactor projects. The most used steel in nuclear technology is the austenitic stainless steel, because it has better resistance to corrosion due to its composition of 12% of Cr and 8% (minimum) of Ni. Austenitic stainless steels have high toughness and relatively high tensile strength. They are non-magnetic and have a low amount of C in their composition that helps to reduce carbide precipitation. The elevated Cr content (minimum 12%) in solid solution, allows the surface passivation leading to corrosion resistance in different environments and temperatures. At high temperatures (> 500 °C), precipitation may occur inside and along grain boundaries of the stainless steel crystal lattice, and dispersed phases such as $M_{23}C_6$ (with M = Cr, Fe, Mo, Ni) can be formed. The precipitation decreases the amount of Cr dissolved in the austenitic matrix, negatively affecting its corrosion resistance [3]. Several series of austenitic stainless steels were developed along several years aiming to produce steels more resistant to precipitation and to radiation-induced corrosion. Some of the mostly used in nuclear technology are the ones from the series AISI 304, AISI 348 and AISI 316. In the case of 316 series austenitic stainless steels, Mo is added to the alloy, further contributing to corrosion resistance [4]. In this thesis, we have focused on the study of AISI 316L

alloys, which is a variation of the AISI 316 steel with a very low concentration of carbon (Table 2.1).

Table 2.1: Chemical composition (% mass)

Material	C	Mn	Si	P	S	Cr	Ni	Mo	Fe
AISI 316L	0.03 max	2.0 max	1.0 max	0.04 max	0.03 max	16.00 max	10.00 max	2.00 max	Bal

From: Laboratório de Metalurgia Física – Grupo de Análise de Falhas, UFRGS, Escola de Engenharia – Porto Alegre

In many cases, AISI 316 steel is used to investigate the behavior of this class of material under nuclear reactor operating conditions, since it is a cheaper commercial steel widely used by the nuclear industry itself (its properties are similar to those of more advanced steels, such as AISI 347 and AISI 348).

The analysis of the microstructural stability of model alloys for nuclear fuel cladding materials submitted to high doses of irradiation is one of the aims of this work, and it will be further explored in chapters 4 and 5.

2.2 Thermoelectric materials

Thermoelectricity was observed for the first time by German physicist Thomas Johann Seebeck in 1821 [5].[1] By heating one of the junctions of two connected conductors that were linked to a compass, he observed that the compass' needle moved. Initially, Seebeck concluded that the temperature difference between junctions created a magnetic field inside the material. In 1823, however, Hans Christian Oërsted and Jean-Baptiste Joseph Fourier publicly demonstrate in a speech delivered at the French Academy of Science that the phenomenon was not magnetic, but electric [6]. Eleven years later, in 1834, while studying the electrical conductivity of antimony and bismuth, the French watchmaker and physicist Jean Charles Athanase Peltier observes the contrary effect, *i.e.*, the temperature rise in bars subjected to a current [7]. It was only in

[1] Some historians claim that the first observation of thermoelectric effect occurred in fact in 1794, by Italian scientist Alessandro Volta. Seebeck would have rediscovered the effect independently in 1821.

1857 that Lord Kelvin demonstrates theoretically that an electric current produces different thermal effects depending on whether the current is transmitted from a hot zone to a cold zone or vice versa for the same metal [8]. From then on, the production of electromotive force due to the temperature difference of two metals or alloys in contact was denominated as Seebeck Effect and the production of a temperature gradient in two joints of two conductors of different materials when subjected to an electric voltage in a closed circuit was denominated as Peltier Effect. The technology was refined and the Seebeck effect started to be used for power generation (such as the ones cited in Chapter 1) while the Peltier effect was applied to the development of thermoelectric cooling devices, normally used in refrigerators. Figure 2.2 shows a scheme of the operation of both types of thermoelectric devices.

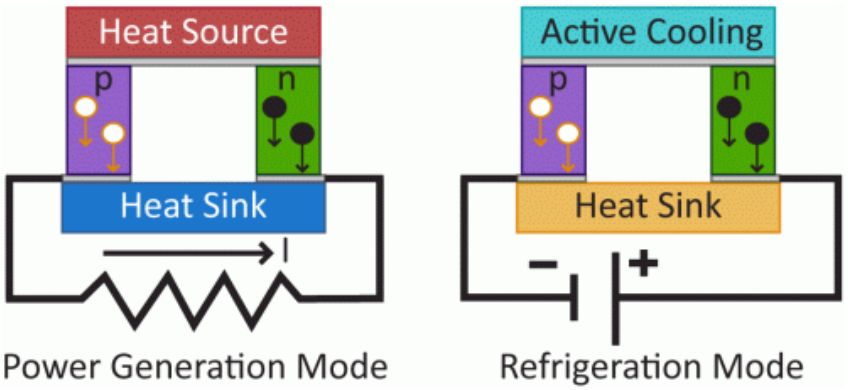

Fig. 2.2 Two different applications of thermoelectric devices for power generation (Seebeck effect) and refrigeration (Peltier effect). In the power-generation mode the upper part of the device is connected to a heat source. The temperature gradient makes charge carriers drift to the cold part. In the refrigeration mode (left panel) a voltage is applied to the device and an electrical current I is created. As electrons in the n-doped part have negative charge and holes in the p-doped part positive charge, charge carriers always drift in the same direction inducing an active cooling in the upper part of the device. Credit: [9,10]

2.2.1 The Seebeck coefficient and the figure of merit

When metals or semiconductors are heated and a temperature gradient between their ends is produced, the mobile charge carriers tend to move from the hot end to the cold end. There is then an accumulation of negative charges, in the case of electrons, or positive, in the case of holes at the cold end. Equilibrium is reached between the chemical diffusion potential and the electrostatic repulsions due to the accumulation of

charges, generating a potential difference ΔV. This potential difference is proportional to the difference in temperature between the two ends (ΔT) when it is kept sufficiently low. The coefficient of proportionality is then called Seebeck coefficient or thermoelectric power, and noted α or S:

$$\alpha = -\frac{\Delta V}{\Delta T} \tag{2.1}$$

The Seebeck coefficient is negative for negatively charged carriers (electrons), and positive for positively charged carriers (electron holes). It generally varies as a function of temperature and depends strongly on the composition of the conductor. For ordinary materials at room temperature, the Seebeck coefficient may range in value from −100 μV/K to +1000 μV/K [11].

The Seebeck coefficient is a fundamental electronic transport property. It measures the entropy transported with the charge carrier as it moves, divided by the carrier's charge. It is affected by charge carriers' interactions with one another, with phonons and with the local magnetic moments of magnetic solids. For metals or degenerate semiconductors (parabolic band, energy-independent scattering approximation) the Seebeck coefficient is given by:

$$\alpha = \frac{8\pi^2 k_B^2}{3eh^2} m^* T \left(\frac{\pi}{3n}\right)^{2/3}, \tag{2.2}$$

where n is the carrier concentration and m* is the effective mass of the carrier [12]. We can relate n to the electrical conductivity (σ) and electrical resistivity (ρ) through the carrier mobility μ:

$$\frac{1}{\rho} = \sigma = ne\mu. \tag{2.3}$$

The Seebeck coefficient, electrical resistivity (or conductivity) and thermal conductivity (κ) are decisive for the measurement of the thermoelectric efficiency of a thermoelectric material (TE). Thermoelectric efficiency is determined by its figure of merit, zT, given by:

$$zT = \frac{\alpha^2 \sigma}{\kappa} T. \tag{2.4}$$

Current conventional thermoelectric materials have a zT value of about 0.8 – 1.0 over a range of temperature of use that give conversion efficiencies of 5-6% [13]. Figure 2.3 shows typical zT values of common thermoelectric materials.

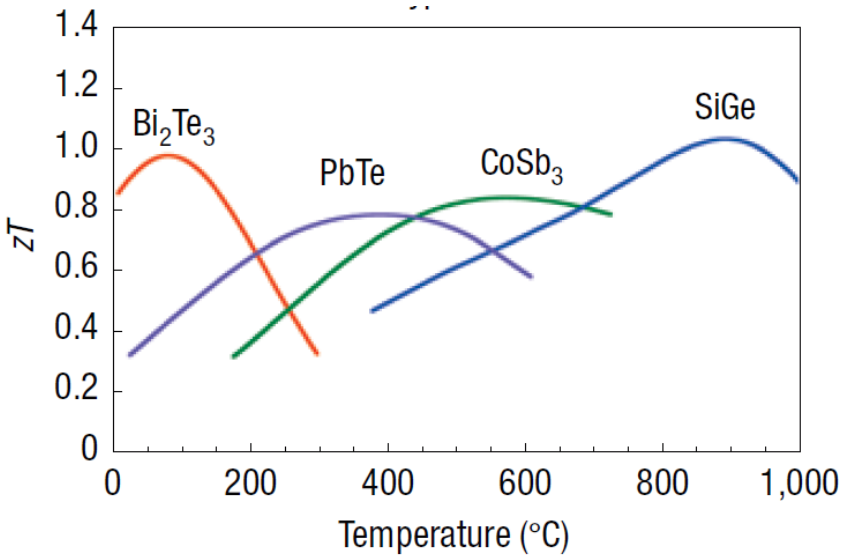

Fig. 2.3 zTs of common thermoelectric materials [12]

From equation 2.4, it is clear that to attain a high figure of merit, both Seebeck coefficient and electrical conductivity must be maximized, while thermal conductivity must be minimized. These three quantities - and consequently, the figure of merit zT - are all dependent on the material's composition, atomic arrangement, and electronic band structure.

2.2.2 Electronic transport

As seen in Eq. 2.4, electrical conductivity is one of the key factors governing the efficiency of thermoelectric materials. Electrical conductivity is determined by the configuration of the energy band structure of the atoms that make up the material. Each configuration will then identify one type of material: metals, semimetals, semiconductors and insulators. Figure 2.4 depicts a scheme of band structures correlated to the types of materials mentioned before.

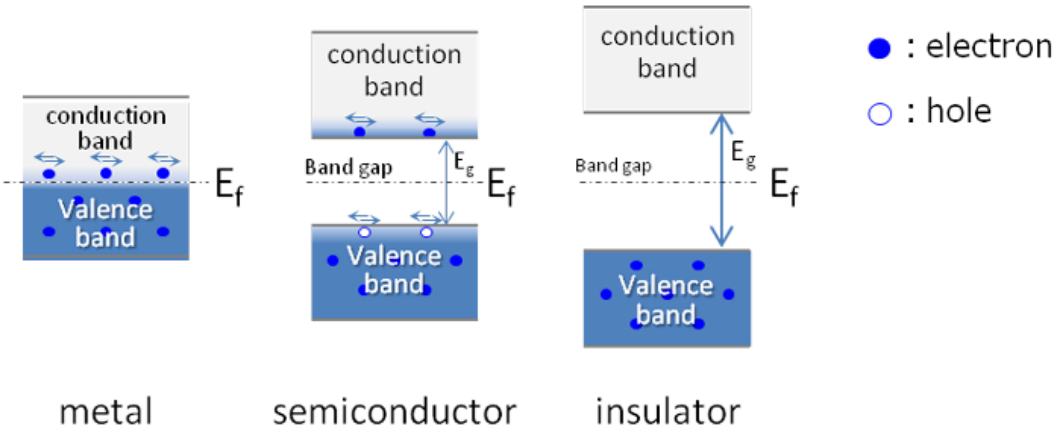

Fig. 2.4 Schematic representation of the band structures of metals, semiconductors and insulators. Image taken from [14]

In metals, the conduction band and the valence band come very close to each other and may even overlap, with the Fermi energy (E_F) somewhere inside. This means that the metal always has electrons that can move freely and so they can always carry current. In semiconductors and insulators, the valence band and conduction band are separated by a forbidden energy gap (E_g) of sufficient width, and the Fermi energy E_F is between the valence and conduction band. To get to the conduction band, the electron has to gain enough energy to jump the band gap. Once this is done, it can conduct. For insulators, the band is so large that basically no electron can jump the gap and there is no current flow. In semiconductors, however, the band gap is smaller and there is enough thermal energy to allow electrons to jump the gap easily and make the transitions in the conduction band. In this case, the number of electrons that jump to the conduction band is equal to the number of holes on the valence band and such semiconductor is denominated intrinsic [15].

The introduction of impurities by doping processes and the presence of lattice defects can insert or absorb electrons in the material and introduce new energy levels in the energy band gap. If the impurity (or defects) gives electrons to the lattice, then a new energy level will be generated near to the conduction band, and the semiconductor will be n-type (Figure 2.5(a)). If now the impurity accepts electrons, consequently generating holes in the lattice, then a new energy level will be created near to the

valence band, and the semiconductor will be p-type (Fig. 2.5(b)). These are extrinsic semiconductor materials.

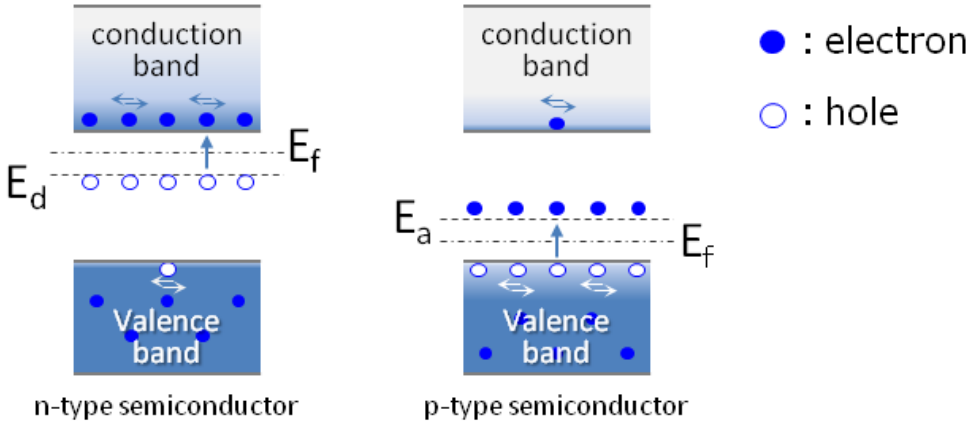

Fig. 2.5 Schematic representation of the band structure of n and p-type semiconductors. Image taken from [14]

In some cases, when the semiconductors are so heavily doped that the Fermi energy level enters the conduction or the valence band, then the semiconductor material is considered degenerate.

Curiously, the best thermoelectric materials are semiconductors that are so heavily doped that their transport properties resemble metals.

2.2.3 Thermal transport

The thermal conductivity κ is the other physical property that will define the applicability of a material as suitable for thermoelectrical applications. Thermal conductivity defines the ability to conduct heat from one point to another in a material. It is defined as the addition of the contribution of lattice vibrations (phonons), denoted as κ_{ph} and charge carriers' movement throughout the lattice, denoted as κ_e:

$$\kappa = \kappa_e + \kappa_{ph}. \tag{2.5}$$

We can see from what was discussed in the previous subsection and from equation 2.3 that charge carriers (electrons) are responsible for electrical conductivity and that they also play an important role on thermal conductivity. In fact, κ_e is related to the electrical resistivity (ρ) and the temperature of the medium by the Wiedmann-Franz law:

$$\kappa_e = \sigma LT = \frac{LT}{\rho} = ne\mu LT, \tag{2.6}$$

with L being the Lorentz factor, 2.4 x 10^{-8} $J^2K^{-2}C^{-2}$ for free electrons [12]. The Lorentz factor can vary with carrier concentration, n. Normally, κ_e is computed indirectly by the measurement of electrical resistivity. From equations 2.3 and 2.6, we see that an increase in the charge carrier concentration will turn both the electrical and the thermal conductivity higher.

In metals, the ratio of thermal to electrical conductivity is about fixed, as the electron part dominates and the contribution from lattice phonons to the thermal conductivity is very low. In semiconductors, however, the phonon part is important and cannot be neglected since it reduces the efficiency. For good efficiency a low ratio of κ_{ph}/κ_e is desired, i.e., $(\kappa_{ph}/\kappa_e) \ll 1$. Therefore, it is necessary to minimize κ_{ph} and keep the electrical conductivity high. The power factor zT can now be rewritten as:

$$zT = \frac{\alpha^2/L}{1 + \frac{\kappa_{ph}}{\kappa_e}} T. \tag{2.7}$$

The materials that exhibit the lowest lattice thermal conductivities are glasses. Nevertheless, glasses present very poor electrical conductivity due to increased electron scattering. Furthermore, they present a lower effective mass because of broader bands (a high effective mass is needed for a high Seebeck coefficient (See Eq.2.2). Good thermoelectrics are, therefore, materials that manage to scatter phonons like a glass without significantly disrupting the electrical conductivity. Until now, the best attempts to obtain such a material were with heavily doped crystalline semiconductors, where the introduction of isoelectronic elements preserves the crystalline electronic structure while enhancing electrical conductivity at the same time that they create a large mass contrast that disrupts the phonon path [11,12].

2.2.4 Thermoelectricity in amorphous materials

All the previous considerations about electronic and thermal transport regard the behavior of materials with a high lattice order – crystalline materials. The characteristic band structure with discreet energy levels of crystalline materials is not found in amorphous materials. To discuss the differences in electrical and thermal conductivity between these two types of materials we need first and foremost to define what an amorphous material is.

Generally speaking, amorphous implies the random arrangement of atoms, the absence of any periodic symmetry, or the absence of any crystalline structure. However, this total lack of periodicity is seldom found in solids. In fact, in amorphous materials the relative positions of the nearest neighbors of an atom are basically the same as in their crystalline counterparts, and what differentiates them is that the long-range periodicity of amorphous materials cannot be predicted. In short, we can say that amorphous materials have only short-range periodicity. The atoms of amorphous semiconductor materials will generally arrange themselves in a continuous random network that correlates in order up to the third or fourth nearest neighbors (Fig. 2.6(b) and (c)). Amorphous pure silicon, for example, contains numerous dangling bonds like those found in crystalline silicon in the presence of vacancies (Fig. 2.6(a)).

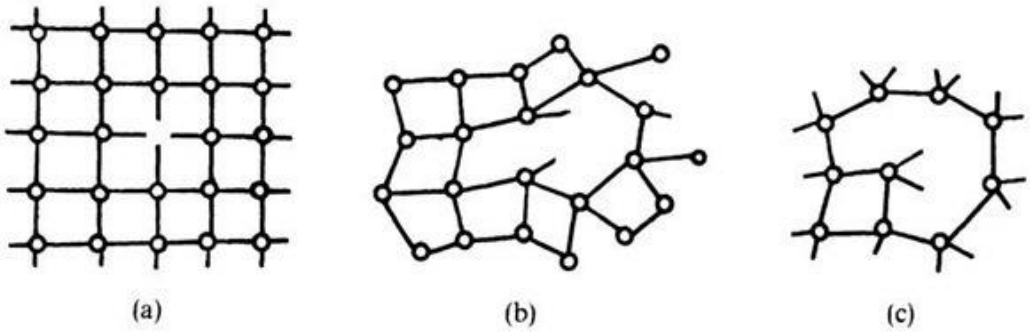

Fig. 2.6 Defects in crystalline and amorphous silicon. (a) Monovacancy in a crystalline semiconductor; (b) one and (c) two dangling bonds in a continuous random network of an amorphous semiconductor. Image taken from [16].

The electrical conductivity for amorphous semiconductors depends, as usual, on the density of carriers, n and the mobility of these carriers, μ (Eq. 2.3),**.** The density of

carriers in amorphous semiconductors is extremely small, because all electrons are strongly bound (localized) to their respective nuclei. Because of the stronger binding forces which exist between the atoms in covalently bound materials (such as in transition metal silicides), the valence electrons are tightly bound, or localized. Therefore, the density of states for the localized states extends into the "band gap" (Figure 2.7). This may be compared to the localized impurity states in doped crystalline semiconductors, which are also located in the band gap. Thus, we observe the formation of a density of states tails. These tails may extend, for some materials, so far into the gap that they partially overlap. In general, however, the density of electron and hole states for the localized levels is very small.

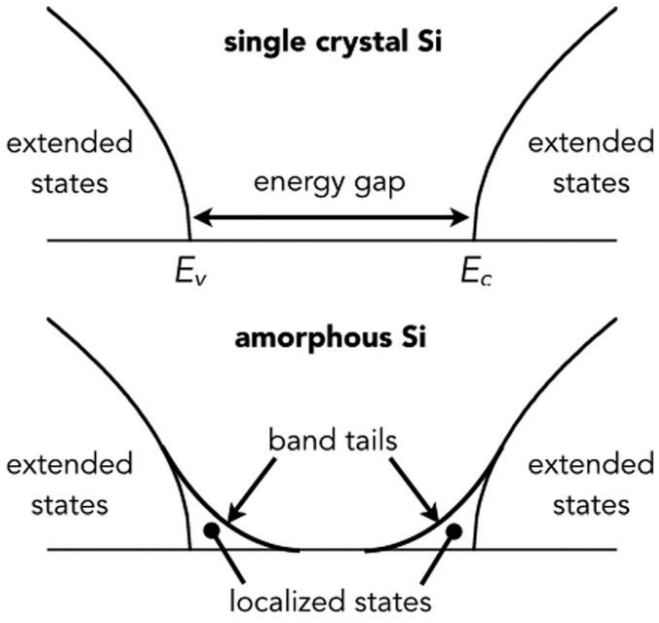

Fig. 2.7 Density of states in single crystal and amorphous silicon. The bottom panel shows the emergence of localized states within the energy gap in amorphous silicon. Image taken from [17]

Likewise, the mobility of the carriers is small because the absence of a periodic lattice causes substantial incoherent scattering. Consequently, the room-temperature conductivity in amorphous semiconductors is generally very low. Some of the localized electrons might occasionally acquire enough thermal energy to overcome barriers which are caused by potential wells of variable depth and hop to a neighboring site. Thus, the

conduction process in amorphous semiconductors involves a temperature-dependent activation energy. The conductivity in amorphous semiconductors increases exponentially with increasing temperature, because any increase in thermal energy provides additional free carriers.

The absence of long-range periodicity in amorphous materials prevents the application of the principles of phonon transport presented previously in the case of crystalline materials. Strictly speaking, thermal conductivity is lower in amorphous materials because the disordered atomic structure can serve as scattering centers for phonons. The first studies on amorphous semiconducting phases gave promising results [18,19]. Their complex and disordered structure is favorable to a strong reduction in thermal conductivity. However, their properties are currently limited by a low electrical resistivity close to that of a metal.

The optimization of ρ and α requires a fine control of effective mass and charge carrier concentration. A high effective mass, m^*, is favorable to the increase of α (according to equation 2.2). However, if m^* is high, carrier mobility decreases, which increases ρ. A compromise between the two quantities must therefore be found.

2.2.5 State of the art of thermoelectric materials

The most widely used materials at room temperature (300-450 K) are the phases derived from Bi_2Te_3, Bi_2Se_3 and Sb_2Te_3 used especially in refrigeration or heat recovery applications [20]. Generally, after doping with Sb or Se atoms, it is possible to vary the concentration of charge carriers and to decrease their thermal conductivity. These compounds currently constitute the commercial materials with the highest figures of merit at room temperature (zT between 0.8 and 1.1) [20].

At medium temperature (500 to 800 K), the chalcogenide PbTe, which has a zT of about 0.8 to 600 K, is the reference material [21]. It has been used as a source of energy in space applications between 1961 and 1975, operating with a radioisotope as a hot source [22]. Among the chalcogenides, TAGS materials, composed of tellurium, silver, germanium and antimony were developed as $AgSbTe_2$ and GeTe solid solutions to replace PbTe and its derivatives. They show better merit factors with a zT greater than 1.2 for the compound (GeTe) 0.85 ($AgSbTe_2$) 0.15 [23]. Finally we can add the β-

$FeSi_2$ phase which, despite its lower performance, has a low cost and good stability and resistance to oxidation [24].

At the regimen of high temperature (> 800 K), Si-Ge alloys are generally used. Si and Ge are both semiconductors with interesting Seebeck coefficient but very high thermal conductivity. In the case of Si-Ge alloys, the thermal conductivity is greatly reduced, which increases zT. A maximum of zT of about 1 was obtained in $Si_{0.8}Ge_{0.2}$ n-type at 1150 K [25].

Besides from the conventional thermoelectric materials discussed above, in the last few years studies on less conventional phases have started to appear. Among the new materials are the half-Heusler compounds whose many vacant sites allow the substitution of elements, thus the thermal and electrical properties can be modulated by mass difference or doping [11]. Other materials, such as clathrates and skutterudites have been developed to have cagelike structures that can enclose guest molecules or atoms that will largely affect the phonon propagation. Some of these compounds are, for example, Cs_8Sn_{44}, $Ba_6Ga_{16}Si_{30}$, $Sr_6Ga_{16}Ge_3$, $LaFe_4Sb_{12}$ and $CeFe_4Sb_{12}$ [11].

2.2.5.1 Chromium (di)silicide

Transition metal silicides ($TMSi_2$) are commonly used as thermoelectric materials because they have a high melting point, are thermally stable at high temperatures and have high electrical conductivity [26,27]. Chromium (di)silicide, $CrSi_2$, is a semiconductor material with potential for thermoelectric applications [11]. The main advantage of using $CrSi_2$ as thermoelectric material is that, unlike most materials used for this type of application, such as PbTe, Bi_2Te_3, Bi_2Se_3 and AgSbTe, $CrSi_2$ is less toxic and its constituents are more abundant in the earth's crust, which considerably reduces its production cost. $CrSi_2$ has a sufficiently high electrical conductivity ($\sigma \approx 10^5$ S/m) and Seebeck coefficient ($S \approx 100$ µV/K for crystalline $CrSi_2$ and $S \approx 60$ µV/K for amorphous $CrSi_2$ at room temperature) and its properties can be optimized in the same temperature range as PbTe - including with similar power factors -, which for the moment is one of the most efficient thermoelectric materials that exist, next to Bi_2Te_3 [27,28]. However, $CrSi_2$ has a large thermal conductivity

($\kappa \approx 10$ W/mK) that must be reduced so that it can be used effectively as a thermoelectric material [29,30].

As it will be presented in chapters 3 and 6, ion implantation and/or ion irradiation can serve as a tool to tailor the samples microstructure and affect their physical properties. These techniques can be used to introduce point, extended defects and dangling bonds that can be electrically active and enhance the charge transport in the lattice [11,19,31]. The vacancies and interstitials introduced by ion implantation/irradiation can also act as scattering centers for phonons, affecting the thermal conductivity. Moreover, depending on the experimental parameters, ion implantation can induce the recrystallization of amorphous materials, where the crystallites formed can also disrupt the phonon path [32].

References

[1] Magnox. https://en.wikipedia.org/wiki/Magnox (accessed June 21, 2019).

[2] C.R.F. Azevedo, Selection of fuel cladding material for nuclear fission reactors, Eng. Fail. Anal. 18 (2011) 1943–1962. doi:10.1016/j.engfailanal.2011.06.010.

[3] G. Krauss, Steels: Processing, Structure and Performance, ASM Internacional, 2005.

[4] P. Marshall, Austenitic Stainless Steels: microstructure and mechanical properties, 1st ed., Springer Netherlands, 1984.

[5] T.J. Seebeck, Magnetische Polarisation der Metalle und Erze durch Temperatur-Differenz, Abhandlungen Der Dtsch. Akad. Der Wissenschafren Zu Berlin. 265 (n.d.) 265–373.

[6] J. Fourier, H.C. Oersted, Sur quelques nouvelles experiences thermo-electriques, Ann. Chim. Phys. (1823) 375–389.

[7] J.C. Peltier, Nouvelles expériences sur la caloricité des courants électriques, Ann. Chim. Phys. 42 (1834) 371–387.

[8] W. Thomson, On a Mechanical Theory of Thermo-Electric Currents, Proc. R. Soc. Edinburgh. 3 (1857) 91–98.

[9] Thermoelectric devices, (n.d.). https://sites.suffolk.edu/scioto/2016/03/04/thermoelectric-devices/ (accessed June 21, 2019).

[10] T.M. Tritt, M.A. Subramanian, Thermoelectric Materials, Phenomena, and Applications: A Bird's Eye View, MRS Bull. 31 (2006).

[11] D.M. Rowe, ed., Thermoelectrics Handbook: macro to nano, Taylor & Francis Group, New York, 2006.

[12] G.J. Snyder, E.S. Toberer, Complex thermoelectric materials, Nat. Mater. 7 (2008) 105–114.

[13] J.R. Sootsman, D.Y. Chung, M.G. Kanatzidis, New and old concepts in thermoelectric materials, Angew. Chemie. 48 (2009) 8616–8639.

[14] Properties of semiconductors, (n.d.).

[15] C. Kittel, Introduction to Solid State Physics, 8th ed., John Wiley & Sons, 2004.

[16] Electrical Properties of Polymers, Ceramics, Dielectrics, and Amorphous Materials Part 2, (n.d.).

[17] G. Horowitz, Validity of the concept of band edge in organic semiconductors, J. Appl. Phys. 118 (2015). doi:10.1063/1.4931061.

[18] G.S. Nolas, H.J. Goldsmid, Amorphous Thermoelectrics, in: 21st Int. Conf. Thermoelectr., 2002: pp. 296–298.

[19] Y. Wu, J. Nyle, C. Naseyowma, N. Newman, F.J. Garcia-garcia, Comparative Study of the Thermoelectric Properties of Amorphous Zn41Sb59 and Crystalline Zn4Sb3, Chem. Mater. 21 (2009) 151–155.

[20] S.M. Kauzlarich, S.R. Brown, G.J. Snyder, Zintl phases for thermoelectric devices, Dalt. Trans. (2007) 2099–2107.

[21] R. Amatya, R.J. Ram, Trend for Thermoelectric Materials and Their Earth Abundance, J. Electron. Mater. 41 (2011) 1011–1019.

[22] Power and Thermal Systems, (n.d.). https://rps.nasa.gov/power-and-thermal-systems/power-systems/current/ (accessed May 21, 2019).

[23] C.M. Bhandari, Minimizing the Thermal Conductivity, in: D.M. Rowe (Ed.), Handb. Thermoelectr. Macro to Nano, CRC Press, 1995.

[24] A.D. LaLonde, Y. Pei, H. Wang, G.J. Snyder, Lead telluride alloy thermoelectrics, Mater. Today. 14 (2011) 526–532.

[25] J.P. Fleurial, Design and discovery of highly efficient thermoelectric materials, in: 9th CIMTECH World-Ceramics Congr. Forum New Mater., 1998: pp. 733–744.

[26] M.I. Fedorov, V.K. Zaitsev, Thermoelectrics of transition metal silicides, in: D.M. Rowe (Ed.), Thermoelectr. Handb. Macro to Nano, CRC Press, 2009.

[27] A. Nozariasbmarz, A. Agarwal, Z.A. Coutant, M.J. Hall, J. Liu, R. Liu, A. Malhotra, P. Norouzzadeh, C. Ozturk, V.P. Ramesh, Y. Sargolzaeiaval, F. Suarez, D. Vashaee, Thermoelectric silicides : A review, Jpn. J. Appl. Phys. 56 (2017).

[28] T. Dasgupta, J. Etourneau, B. Chevalier, S.F. Matar, A.M. Umarji, Structural, thermal, and electrical properties of CrSi2, J. Appl. Phys. 103 (2008). doi:10.1063/1.2917347.

[29] S. Perumal, S. Gorsse, U. Ail, B. Chevalier, R. Decourt, A.M. Umarji, Effect of co-substitution of Mn and Al on thermoelectric properties of chromium disilicide, J. Mater. Sci. 48 (2013) 227–231. doi:10.1007/s10853-012-6732-4.

[30] M. Abd El Qader, R. Venkat, R. Kumar, T. Hartmann, P. Ginobbi, N. Newman, R. Singh, Structural, electrical, and thermoelectric properties of CrSi2 thin films, Thin Solid Films. 545 (2013) 100–105. doi:10.1016/j.tsf.2013.07.040.

[31] A. Desalvo, F. Zignani, R. Galloni, R. Rizzoli, M. Ruth, Doping of amorphous

silicon by potassium ion implantation, Philos. Mag. B. 67 (1993) 131–142. doi:10.1080/13642819308230224.

[32] S. V. Novikov, A.T. Burkov, Grain boundary scattering contribution to the thermopower in Cr-Si nanocrystalline films, J. Phys. Conf. Ser. 769 (2016). doi:10.1088/1742-6596/769/1/012069.

CHAPTER 3

Review on ion-solid interactions

When energetic particles impinge on a target material, they will collide with the atoms of the matrix, transferring some of their energy. The result of this interaction will depend on both the type of incident particle and its initial energy and on the characteristics of the target material. In this chapter, it will be presented some of the main aspects of ion-solid interactions, including the concept of collision cascade and the description of some typical implantation and irradiation effects that will be of importance for the discussion of the results presented in Chapters 5 and 6.

3.1 Ion-solid interaction

When an ion accelerated with an energy E_0 impinges on a material it will lose part of its energy as it goes through the material. Some of its energy will be lost due to interactions between the ion and the electronic cloud (inelastic collisions) and the atomic nuclei (elastic collisions). A way to estimate the amount of energy lost by the ion as it traverses the material is to analyze its stopping power behavior, which depends on the initial parameters of the interacting ion, such as mass and energy, and on the target's characteristics, such as density and chemical composition. The stopping power is a function of the ion energy (S=S(E)) and can be in a good approximation expressed as a combination of two terms; one that refers to the incident ion interaction with the target's electrons, called electronic stopping power (S_e), and the other term refers to the interaction between the incident ion and the atoms' nuclei, named as nuclear stopping power (S_n). Both energy loss processes can be considered as independent [1]. The total stopping power, measured as an energy loss flux (E) in length (x) is given by:

$$S = S_e + S_n = \frac{dE}{dx}_e + \frac{dE}{dx}_n \tag{3.1}$$

The electronic stopping power is described by inelastic collisions between the incident ion and the target's electrons because the electrons absorb energy leading to their excitation and/or ionization, without causing atomic displacement. Due to the small mass of the target's electrons, the incident ions practically do not suffer deviation from their trajectory by the electronic influence. However, in the high energy regimen, the electronic stopping power becomes the dominant energy loss process because the cross-section for nuclear collisions decreases with $1/E^2$. At rather high energies (not covered in this work), for example, heavy ions with energy of hundreds of MeV can trigger an "Coulombian explosion", where the loss of electrons along the ion trajectory causes the ejection of the atoms from their equilibrium positions due to Coulomb repulsion, generating extensive damage in the crystal lattice [2].

The nuclear stopping power is described by elastic collisions as the incident ions and the atomic nuclei interact. In this interaction the accelerated ion transfers kinetic energy to the nuclei, which can cause the displacement of the atoms from their equilibrium positions in the crystal lattice. This process generates point defects such as vacancies and interstitials. If the primary knocked-on atom (PKA) has still some exceeding energy, it will be able to transfer this excess to another atom, giving rise to a collision cascade. This effect can cause the formation of extended defects such as atomic clusters, dislocation loops and cavities. The energy loss due to nuclear interactions is predominant for low energies or heavy ions, since the probability for a collision between slower and/or heavier ions and atomic nuclei is more significant.

The determination of the low, high and intermediate energy ranges for the stopping power analysis depends on the combination between interacting ion and target atom. For the case of light ions impinging on light targets the intermediate energies are around 100 keV. For heavy ions impinging on light targets the intermediate energy range falls to around 20 keV. Figure 3.1 shows the graph of the energy loss and projected range (R_p) as a function of energy for the case of (a) Au and (b) Ag ions impinging on a stainless steel target [3].

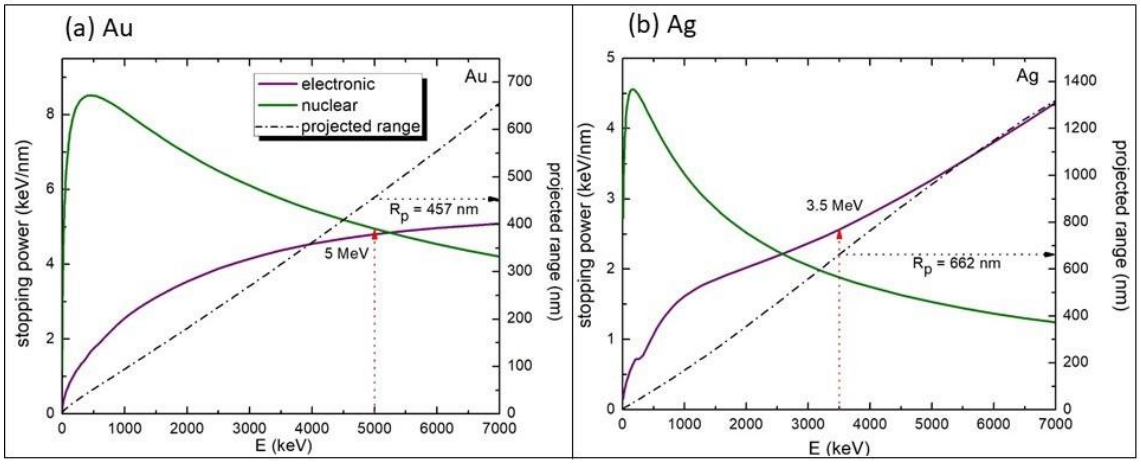

Fig. 3.1 Nuclear and electronic stopping powers as a function of ion energy for the interaction of steel targets with (a) Au and (b) Ag ions. The dotted lines represent the energies and projected ranges of the ions used in this work

In many stages of this work, 5 MeV Au ions were used, as detailed in Fig. 3.1(a). In these conditions, the energy losses due to the nuclear and electronic stopping power have very similar values, of approximately 4.9 and 4.8 keV/nm, respectively. In another experiment we used 3.5 MeV Ag ions (Fig 3.1 (b)) and, as can be seen in the figure, the energetic losses coming from electronic interactions are dominant for that energy range. For metallic targets such as the AISI 316L stainless steels samples used in this work and for ions with energies below 5 MeV the inelastic energy losses are dissipated in the form of heat, while the energy losses triggered by elastic processes generate atomic displacements and heat. During irradiation experiments targets with a good thermal contact can have their temperature controlled. Thus, regarding to damage generation, the important parameters to be observed are the target's temperature and the amount of atomic displacements generated by elastic collisions.

When transferring all their kinetic energy to the target's atoms the incident ions will be retained in a specific depth in the material, which will also be dependent on ion initial energy and matrix characteristics. The ion distribution profile in the target is determined by statistical processes, being described by a Gaussian curve given by:

$$C(x) = \frac{\phi}{\sqrt{2\pi} \cdot \Delta R_p} e^{-\frac{(x-R_p)^2}{2(\Delta R_p)^2}} \quad (3.2)$$

where ϕ is the implantation fluence (at/cm²), x is the sample thickness, R_p is the projected range, which determines the dispersion of the ion position around an average maximum value and ΔR_p is the distribution standard deviation, *i.e.*, the width of the ion distribution. The ion implantation profile can be simulated with the SRIM (*Stopping and Range of Ions in Matter*) software, that uses the Monte Carlo method to estimate the nuclear and electronic energy losses, number of displacement per atom, R_p e ΔR_p [4]. Figure 3.2(a) shows the SRIM simulation of the implantation profile of an Ar ion *plateau* in a 500 nm thick stainless steel target. Figure 3.2 (b) shows the same Ar implantation profile now obtained via Equation 3.2 with specific energies and fluences.

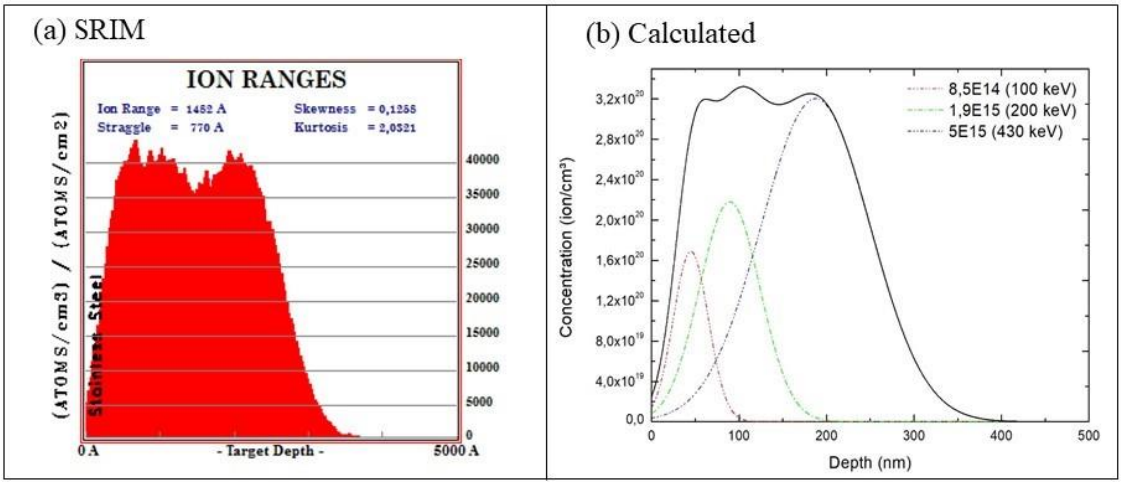

Fig. 3.2 Concentration-depth profile of Ar-*plateau* implantation in stainless steel (a) obtained with SRIM software and (b) calculated with equation 3.2.

With the aid of the tools described above, it is possible to obtain precise models and important information from the implantation and irradiation profiles for various ion species inserted in a wide range of materials.

3.1.1 Collision cascades

The first atom that interacts with the incident ion (or another particle) is denominated primary knock-on atom (PKA). Receiving the energy from the collision, the PKA will move through the lattice and collide with another atom. If the energy

transferred from the PKA to the atom is sufficiently high, this second atom can also be displaced from its equilibrium lattice position and, in its turn, trigger the displacement of a third atom (Figure 3.3). If this sequence of collisions continues, we have what is called a collision cascade – a mechanism that can induce several modifications in the physical and mechanical properties of a material [5].

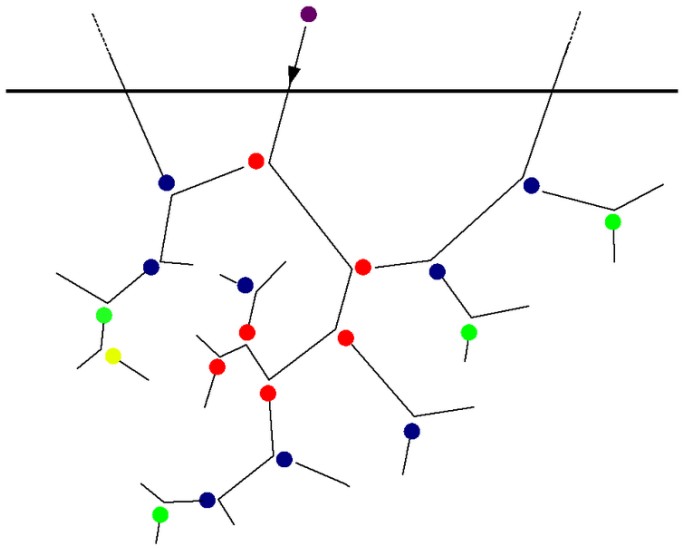

Fig. 3.3 Schematic illustration of a linear collision cascade. The thick line illustrates the position of the surface, and the thinner lines the ballistic movement paths of the atoms from beginning until they stop in the material. The purple circle is the incoming ion. Red, blue, green and yellow circles illustrate primary, secondary, tertiary and quaternary recoils, respectively. Taken from [6]

It must be considered that each particle type will produce different collision cascades. This is mainly due to the way with which the particle interacts with the target's atoms. The interaction of protons with the target atoms is better described by the Coulomb potential, with the Coulomb forces extending to infinity and slowly increasing as the proton approaches an atom. Since protons are lighter, the collision cascades produced by them are smaller and sparser than the ones produced by ions or neutrons. In the case of ions, the interaction is described by the screened Coulomb potential, and the collisions generate many low energy PKAs. In the case of neutrons, the collisions are described by the hard-sphere potential, and the interaction results in the generation of fewer but more energetic PKAs.

A scheme showing the difference between the collision cascades morphologies created by different energetic particles is depicted in Figure 3.4.

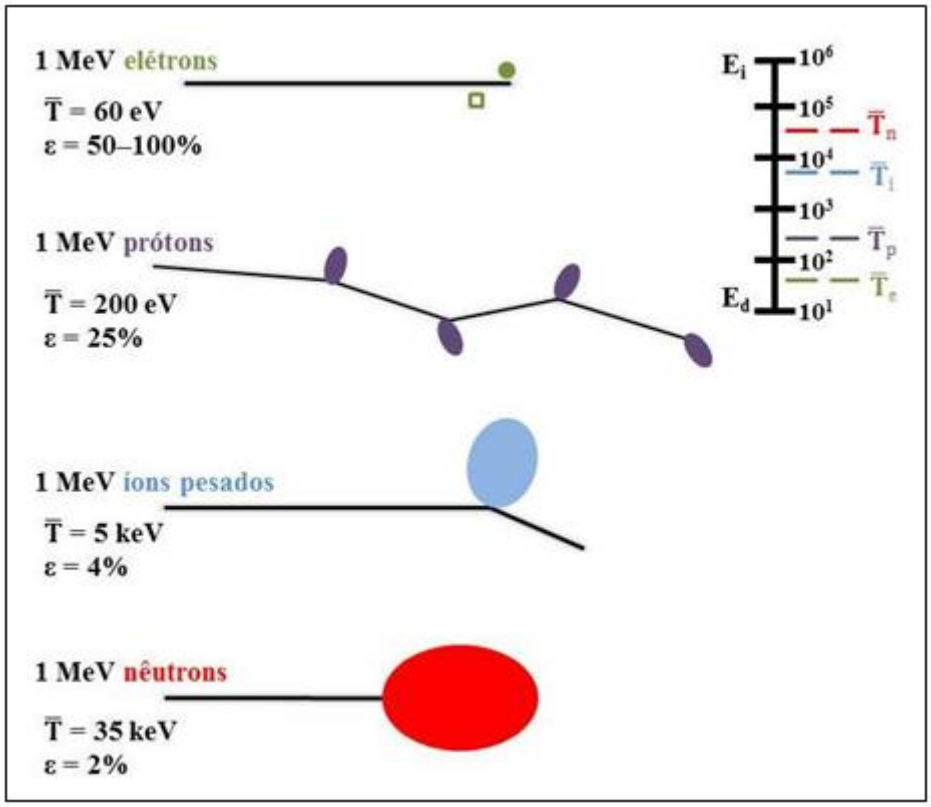

Fig. 3.4 Differences on the morphology, displacement coefficient and mean recoil energy of collision cascades generated by different energetic particles accelerated at 1 MeV in a Ni target. [Adapted from [7]]

In any of the cases cited above the collision cascades will only occur if the incident particle transfers a certain amount of energy that is above a minimum energy value denominated as displacement energy E_d. The displacement energy depends on the type of chemical bonds existent between the target's atoms and normally it is in the energy range of 10 – 60 eV. If the energy that an atom receives after a collision with a particle is smaller than its E_d, then this atom will remain in its equilibrium position. For calculations in softwares like SRIM [4] it is used a displacement energy of 40 eV for the the stainless steel targets while for less dense compounds, such as SiO_2, and E_d of 25 eV is normally used.

The number of defects generated by a PKA is usually calculated considering a linear displacement model developed by Kinchin-Pease in 1955 (at least for the ion irradiation case) [5]. The Kinchin-Pease model assumes that the atomic displacements are caused by a series of independent binary collisions between the incident ions and the target's atoms. The energy transferred in the collisions is described by the hard-sphere isotropic scattering model (elastic collisions: there is no dissipation of energy to the crystal lattice). The Kinchin-Pease model assumes that the number of displaced atoms is given by the relation between the energy transferred by the incident ions T and the displacement energy E_d [5]:

- If $T < E_d$, the incident ion cannot displace an atom from its position in the matrix. In this case, the ion's kinetic energy is dissipated by the vibration of the matrix and the ion becomes an interstitial;
- If $E_d < T < 2E_d$, the knocked atom leaves its equilibrium position and becomes an interstitial atom or recombines with a vacancy. In its place, the knocked atom leaves a vacant site or a vacancy;
- If $2E_d < T < E_c$, where E_c is the cutoff energy, the kinetic energy transferred by the ion to the atom is sufficient to displace the atom from its lattice site and make it travel through the matrix. As it collides with other atoms, it can generate a collision cascade.
- If $T \gg E_c$, the electronic stopping power is dominant and the loss of energy occurs by inelastic collisions and no additional displacements occur until electron energy losses reduce the PKA energy to E_c.

The Kinchin-Pease model is used in softwares like SRIM [4] to estimate the quantity of defects that will be produced in an interaction between incident ions and target atoms.

3.2 Implantation/Irradiation-induced damage formation

The interaction of accelerated particles with the target's atoms leads to the target's microstructure modification. In nuclear materials, for example, the constant exposition to energetic particles can lead to the weakening of the material with consequent decrease of its lifespan. In the case of semiconductor materials, the defects

formed after ion implantation/irradiation can strongly modify the electrical and thermal properties of the material.

As seen in the previous session, the interactions of energetic particles with a target generate collision cascades that will give rise to atomic displacements and defects. Heavier particles, such as neutrons and heavy ions produce denser collision cascades when compared to particles and/or light ions, facilitating the agglomeration of point defects. Moreover, depending on the cascade density, there will be temperature effects on the material [8]. Ion implantation can produce defects such as Frenkel pairs, atomic clusters, dislocation loops and precipitates [5,7]. Some examples of the implantation induced defects can be seen in Figure 3.5.

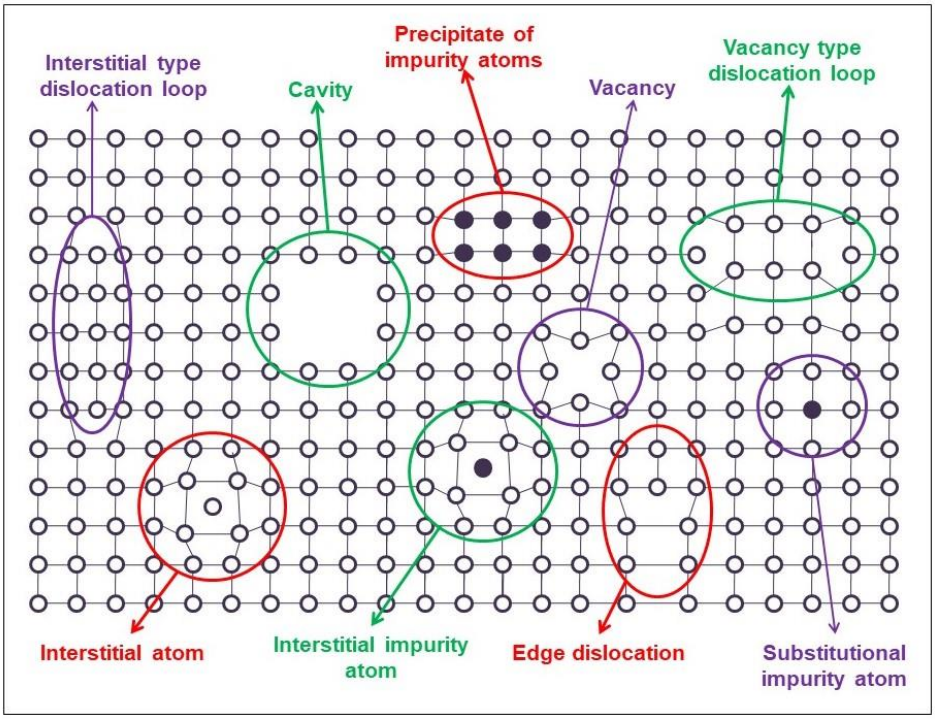

Fig. 3.5 Illustration representing some typical irradiation-induced defects

In this session, we will analyze some of the main types of defects and effects caused by ion implantation.

3.2.1 Amorphization and (re)crystallization

The defects produced by ion implantation and ion irradiation can be, in a certain way, controlled by the ion parameters. In a certain extent, the number of defects produced by ion-solid interactions can be so extensive that the long-range order seen in crystalline

materials can be disrupted, and the solid becomes amorphous. In fact, preferential amorphization can be observed at regions where extended defects first form, for example, at nanocavities or at surfaces [10]. This phenomenon has been widely explored by ion implantation experiments in crystalline Si [2,11].

The other way round is also possible, *i.e.*, induce the crystallization of an amorphous material by ion implantation experiments. This can be explained considering that the defects produced by ion implantation introduce interfaces that will serve as nucleation centers for crystallites. Several studies on ion implantation in a-Si have been carried out and a clear correlation between epitaxial recrystallization and collision cascade density and ion fluence has been found; but there are still many features on the crystallization process that is not yet well understood [2].

A key factor in amorphization and (re)crystallization induced by ion beam experiments is the temperature at which the experiments are performed, because it determines whether the defects produced within collision cascades will be stable or whether they will migrate and coalesce or recombine. Implantation/irradiation fluence is also an important parameter affecting the balance between defect creation and annihilation.

3.2.2 Cavity and bubble formation

Depending on the type of material being analyzed, the nucleation of cavities and/or bubbles can be either a detrimental or a beneficial process. For example, the formation of arrays of bubbles can be used to trap impurities in semiconductor materials and, in the case of thermoelectrics, can be used to disrupt of the phonon mean free path, heavily affecting the thermal conductivity.

In nuclear materials, the formation of bubbles and cavities can induce the swelling of the material (void swelling) (Figure 3.6), which is a most undesirable effect, since it can lead to a drastic reduction in the lifespan of the components of a nuclear reactor. Usually, ferritic/martensitic alloys have a higher resistance to swelling when compared to austenitic alloys, since in the latter ones Cr, Ni and some other elements in a higher concentration can be transmuted into He, increasing the probability of swelling [9].

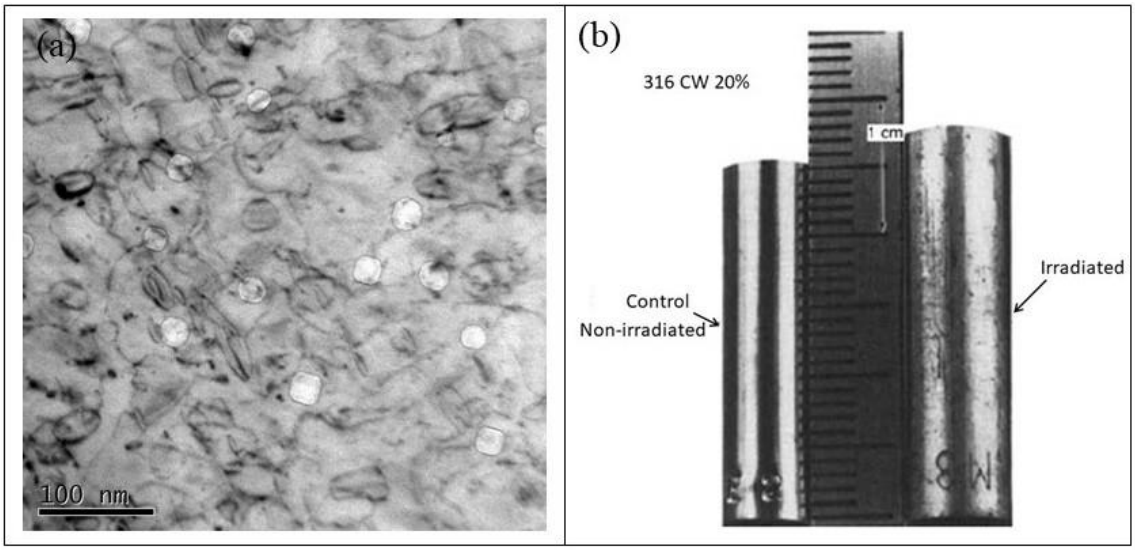

Fig. 3.6 (a) Cavities and dislocations present in AISI 316L austenitic stainless steel irradiated with Au ions at a fluence of 1 x 10^{16} at/cm² (E = 5 MeV) or 40 dpa at 550 ºC (result from this work). (b) Swelling due to the formation of cavities such as those shown in (a) observed in a AISI 316 fuel cladding tube irradiated to 1.5 x 10^{23} n/cm² (E > 0.1 MeV) or 75 dpa at 510 ºC in a EBR-II nuclear reactor [9].

The occurrence of void swelling is a serious problem which mechanisms of formation are complex and are still not fully understood. It is determined by the combination of factors such as temperature variation, the presence of grains of specific sizes, irradiation fluence, material composition, presence/formation of inert gases etc.

The presence of atoms of an inert gas in the matrix can stabilize the formed cavities and/or accelerate the formation of these cavities [12,13]. Once these gas atoms are "trapped" by the cavities, their return to the matrix becomes highly unlikely, and inert gas bubbles are then formed. In general, gas atoms serve as attractors of vacancies (and vice versa).

3.2.3 Precipitation in nuclear materials

In addition, irradiation can cause either the formation of new phases (in equilibrium or non-equilibrium) as well as the modification or destruction of existing phases in the material [14–16].

The many phases that may exist or form in a steel can be classified regarding their behavior under the effect of irradiation. They are classified as radiation-induced, radiation-modified and radiation-enhanced phases [5].

The radiation-induced phases are formed only with irradiation. Some examples are: γ', G, M_xP.

Radiation-modified phases occur both by the influence of irradiation as by thermal influence. Examples: η (M_6C), Laves e M_2P.

Radiation-enhanced phases are normally formed due to thermal effects, but their formation can be accelerated by irradiation. Examples: M_6C, τ ($M_{23}C_6$), MC carbides and the σ and χ intermetallic phases.

Table 3.1 shows some crystallographic and morphological data of several phases belonging to each of the categories mentioned above [5].

Table 3.1

Radiation	Phase	Crystal structure	Lattice parameter (nm)	Morphology	Orientation in γ matrix	Volume misfit
-induced	γ′ (Ni_3Si)	Cubic, A1 Fm3m	0.35	Spherical	Cube on cube	−0.1
	G ($M_6Ni_{16}Si_7$)	Cubic, A1 Fm3m	1.12	Small rod	Random	0.05
	M_2P (FeTiP)	Hexagonal, C22, P321	0.6 ($c/a = 0.6$)	Thin lath	$(1210)_{ppt}\|\|(001)_\gamma$	−0.4
	Cr_3P	Tetragonal, S_4^2 14	0.92 ($c/a = 0.5$)	–	–	∼0
-modified	η (M_6C)	Cubic, E9, Fd3M	1.08	Rhombohedral	Cube on cube or twin	0.1
	Laves (A_2B)	Hexagonal, C14 $P6_3/mmc$	0.47 ($c/a = 0.77$)	Faulted lath	Various	−0.05
	M_2P (FeTiP)	Same	Same	Same	Same	Same
-enhanced	MC	Cubic, B1 Fm3m	0.43	Spherical	Spherical	0.7
	η (M_6C)	Same	Same	Same	Same	Same
	τ ($M_{23}C_6$)	Cubic, $D8_4$ Fm3m	1.06	Rhombohedral platelet	Cube on cube or twin	0.1
	Laves (A_2B)	Same	Same	Same	Same	Same
	σ	Tetragonal, $D8_b$ p4/mnm	0.88 ($c/a = 0.52$)	Various	Various	∼0
	χ	Cubic, A12 143m	0.89	various	various	0.05

Among all phases that can be formed or grown by radiation, three of them will be more important for the scope of this work: $M_{23}C_6$, M_6C (η) and MC carbides. These phases are formed at temperatures around 500 °C.

$M_{23}C_6$ (M = Cr, Fe, Mo): It is the main carbide formed in austenitic stainless steels; it is a metastable phase that appears in the early stages of precipitate nucleation due to its facility to nucleate. It occurs mainly in grain boundaries, in coherent and incoherent twin boundaries and dislocations [15]. The nucleation of $M_{23}C_6$ in grain boundaries is

undesirable, since it causes the depletion of Cr in the regions surrounding the grain, making the steel susceptible to intragranular corrosion and martensitic phase formation during the cooling stage. Besides, the presence of $M_{23}C_6$ promotes the reduction of the hardness and ductility of the steel [16]. To prevent the precipitation of this phase, the amount of C in the alloy may be reduced or elements such as Nb or Ti may be added to promote the nucleation of more stable carbides (MC). In 316 steels, the presence of Mo may favor the partial transformation of $M_{23}C_6$ into M_6C, which is more stable [15]. Due to its fast formation kinetics, the precipitation of $M_{23}C_6$ is almost impossible to avoid in irradiation experiments.

M_6C (Mo, W, Fe, Nb, V): Found mainly in austenitic steels containing Mo. The transformation of the $M_{23}C_6$ phase into M_6C is credited to the absorption of Mo from the matrix by the $M_{23}C_6$ phase, according to the following equation [17]:

$$M_{23}C_6 \rightarrow (FeCr)_{21}Mo_3C_6 \rightarrow M_6C.$$

Normally it is always associated with the presence of $M_{23}C_6$. Since the M_6C phase forms only after long periods of time [15], it has little documentation in the literature.

MC (M = Ti, Zr, Hf, V, Nb, Ta): These carbides are quite stable and are predominantly intragranular, forming normally in dislocations and stacking faults. Due to its low interface energy, its presence is less damaging to properties such as resistance to deformation and is preferable to other carbides. In some studies it is reported that the presence of small MCs can improve some mechanical properties of certain steels and curb grain growth [18]. Furthermore, the MC phase presents a great resistance to coarsening [19].

3.2.4 Simulation of neutron irradiation with ions for the study of nuclear materials

The damage produced by neutron irradiation in nuclear materials accumulates over several years of exposure, and direct observation of these materials becomes impractical. Even the analysis of samples taken from nuclear environments entails a few years of preparation and precautions, since special instruments and facilities must be available for the handling of radioactive samples. Therefore, the simulation of the effects of radiation through particle irradiation (encompassing here light, heavy ions or

electrons) has become necessary and, in many ways, advantageous, since it is possible to produce basically the same defects in the materials of interest in much less time (some tens of hours) and with much more safety, since irradiation with ions does not rend the material radioactive.

To reproduce the effects of neutron irradiation with ions, some experimental parameters must be adjusted. It must be considered that the rate of irradiation with ions is much faster than with neutrons and that the ions produced in an ion accelerator are practically mono-energetic, whereas the neutron energy spectrum in a reactor can present dozens of orders of magnitude (Figure 3.7).

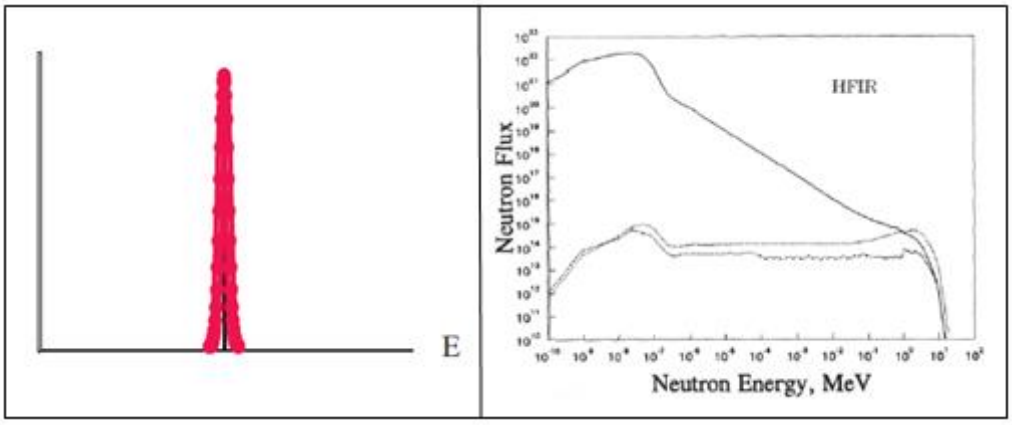

Fig. 3.7 Energy distribution of (a) ions produced in an accelerator and of (b) neutrons in a reactor [7]

In addition, the penetration distance of ions and neutrons is different; since ions are electrically charged, they lose energy very rapidly in a non-uniform manner throughout the material, while neutrons reach greater distances causing damage in a more uniform way (Figure 3.8). Another important feature is that ion irradiation experiments should be performed at relatively high temperatures, ~500 °C, to reproduce the effects of neutron irradiations at ~ 300 °C [20,21].

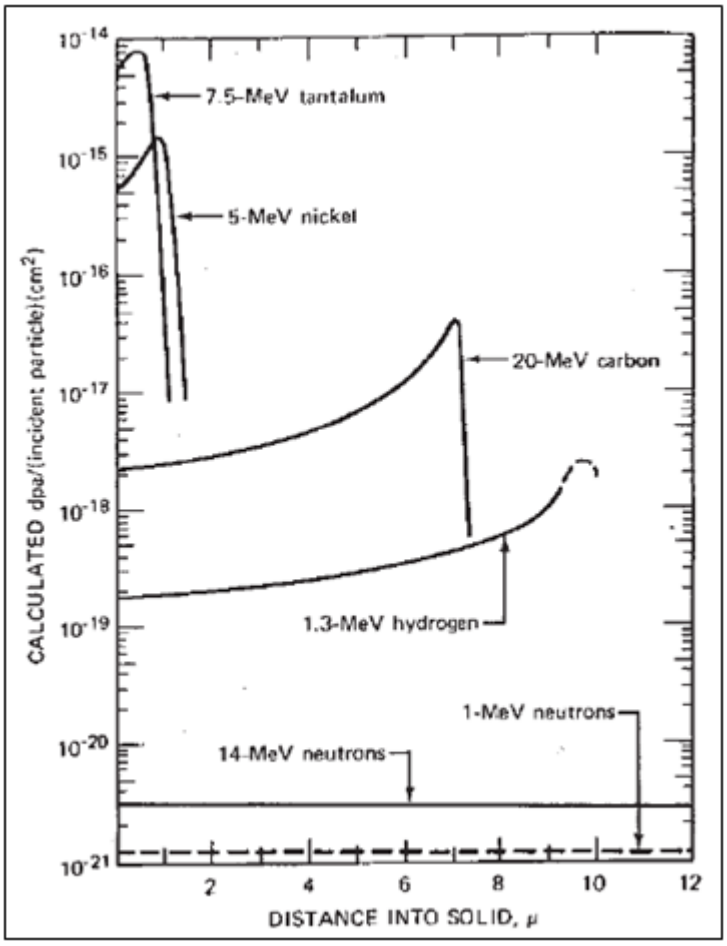

Fig. 3.8 Dislocation per atom as a function of solid-depth for neutrons and ions at different energies [7].

In this way, the equivalence between ions and neutrons is more easily calculated by the choice of parameters, such as irradiation energy and fluence, which will produce the same amount of atomic displacements at each interaction. This estimation is computed by the displacement per atom (dpa) formula:

$$dpa = \frac{fluence\ (ions\ cm^{-2}) * Vac(ion^{-1}cm^{-1})}{N(at.cm^{-3})}. \qquad (1.5)$$

Furthermore, the equivalence between irradiation with ions and neutrons can be confirmed by comparing the characteristics of the damages produced by each irradiation; some studies have shown that the size and density of vacancies and/or bubbles and the formation of dislocation loops and other types of microstructural

defects produced after ion irradiation are very similar to those present in neutron-irradiated materials [22–24].

References

[1] M. Behar, P.F.P. Fichtner, P.L. Grande, F.C. Zawislak, Mater. Sci. Eng. 15 (1995) 1–83.

[2] H. Bernas, ed., Materials Science with Ion Beams, Springer, 2010.

[3] J.P.B. J.F. Ziegler, (2003).

[4] J.F. Ziegler, J.P. Biersack, (2003) http://www.srim.org/.

[5] G.S. Was, Fundamentals of Radiation Materials Science, Springer, 2007.

[6] (n.d.).

[7] K.E. Sickafus, E.A. Kotomin, B.P. Uberuaga, eds., Radiation Effects in Solids, Springer Science & Business Media, 2007.

[8] D. Kaoumi, A.T. Motta, R.C. Birtcher, J. Appl. Phys. 104 (2008) 1–13.

[9] K.L. Murty, I. Charit, An Introduction to Nuclear Materials: Fundamentals and Applications, 2013.

[10] R.S. Averback, T.D. de la Rubia, Solid State Phys. - Adv. Res. Appl. 51 (1997) 281–402.

[11] E. Oliviero, S. Peripolli, L. Amaral, P.F.P. Fichtner, M.F. Beaufort, J.F. Barbot, S.E. Donnelly, J. Appl. Phys. 100 (2006).

[12] K.C. Russell, (1992).

[13] A. Müller, V. Naundorf, M. Macht, A. Moller, V. Naundorf, M.P. Macht, 3445 (2004).

[14] F.. Beckitt, B.. Clark, Acta Metall. 15 (1967) 113–129.

[15] T. Sourmail, Mater. Sci. Technol. 17 (2001) 1–14.

[16] P. Marshall, Austenitic Stainless Steels: Microstructure and Mechanical Properties, 1st ed., Springer Netherlands, 1984.

[17] B. Weiss, R. Stickler, Metall. Trans. A 3 (1972) 851–866.

[18] J. Ki Leuk Lai, C. Hung Shek, K. Ho Lo, Stainless Steel: An Introduction and Their Recent Developments, Bentham Science Publishers, 2012.

[19] J.W. Martin, ed., Concise Encyclopedia of the Structures of Materials, 1st ed., Elsevier, 2007.

[20] L.K. Mansur, J. Nucl. Mater. 78 (1978) 156–160.

[21] L.K. Mansur, J. Nucl. Mater. 216 (1994) 97–123.

[22] A. Renault-Laborne, J. Malaplate, C. Pokor, B. Tanguy, Eff. Radiat. Nucl. Mater. 26th Vol. 74 (2014) 1–24.

[23] H.R. Brager, J.L. Straalsund, J. Nucl. Mater. 46 (1973) 134–158.

[24] J.K.L. Lai, D.J. Chastell, P.E.J. Flewitt, Mater. Sci. Eng. 49 (1981) 19–29.

CHAPTER 4

Experimental Procedure

In this chapter the experimental procedures performed during this work will be reported, including the preparation of 316L stainless steel and $CrSi_2$ samples as well as the characterization techniques, data collection and analyses used in this work. Among these techniques, the techniques of ion implantation and irradiation, thermal treatments, transmission electron microscopy (TEM), scanning transmission electron microscopy (STEM), energy dispersive X ray spectroscopy (EDX), four-point electrical measurements by Hall Effect and electron diffraction will be described.

4.1 AISI 316L sample preparation

250 μm thick AISI 316L stainless steel samples are cut into discs with diameters of 3 mm (suitable for TEM sample holders). The discs are then mechanically polished to reduce the surface roughness. The grinding-polishing process is performed using sandpapers with distinct mashes (1200, 2400 and 4000) and then finished with 1 and ¼ μm diamond pastes. After these steps, the samples' surfaces become–completely smooth, with virtually no grooves visible by optical microscopy. Figure 3.1 shows optical micrographs of the sample in the stages before and after the mechanical polishing.

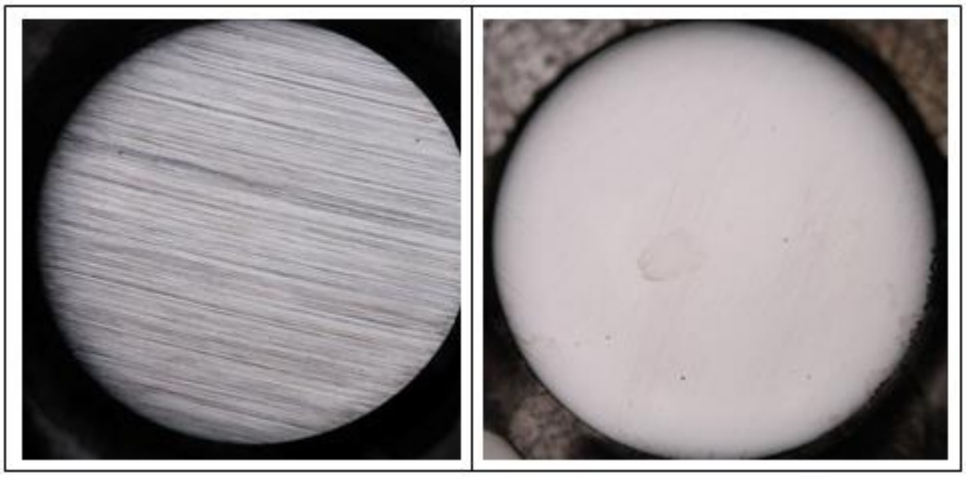

Fig 4.1 AISI 316L sample (a) after the polishing with the first sandpaper and (b) after the polishing with the last felt. 50X magnification.

The polished samples are solution-annealed in high vacuum (pressures of $\approx 2 \times 10^{-6}$ mbar) at 1050 °C for 2 hours, carried out in a conventional furnace where the samples are inserted into a cylindrical quartz tube. This process serves to dissolve the existing carbides, solubilizing the carbon content in the austenitic matrix to produce a metal-carbon solid solution. The solid solution is retained via a sufficiently fast cooling process which simply consists of the removal of the tube from the furnace. This heat treatment also serves to relieve the matrix of internal mechanical stresses caused by cold working (polishing). It should be noted that the solution-annealing treatment also causes the grain growth, reaching sizes of tens of micrometers.

4.1.1 Ion implantation procedure in stainless steel

The ion implantation experiments on AISI 316L samples were performed with the 500 KV HVEE ion implanter from the Laboratório de Implantação Iônica (UFRGS). The functioning of an ion implanter is described elsewhere [1,2].

The solution-annealed AISI 316L samples are implanted with inert gas ions. This implantation is performed because inert gases are sub-products of neutron induced nuclear fission of the matrix atoms and their presence in the matrix affects in distinct ways the microstructure evolution during irradiation processes. The production of these gases due to nuclear reactions is an important factor in the formation of defects observed in irradiated materials. In fact, some of the main observed effects are the

embrittlement and the swelling caused by the formation of nanocavities and bubbles, which cause the deterioration of the mechanical properties of the materials.

Helium is the most abundant inert gas sub-product of the neutron induced fission reactions. However, in this work, Ar ions were chosen due to two specific reasons: i) the study focuses on fuel cladding materials, which are in direct contact with the Uranium-based nuclear fuel. In this particular case, there is an abundant production of Xe by the U fission reactions, which tends to be implanted into the cladding surface in contact with the fuel; ii) the maximum energy of the ion implanter (450 kV) renders a very shallow implantation depth of Xe atoms in an austenitic steel matrix. In this case the experimental studies would become very difficult to be performed because the region of interest of the sample would correspond to a very narrow layer at the surface. Therefore, Ar was chosen as a case-study inert gas element that could be implanted deeper into the matrix and yet better represent a heavy inert gas behavior as compared to He.

Ar ions with energies of 430, 200 and 100 keV were implanted in the steel samples with fluences chosen so that the Ar implantation profile was like a plateau uniformly distributed through a depth of 250 nm. The implantation parameters were chosen by calculating the concentration as a function of depth (Equation 3.2) and the concentration-depth profile for Ar can be seen in Chapter 3, Fig. 3.2 (b). Table 4.1 shows the energy and fluence parameters chosen for the Ar implantation.

Table 4.1 Energies and fluences of Ar implantation

Energy (keV)	**Fluence (at./cm²)**
430	2.5×10^{15}
200	9.5×10^{14}
100	4.25×10^{14}
Soma	3.875×10^{15}
Concentration (íon/cm³)	1.6×10^{21}

The total fluence is equivalent to 0.25 at.% of Ar in relation to the sample. This data is obtained considering that the density of the matrix is 8 x 10^{22} at/cm² and that the implanted region is approximately 250 nm thick. Then we have that:

$$8x10^{22} \text{ at/cm}^3 * 2.5 \times 10^{-5} \text{ cm} * 0.25\% = 4x10^{15} \text{ at/cm}^2,$$

which is approximately the total sum of the fluences.

The samples are implanted with Ar ions at room temperature and with ion currents always below 500 nA/cm² to avoid sample heating during the implantation.

The samples implanted with Ar are then annealed in high vacuum at 550 ºC for 2 hours to induce the nucleation of Ar bubbles. The annealing temperature and time were chosen to avoid second phase precipitations, following the temperature to time transformation diagram shown in Fig. 4.2 [3] below:

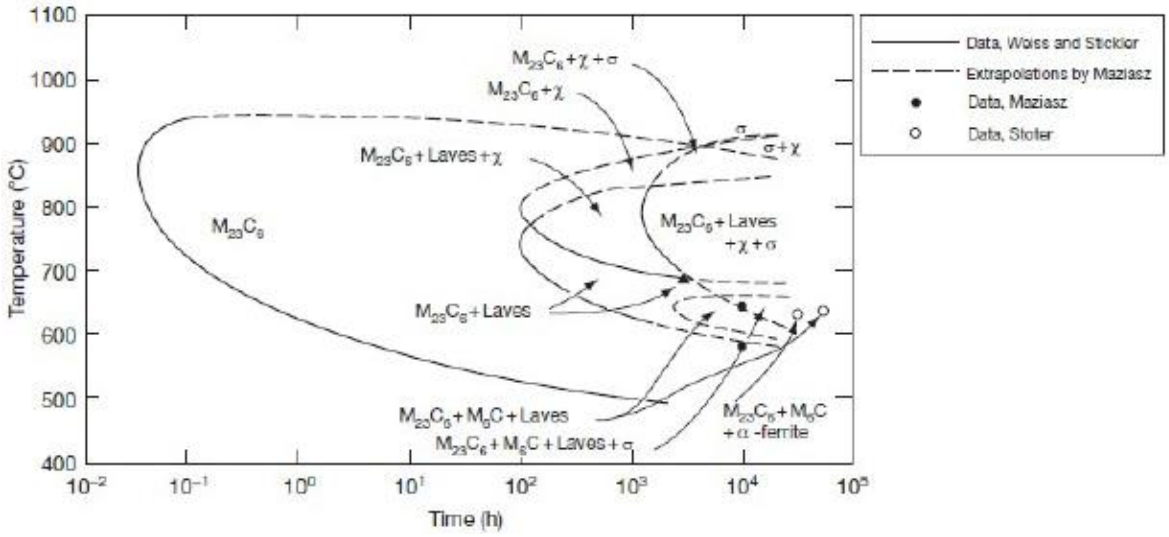

Fig. 4.2 Graph showing the relation between the temperature of formation of precipitates as a function of time

4.1.2 Irradiation procedure

After the Ar implantation and after the thermal annealing at 550 ºC/2h, the samples are submitted to the irradiation step. To compare results, samples that were not implanted are also irradiated. AISI 316L steel samples are placed in a copper sample holder and secured by a steel mask, as shown in Figure 4.3 (a). The sample holder with the specimens properly attached is then attached to another holder that is inserted into

the accelerator chamber. Figure 4.3 (b) shows the final configuration of the sample holder with the samples in the irradiation chamber. The steel shutter is used to cover the samples that have already been irradiated until their final fluence, keeping exposed to the ion beam only the top of the sample holder with the samples that still need to reach a higher irradiation fluence.

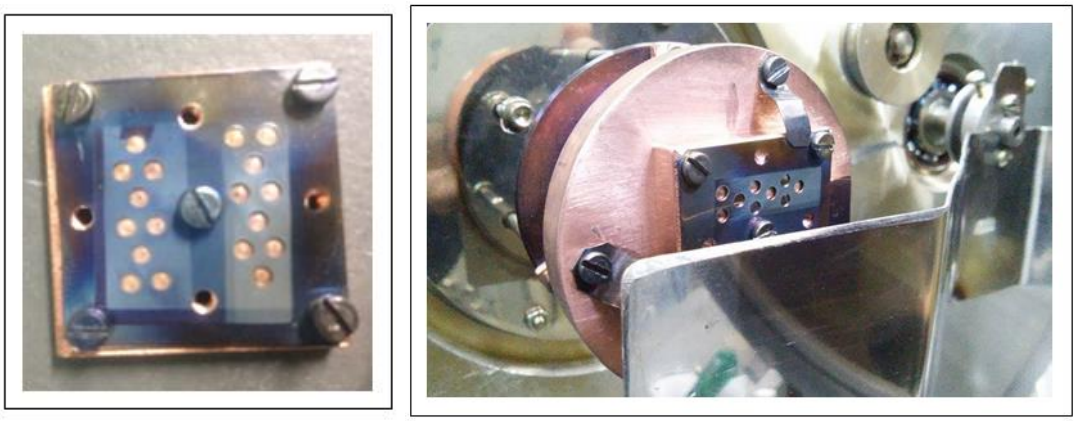

Fig 4.3 (a) Cu sample-holder of 4 cm² with the steel mask. (b) Sample-holder fixed in the irradiation chamber

The steel samples were irradiated with Au and Ag ions. The irradiation parameters are shown in Table 4.2. For all irradiations performed, ion fluences equivalent to 20 and 40 dpa were reached. The ion parameters were chosen to reproduce the same irradiation and vacancy generation profiles for all ions, so that the amount of dpa for both Au and Ag was the same. Therefore, we seek to verify if the morphology of the damage generated by irradiation depends only on the dpa, as it is generally considered in the literature, or if the ion species and ion flux have any influence on the results.

Table 4.2: Irradiation parameters

Ion	Mass (a.m.u)	Energy (MeV)	Dose (at/cm²)	dpa	Temperature (ºC)
Au	196.96	5.0	$5.0x10^{15}$ $1.0x10^{16}$	20 40	550
Ag	107.86	3.5	$1.2x10^{16}$ $2.4x10^{16}$	20 40	550

Figure 4.4 shows the dpa and ion concentration depth profiles calculated with SRIM for Ag and Au irradiations.

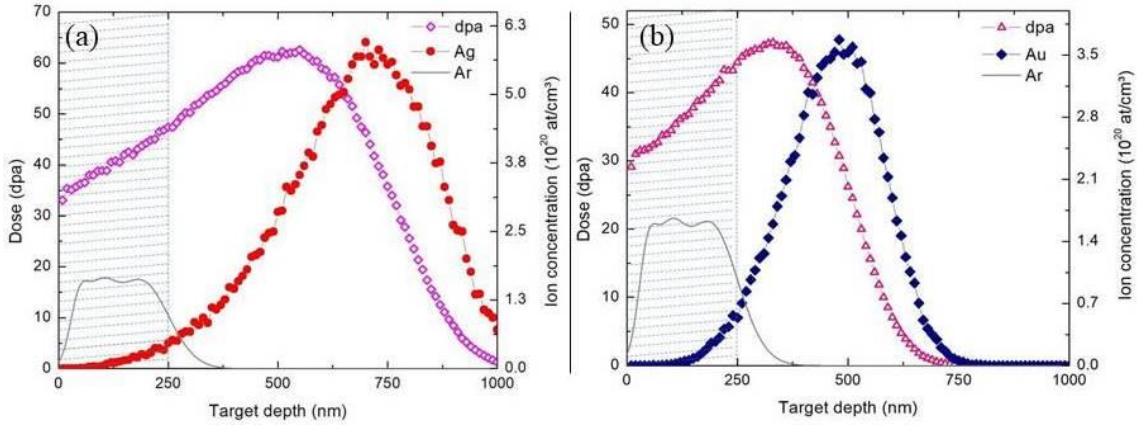

Fig 4.4 Dpa and ion concentration depth profile of (a) Ag and (b) Au irradiation experiments.

Au ions were chosen initially because they are heavy ions, producing large collision cascades without the need for very high doses of irradiation. In addition, the Au beam is easily produced in the LII accelerator by the triple ionization of the ions, which means that the resulting ion beam is more intense and stable. Ag is an intermediate mass element and its beam is also relatively stable, and since it is a lighter ion, it generates fewer collision cascades than Au. In this case, higher irradiation doses are required to produce the same atomic displacements of 20 and 40 dpa.

4.2 Experimental procedures in Chromium (di)silicide - $CrSi_2$ samples

In this work, the experiments were performed on 280 nm thick $CrSi_2$ thin films deposited on silicon substrate. The deposition was performed by the chemical vapour deposition technique (CVD). For the deposition of the $CrSi_2$ film, a $CrSi_2$ target with purity of 99.95% supplied by Neyco was used. A SiO_2 sublayer with a thickness of 25 nm was also deposited by sputtering prior to the $CrSi_2$ layer deposition.

The CVD technique consists basically in the ejection of the surface atoms of a target material (cathode) by the bombardment of ions of an inert gas created inside a plasma and depositing these ejected atoms in a substrate located at the anode level. Initially, a plasma is obtained by applying an electric field on the gas (Ar) which is maintained at low pressure (2×10^{-6} mbar). The field strength is adjusted so that it reaches the rupture stress value of the gas and a high voltage arc forms between two electrodes, which generates a magnetic field inside the chamber with consequent formation of many free electrons and ions. Ar ions are attracted to the cathode with sufficient energy to break the bonds of the atoms of the target material, which are ejected toward the substrate and where they finally settle, forming the film. The $CrSi_2$ films were obtained through Plassys MP4505 equipment from the Center for Micro and Nano-electronic Technology (CTM) of the University of Montpellier.

4.2.1 Ion implantation in $CrSi_2$

Three implantation experiments were performed on distinct sets of $CrSi_2$ samples. The first set was implanted at room temperature with a plateau of Ne ions reaching an average concentration of 1.0 at%. This implantation was carried out with the objective of analyzing the influence of defects generated by the implantation of an inert gas in the material. In a second set of samples, Ne implantation was held at 250 ºC. Finally, a third set of samples was implanted with a plateau of Al ions with an average concentration of 0.008 at%. Table 4.3 shows the implantation parameters used in $CrSi_2$ experiments.

Table 4.3: $CrSi_2$ implantation parameters

Ne		**Al**	
Room temperature and T=250 ºC		Room temperature	
Energy (keV)	**Fluence (at/cm²)**	**Energy (keV)**	**Fluence (at/cm²)**
250	$1x10^{16}$	200	$1x10^{14}$
120	$7x10^{15}$	90	$4.5x10^{13}$
50	$4x10^{15}$	40	$1x10^{13}$
20	$1.5x10^{15}$	30	$1x10^{13}$
Concentration (at.%)			
~ 1.0		~ 0.008	

The concentration depth profiles of Ne and Al implantations performed by SRIM calculations are shown in Figure 4.5 (a) and (b), respectively.

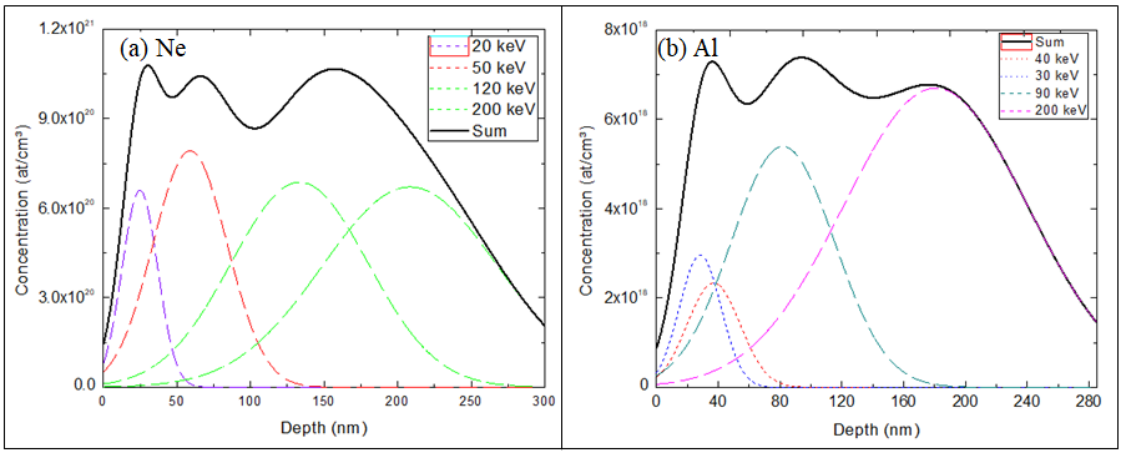

Fig. 4.5 Concentration depth profiles of (a) Ne and (b) Al implantations in $CrSi_2$ thin films

Additional Al ion implantations were held at a higher concentration level (high dose) at room temperature and at 250 ºC. The parameters of these experiments are shown in Table 4.4.

Table 4.4: High dose Al implantation parameters

Al	
Room temperature and T=250 ºC	
Energy (keV)	**Fluence (at/cm²)**
250	$8x10^{15}$
120	$3.6x10^{15}$
50	$8x10^{14}$
20	$8x10^{14}$
Concentration (at.%)	
~ 0.64	

The ion implantation current during all experiments was also maintained below 500 nA/cm².

4.2.2 Electrical resistivity measurements

The electrical resistivity measurements on $CrSi_2$ thin layers are carried out between 80 K and 330 K by the van der Pauw method using the Ecopia HMS 5000 equipment. This method consists in symmetrically and orthogonally arranging four electrical contacts close to the edges of the sample (denoted A, B, C and D in Figure 4.6). Then, an electric current I applied between two adjacent contacts induces a voltage V between the other two contacts.

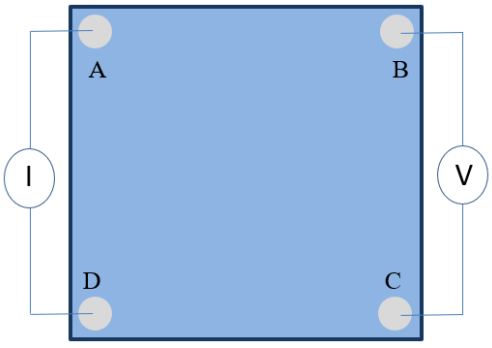

Fig. 4.6 Configuration of the electric contacts for the van der Pauw method

The voltages for the different pairs are then measured (I_{AB}, V), (I_{BC}, V_{DA}), (I_{CD}, V_{AB}), (I_{DA}, V_{BC}), (I_{-AB}, V_{-CD}), (I_{-BC}, V_{-DA}), (I_{-CD}, V_{-AB}) and (I_{-DA}, V_{-BC}). The electrical resistivity ρ is calculated according to the relation:

$$\rho = \frac{\pi . t . V}{2 . I . \ln(2)} f, \tag{4.1}$$

where t is the thickness of the thin layer, V is the average value of the four measured voltages and f is the correction factor of van Der Pauw method. The value of f depends on the ratio $R_{AB,}/R_{BC,DA}$ and is in most cases equal to 1. The electrical contacts were made with In droplets. The measurements are made for five currents between -2.00 and 4.00 mA. A linear relation is verified by Joule effect between I and V showing the ohmicity of the contacts and the absence of heating of the layer.

4.3 Transmission electron microscopy

Transmission electron microscopy (TEM) is a technique used for the analysis and characterization of the microstructure and morphology of solid materials, basically consisting of the obtention of information due to the interaction of accelerated electrons with the atoms from the target material. The electron beam of a transmission electron microscope has typical energies between 80 and 300 keV. A schematic representation of the TEM components and a brief description of its functioning is described in Ref. [4]. In this work, two microscopes were used: the JEOL JEM-2010 equipped with a LaB_6 filament operating at 200 kV from the *Centro de Microscopia e Microanálise* (CMM – UFRGS) was used for the samples' microstrutural analyses and the JEOL 2200FS equipped with a Field Emission Gun (FEG) operating at 200 kV from the *Plateforme de Microscopie Electronique et Analitique* (MEA - Université de Montpellier), France, was used for both the microstrutural and chemical composition characterization of the samples.

4.3.1 Sample preparation

4.3.1.1 316L stainless steel

For the analysis in a transmission electron microscope, the samples of interest must undergo a new process of polishing and thinning. The stainless steels samples used

in the previous experimental steps already have the specific diameter of microscopy samples. The samples are glued with a special wax on an acrylic stub, with the surface of interest facing down. The stub is attached to a grinder and taken to the high-speed polisher where the sample is thinned to a thickness of approximately 60 μm. The stub with the sample is then taken to the dimple grinder, where another mechanical thinning using a steel polishing disc and 3 μm diamond paste is performed. In this apparatus, the central region of the sample is thinned (the disk digs a dimple in the sample) to a thickness between 35 and 40 μm. A final fine polishing is then performed in the dimple with felts and diamond pastes with granulometries of 1 and ¼ μm. The sample is detached from the stub, glued in a new support and is submitted to an ionic thinning process carried out in the ion milling equipment. In the ion milling process, two 4 keV Ar ion beams are accelerated to the sample at angles of 5º or 6º, which rotates in the chamber until a tiny hole in the sample is produced. The areas of the edge of the hole(s) will be the regions of interest analyzed in the TEM, since they are extremely thin regions (~ 100 nm). At last, a final thinning in the ion milling is performed. This thinning is done with 1 keV Ar ions impinging on the sample at an angle of 3º aiming to improve the surface uniformity of the edge of the hole. The ion milling process does not introduce any damage in the region of interest because the energy used is very low and the effect is only to improve the surface morphology of the sample. After this final step, the sample is ready to be analyzed in a TEM microscope. Figure 4.7 shows how the sample looks after all these processes.

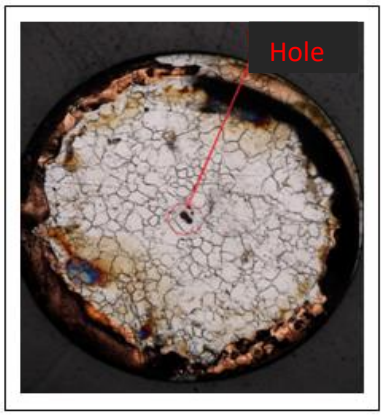

Fig. 4.7 Optical microscopy of the AISI 316L sample prepared in plan-view geometry for transmission electron microscopy

4.3.1.2 Chromium (di)silicide - $CrSi_2$

The $CrSi_2$ samples were prepared in the cross-section geometry for observation in the TEM using the Focused Ion Beam (FIB) technique. This technique consists of the use of a beam of extremely focalized Ga ions to cut a lamella with variable thickness (between tens and hundreds of nanometers) in the region of interest of the sample. This lamella is then removed and "glued" to a grid. Prior to cutting, a thin layer of C followed by a thicker layer of Pt is deposited on the surface in order to protect the surface of the sample and to aid in the manipulation and the subsequent gluing of the lamella in a grid.

Figure 4.8 shows the FIB grid already mounted on the TEM sample holder. The four "teeth" observed in images a, b and c are where the samples of interest are glued. Figs. 4.8 (a), (b) and (c) were made in magnifications of 1, 5 and 10 times in an optical microscope. The image in (d) shows a zoom of the "teeth" of the image in (c), where $CrSi_2$ samples are glued to the two central teeth.

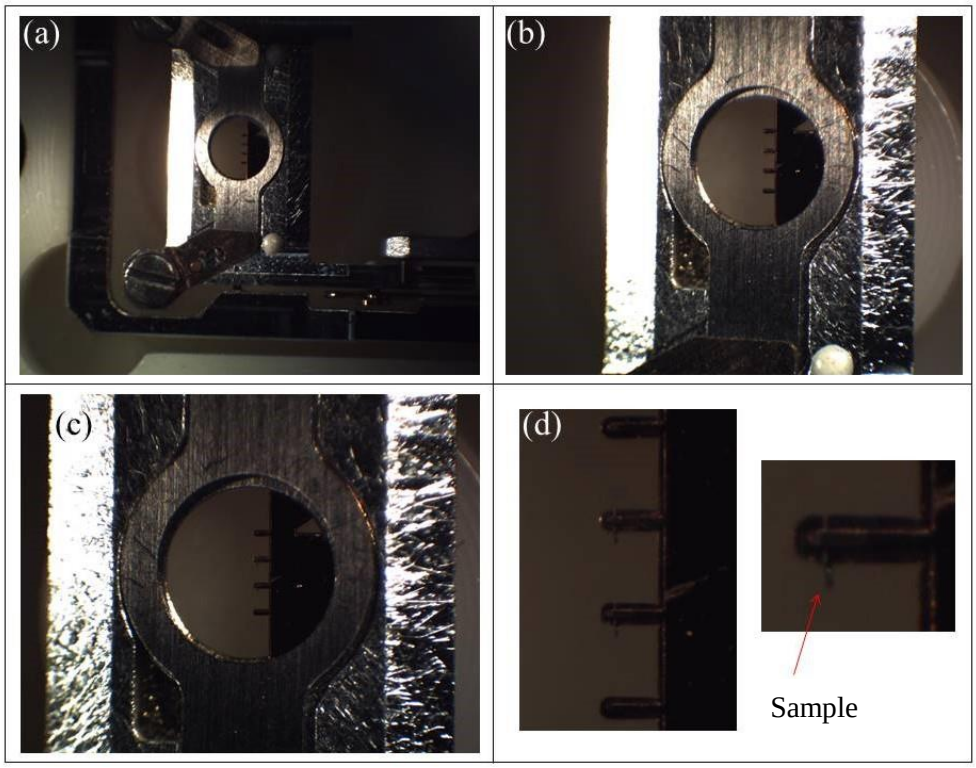

Fig. 4.8 Optical microscopy of two cross-section $CrSi_2$ samples prepared by FIB for TEM analysis. Magnifications of (a) 1x, (b) 5x, (c) 10x and (d) *zoom* of the two central “teeth” shown in (c) where the samples are glued

Figure 4.9 shows a scanning electron microscope (SEM) image of the final geometry of the sample after FIB preparation. The magnification is of 11000X. The thicker regions of the sample serve as a "support" to the sample itself, since it makes it firmer and less susceptible to breaking. The thinner regions (lighter contrast) are the regions that have the optimal thickness for observation in the TEM. The $CrSi_2$ thin film can be seen as a darker band that runs through the entire sample.

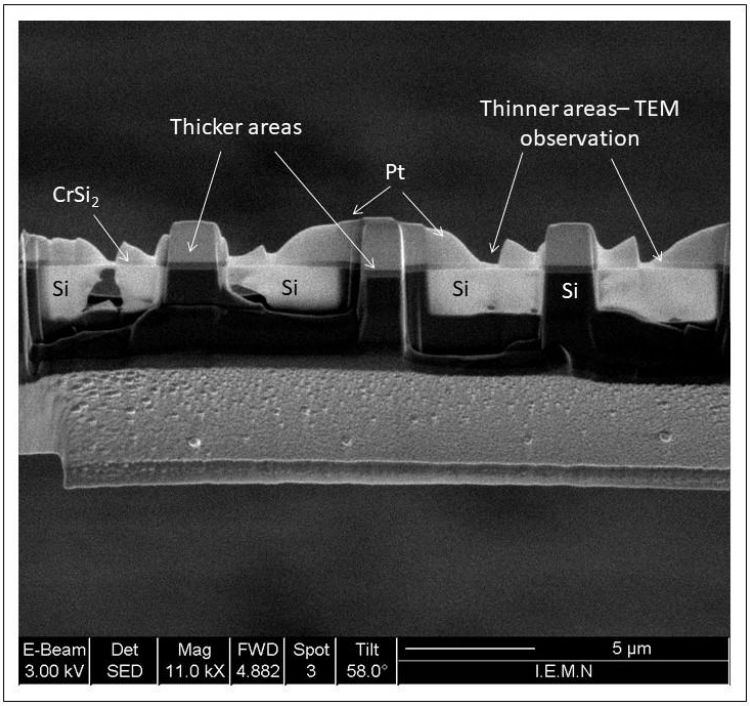

Fig. 4.9 Scanning electron microscopy of a *cross-section* $CrSi_2$ sample prepared by FIB for TEM analysis. 11000 X magnification

The sample preparation by FIB was performed at the *Institut d'électronique, de microélectronique et de nanotechnologie* (IEMN), in Villeneuve d'Ascq, France.

4.3.2 Imaging Contrasts

The information obtained with the transmission electron microscopy technique comes basically from the elastic and inelastic scattering processes that occur in the interactions between the electrons from the beam and the nuclei and electrons of the sample's atoms. In the elastic scattering, the accelerated electrons interact with the effective Coulomb potential of the atomic nuclei, and there is no energy loss. If this interaction does not carry structural information, that is, if it occurs only with an atom,

it is said that an incoherent scattering occurred. If this interaction occurs with several atoms, the scattering (at a high angle) is considered coherent, giving rise to the diffraction phenomenon, which can be described by Bragg's Law. The diffraction is essential to obtain information about the crystallography of the sample. In the inelastic scattering, the electron-electron interactions cause the energy loss of the incident electron as well as its deflection at low angles [5]. This set of interactions will give rise to the images generated by the microscope, and the information contained in these images is determined by certain conditions of contrast that are discussed as follows:

I. **Mass-thickness contrast**: depends on the different atomic numbers of the elements present in the sample or on the combination of density and thickness of the sample, since the more scattering centers present in the trajectory of the incident electron the greater the chance of it being inelastically scattered. It is possible to introduce the objective aperture to select only the electrons that have scattered, resulting in a darker image in the regions that have a greater number of scattering centers, generating a contrast between regions with different densities or different thicknesses.

II. **Diffraction contrast**: occurs due to the coherent elastic scattering of electrons, which interact as waves scattered simultaneously by several atoms at the specific angles determined by Bragg's Law. The lens aperture can be used to obtain dark field (DF) and bright field (BF) images, since with this aperture it is possible to choose which one of the transmitted or diffracted beam will pass through it. The diffraction contrast allows differentiating regions in the sample that present extended defects and crystalline structures. From the obtained diffraction patterns one can, for example, identify existing structures in the matrix, such as precipitates and nanocrystallites.

III. **Phase contrast (Fresnel fringes)**: it is a result from the interference of waves that are scattered with a phase difference. The phase difference occurs when the wave travels through regions that have different densities or thicknesses, as in regions that present grain boundaries, cavities or interfaces, among other things. This effect is only observed when the objective lens is placed out of focus, i.e., in underfocus or overfocus conditions. In underfocus, cavities and bubbles, for

example, appear as light regions surrounded by a black ring (Fresnel fringes). In overfocus, the same objects appear as dark areas surrounded by a white ring.

IV. **Phase contrast (lattice image/high resolution image)**: the beam is aligned to a crystalline zone axis, generating several diffraction "spots". An image of the periodicity of the diffracting crystalline planes is produced due to the phase difference between the diffracted and direct electron beams and also due to imperfections in the objective lens.

4.3.3 Analytical techniques

4.3.3.1 Energy dispersive X-ray spectroscopy (EDX)

This technique is used for elemental analysis or chemical characterization of a sample. It basically consists of the use of the electron beam of the transmission electron microscope for the excitation of the atoms of the sample with consequent emission of radiation in the X-ray frequency band. The interaction between the electron of the beam with the atoms of the target can generate two types of X-rays:

- **Characteristic X-rays**: result from the interaction between inner energy orbitals: the atom is ionized due to the removal of an electron from an inner layer by inelastic scattering. When an electron from an outer layer "falls" to that energy level a photon (X-ray) with energy equivalent to the energy difference between each level is emitted (Figure 4.10 (a)). As the ionization energy for each electronic shell of each chemical element is specific, it is possible to identify the elements present in the sample, whose signals will appear as well defined peaks in the energy spectrum (Fig. 4.10(b)).

- **Bremsstrahlung X-rays**: produced by the deceleration of the electrons of the beam by the electric fields present around the nucleus of the atoms. In this inelastic interaction, the incident electrons lose energy and change direction. Part of the energy lost is converted to X-ray. In the EDX spectrum, the X-ray signals of Bremsstrahlung will be seen as a continuous signal, and they are considered as a background signal (Fig. 4.10(b)).

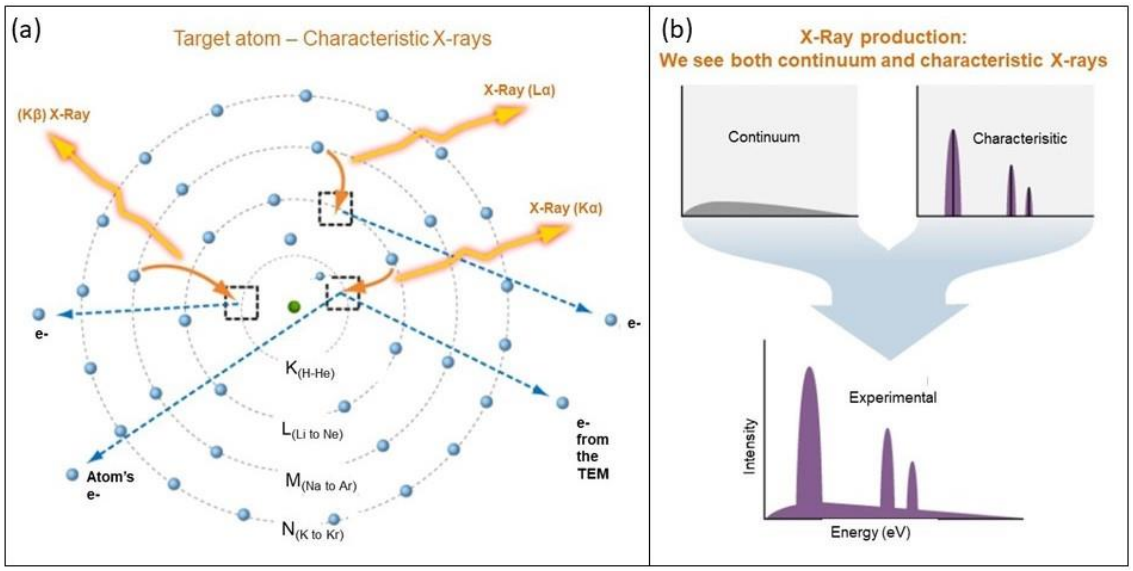

Fig. 4.10 (a) Production of characteristic X-ray by the transition involved in the generation of Kα, Kβ and Lα x-rays; (b) the resulting EDX spectrum is composed by the characteristic X-ray peaks superimposed with the continuum (Bremsstrahlung X-rays). Adapted from [6]

The detection of the X-ray signals occurs as follows: the energy of the X-ray arriving at the detector is dissipated by the generation of a series of electron-hole pairs in the semiconductor crystal that makes up the EDX detector. The number of pairs is directly proportional to the energy of the X-rays. A voltage is then applied throughout the crystal, which causes the pairs to migrate to electrodes that are on opposite sides of the crystal. This movement causes a charge pulse that is amplified by a sensitive preamplifier. The final pulses are proportional in height to the incident X-ray energy.

4.3.3.2 Diffraction

Diffraction is a phenomenon that will be of great importance in the scope of this work because through it will be possible to perform the identification of the phases formed in the implanted and irradiated materials. In this subsection it will be presented the main concepts of diffraction, with a special focus on the diffraction of electrons.

Generally speaking, diffraction is basically "an interaction between a wave and an object" [7]. In this interaction, the incident wave will be scattered by the target's atoms in all directions. However, it will only be possible to "see" scattering events that occur in certain directions determined by the Bragg's Law [7]:

$$n\lambda = 2dsen\theta. \qquad (4.2)$$

The Bragg's Law states that the path difference between waves scattered by adjacent lattice planes must be a multiple of the wavelength of the incident radiation, i.e., the scattered waves must be in phase for a constructive interference.

The Bragg's Law can be represented geometrically through the Ewald Sphere (Fig. 4.11) [7,8]:

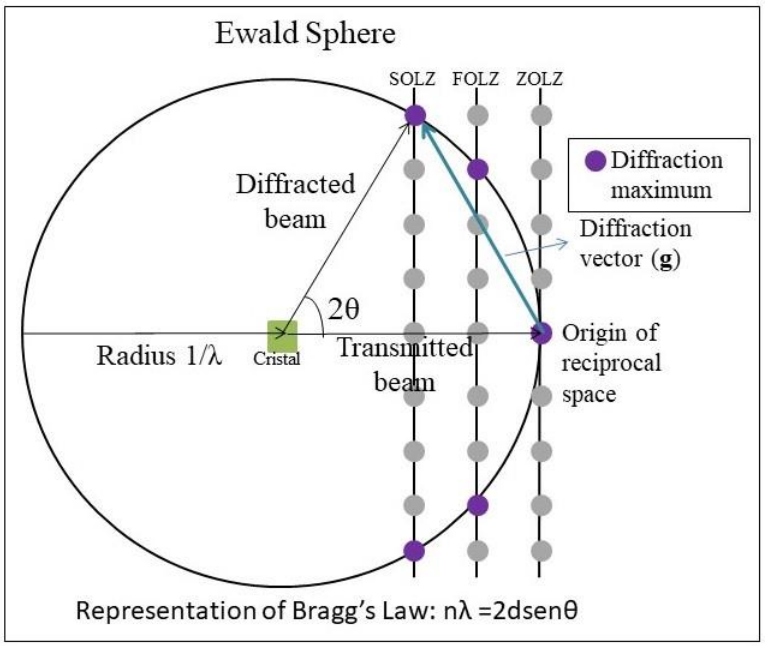

Fig. 4.11 Geometrical representation of the Ewald sphere.

$$\sin\theta = \frac{g/2}{1/\lambda} = \frac{1/d_{hkl}}{1/2\lambda} = \frac{\lambda}{2d_{hkl}} \tag{4.3}$$

where g is the diffraction vector and d_{hkl} is the interplanar distance. The acronyms ZOLZ, FOLZ and SOLZ represent, respectively, the Zero Order Laue Zone, the First Order Laue Zone and the Second Order Laue Zone.

The Ewald sphere is an important concept that relates the wavelength of the incident radiation to the diffraction pattern that will be generated. For electrons and X-rays, the size of the sphere will be different; consequently, the information obtained through the diffraction of these waves will be different.

Electrons with typical energies of a transmission electron microscope (100 to 300 keV) interact strongly with matter (electrons are scattered both by the nuclei and

electrons of the atoms of the material), making it possible to obtain information on the crystalline structure of nanometric materials both through diffraction and through the acquisition of high resolution images.

The wavelength of these electrons is so small (0.037 - 0.020 Å) that the radius of the Ewald sphere becomes very large, which promotes the intersection of the sphere with more points in the reciprocal lattice, that is, a larger number of reflections fulfills the diffraction condition at the same time. In the case of electron diffraction, the ZOLZ points are the most detected due to the very large radius of the Ewald sphere.

Due to the great power of interaction of electrons with matter, multiple scattering events can occur for each reflection (dynamic approximation). However, the amount of information obtained can prevent a correct analysis of the data. To minimize this effect, the sample should be as thin as possible.

From the diffraction pattern, it is possible to obtain information about the lattice parameter of the object being observed. For polycrystalline samples, the diffraction pattern will be composed of concentric rings. The information obtained through the diffraction is in the reciprocal space, which can be related to the real space through the following equation:

$$g = \frac{R\lambda}{d}, \tag{4.4}$$

where g is the radius of the ring in the diffraction pattern, R is the camera length, λ is the wavelength of the electrons and d is the interplanar spacing in the real space. Since the values of R and λ are known, the relationship between g and d is directly obtained:

$$g = \frac{1}{d} \rightarrow d = \frac{1}{g}. \tag{4.5}$$

This relation will be of great importance for the diffraction analyses described in Chapters 5 and 6.

References

[1] F.P. Luce, Estabilidade de Nanopartículas Em Sílica: Efeitos Térmicos e de Irradiação Com Elétrons e Íons Energéticos, Universidade Federal do Rio Grande do SUl, 2012.

[2] F. Kremer, Formação de Ilhas Metálicas de Sn e Pb Em Interfaces SiO2/Si e SiO2/Si3N4 via Implantação Iônica e Tratamento Térmico, Universidade Federal do Rio Grande do Sul, 2010.

[3] P.J. Maziasz, J.T. Busby, Comprehensive Nuclear Materials - Volume 2, Elsevier B.V., 2012.

[4] M.M. Timm, Efeitos Da Irradiação de Elétrons Sobre a Formação e Estabilidade de Nanopartículas de Au Em Filmes de Si3N4, Universidade Federal do Rio Grande do Sul, 2015.

[5] L. Reimer, H. Kohl, Transmission Electron Microscopy, 2008.

[6] C. Zheng, Metallic Oxide Nano-Clusters Synthesis by Ion Implantation in High Purity Fe10Cr Alloy, Université Paris-Saclay, 2015.

[7] D.B. Williams, C.B. Carter, Transmission Electron Micorscopy - a Textbook for Materials Science, Springer, 2009.

[8] B.D. Cullity, S.R. Stock, Elements of X-Ray Diffraction, Third Edit, Pearson, 2014.

CHAPTER 5

Ion irradiation effects on AISI 316L

The understanding of the physical mechanisms causing the formation of cavities, bubbles and precipitates is crucial for the design and determination of the useful lifetime of components used in nuclear reactors or in other applications involving the radioactive materials, such as the Radioisotope Thermoelectric Generators (TERs). This chapter presents the results from the investigation of the effects on the microstructure produced by heavy ion irradiation into solution annealed AISI 316L stainless steel as a model case material for nuclear fuel cladding. Recently, in a study performed under conditions very similar to those presented here, Jublot-Leclerc et al. showed that 4 MeV Au irradiation at 450 °C and 550 °C causes the formation of cavities either in 316L steel and FeNiCr alloys. The increase of the void sizes is correlated with the increase of the irradiation temperature and fluence [1]. Similarly, Renault-Laborne et al. investigated the formation of M_6C (η), $M_{23}C_6$ (τ), Ni_3Si (γ') and $M_6Ni_{17}Si_7$ (G) phases in 316 steels irradiated with neutrons [2]. It has also been demonstrated that 5 MeV Fe irradiations at 500 °C in 304L austenitic steel up to a damage level of 80 dpa shows that the grain size structure modifies the kinetics of phase transitions, detected as a reduction in the formation of $M_{23}C_6$ type precipitates in 304L samples of ultra-fine grains when compared to the normal 304L steel [3]. These recent studies demonstrate the need for a better understanding of the effects of heavy ion irradiation in nuclear materials.

In this sense, the present study attempts to demonstrate that the effects of heavy ion irradiations depend on the ion mass and irradiation flux (dose rate) and explain the microstructure changes in terms of the kinetics of the vacancy generation and annihilation processes. It is discussed how the formation of carbide precipitates and inert gas-bubbles are affected by the vacancy concentration in the matrix, which is correlated to the irradiation parameters. To further understand the behavior of the vacancies, the microstructure evolution as a function of the irradiation process is investigated comparing samples containing a condensed system of Ar bubbles with

samples without the bubbles. This is done because bubbles typically behave as very effective sink sites for vacancies and therefore increases the vacancy annihilation process. TEM, STEM-EDX and SAD are the main techniques used to investigate the microstructure of the samples. Section 5.1 summarizes the irradiation effects obtained in samples without Ar bubbles and Section 5.2 presents the results for samples containing Ar bubbles. The overall irradiation effects are then discussed in Section 5.3, and the conclusions summarized in Section 5.4.

5.1 Samples without Ar

In this subsection the results regarding the irradiation experiments performed on samples without Ar are presented. Two Au irradiation experiments were performed, one at a high ion flux conditions (13.89 x 10^{11} ion/cm²s, named as Au_{HF}) and other at a low ion flux (5.95 x 10^{11} ion/cm²s, named Au_{LF}). To test for the ion mass effect on the irradiations, the experiments with Au ions are compared with an irradiation with Ag ions (4.17 x 10^{11} ion/cm²s, named Ag_{LF}), which is about 2 times lighter than Au. The flux for the Au_{LF} condition was adjusted to reach about the same ion flux value of the Ag_{LF} condition, which is about a half of the Au_{HF} value. All the irradiation experiments were performed at 550 ºC with fluences equivalent to ≈ 20 and ≈ 40 dpa. The irradiation parameters are summarized in Table 4.2 in Chapter 4.

Figure 5.1 shows a micrograph of an as-prepared sample (non-implanted with Ar and non-irradiated). In this sample, no special microstructure feature is observed. The micrograph shows a grain boundary, which also present a very fine precipitate dispersion.

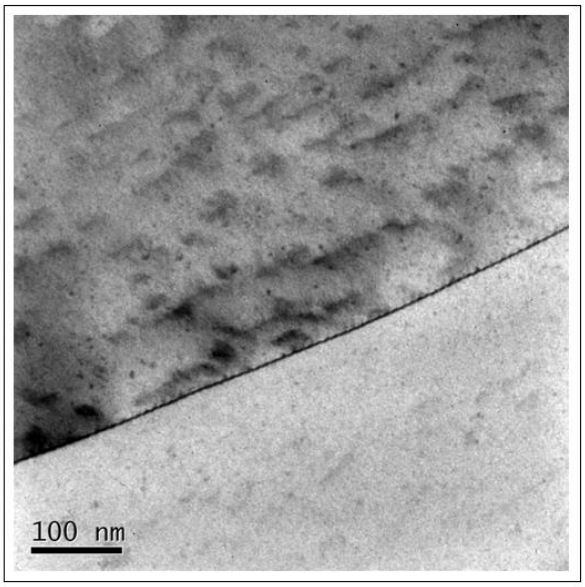

Fig. 5.1 Solution-annealed AISI 316L sample. Magnification of 20.000 X of a region showing a grain boundary.

Comparatively, Figure 5.2 shows that the Au_{HF}, Au_{LF} and Ag_{LF} irradiation processes largely modify the samples' microstructures. The results shown in Fig. 5.2 are relative to a solution annealed AISI 316L sample irradiated up to doses of 40 dpa ($1x10^{16}$ at/cm²), with the substrate heated at 550 ºC. In Fig. 5.2 (a), the Au_{HF} irradiation has induced the formation of dislocation loops, stacking fault tetrahedra and large cavities (white shapes surrounded by a dark fringe). These are typical irradiation effects produced by ions and neutrons, widely known in the literature [4]. The Au_{LF} and Ag irradiations depicted in Figs. 5.2(b) and (c), respectively, show different features: a dense array of small cavities (appearing as white disks surrounded by a dark fringe) and second phase precipitates (appearing as large and dark structures) distributed throughout the matrix. These features are quite distinct from the irradiation-related defects observed in the Au_{HF}.

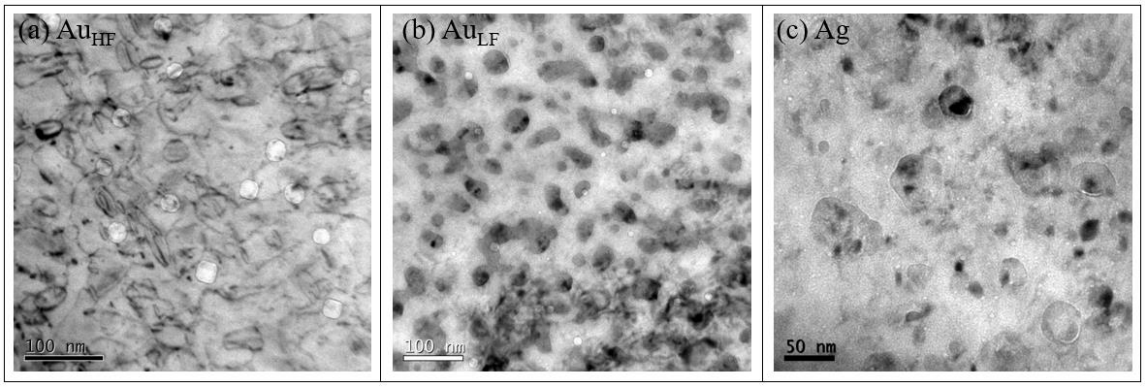

Fig. 5.2 Solution-annealed AISI 316L sample irradiated to ion fluences equivalent to 40 dpa with (a) Au_{HF} ions, (b) Au_{LF} and (c) Ag ions

5.2 Samples with Ar

Figure 5.3(a) shows the TEM micrograph of a sample implanted with Ar and thermal annealed at 550 ºC/2h. The Ar implantation forms a concentration-depth plateau extending from the sample surface to a depth of ≈ 250 nm (Fig 4.4). Even after the annealing procedure, the attained Ar bubble mean size is very small, in the order of 1 nm. Figure 5.3(b) shows a zone axis oriented diffraction pattern from a single grain. This diffraction measurements strongly indicates that the Ar implanted and annealed sample is free from second phase precipitates.

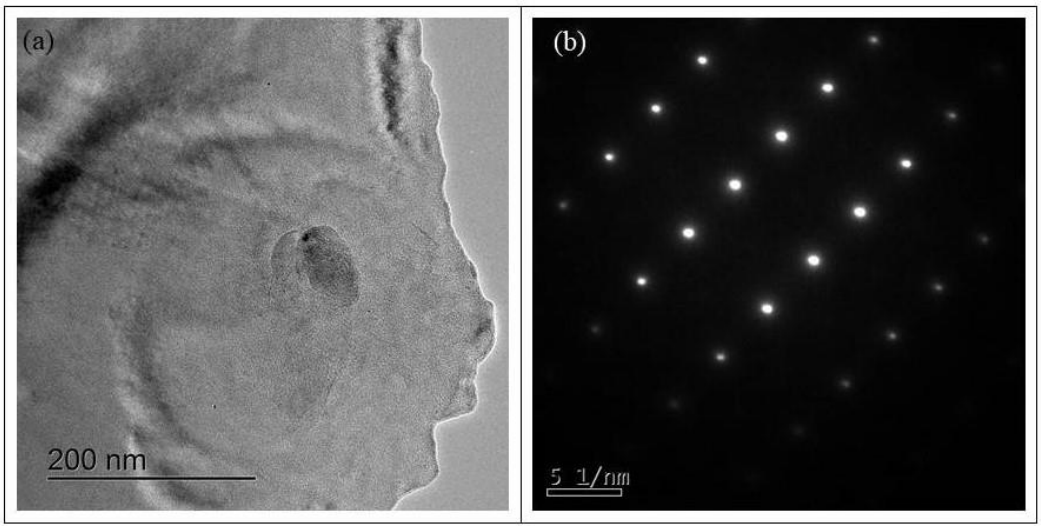

Fig. 5.3 (a) Ar-implanted and annealed AISI 316L sample. (b) Diffraction pattern of the sample shown in (a)

Figure 5.4 shows TEM micrographs of samples implanted with Ar and irradiated at 550 ºC to a fluence of 20 dpa with Au_{HF}, Au_{LF} and Ag ions. After the irradiation experiments, a high density of small cavities is observed. These cavities are filled with the Ar atoms present in the matrix, thus characterized as bubbles. In all these Ar-implanted samples the bubble formation is accompanied by the formation of precipitates.

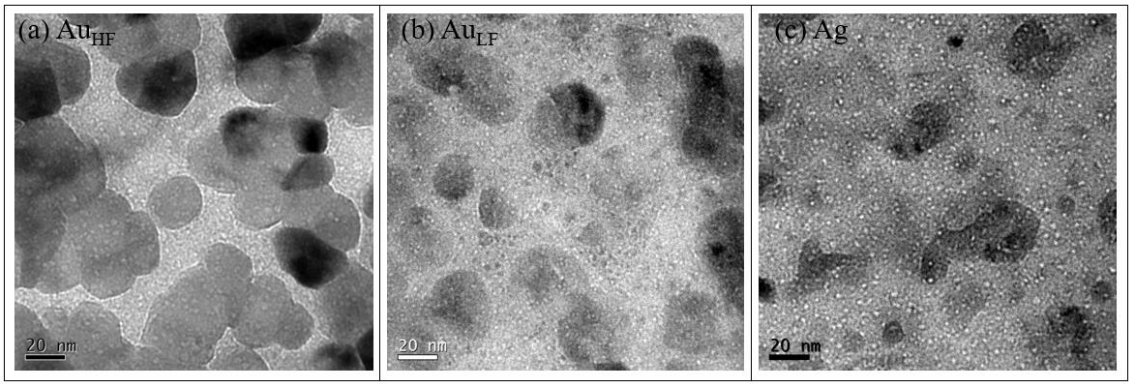

Fig. 5.4 Ar-implanted AISI 316L sample irradiated to ion fluences equivalent to 20 dpa with (a) Au_{HF} ions, (b) Au_{LF} and (c) Ag ions

Similarly, Figure 5.5 shows TEM micrographs of samples implanted with Ar and irradiated at 550 ºC to a damage level of 40 dpa with Au_{HF}, Au_{LF} and Ag ions.

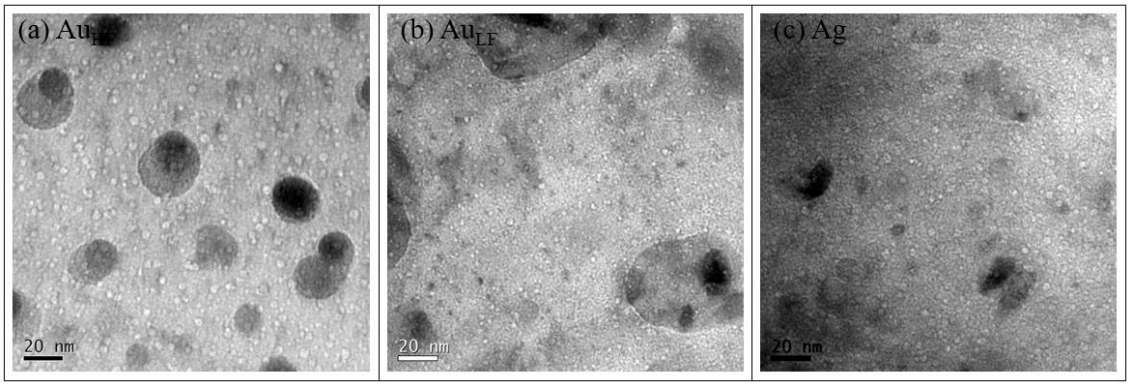

Fig. 5.5 Ar-implanted AISI 316L sample irradiated to ion fluences equivalent to 40 dpa with (a) Au_{HF} ions, (b) Au_{LF} and (c) Ag ions

Similarly to the samples irradiated to 20 dpa, the 40 dpa irradiation cases present precipitates and a dense system of Ar bubbles. This time, however, the bubbles formed

in the 40 dpa case are somewhat larger than the ones formed at 20 dpa. The bubble size distribution for all Ar-implanted samples are presented in Figure 5.6.

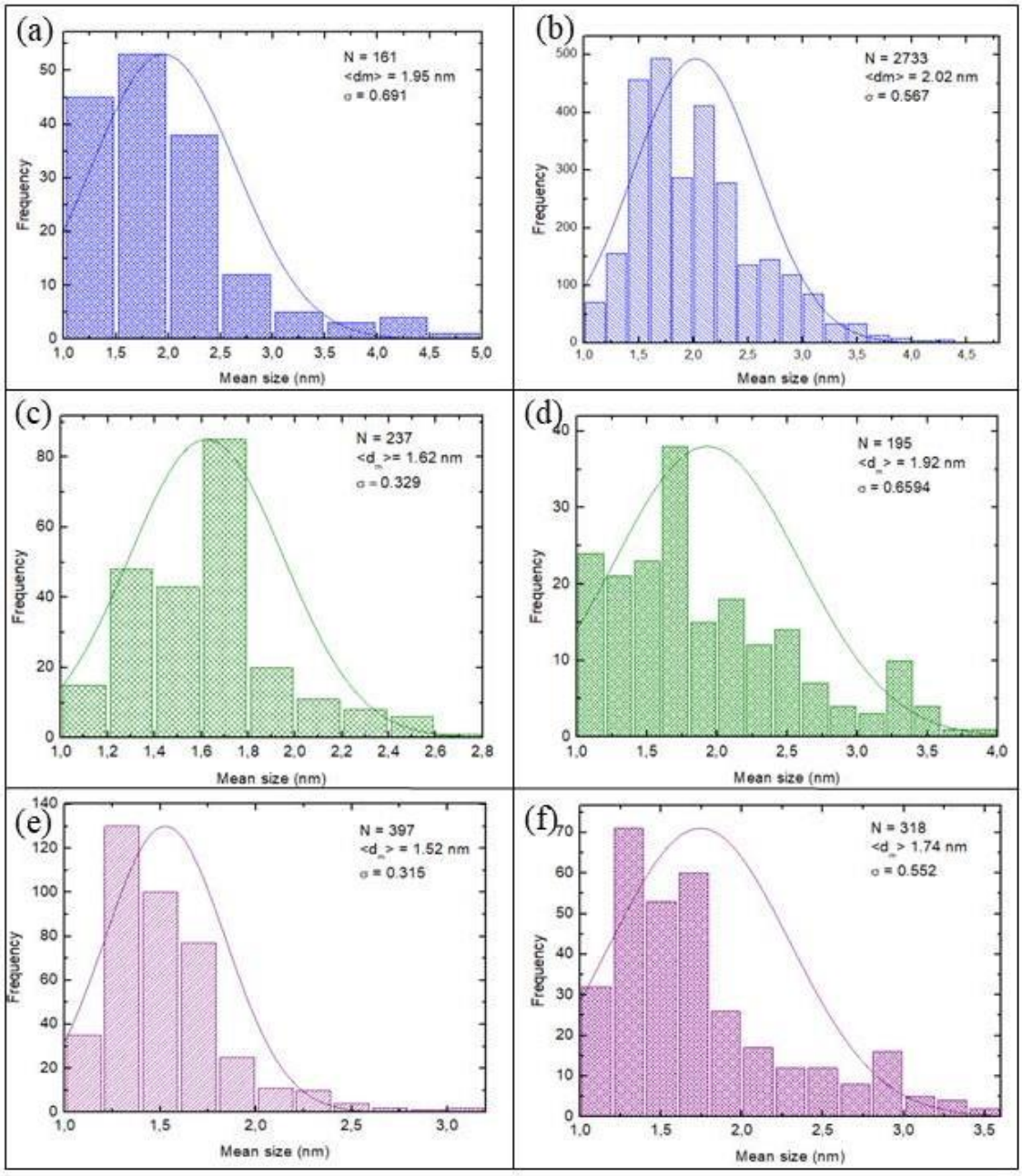

Fig. 5.6 Ar bubble size distribution for AISI 316L samples irradiated with (a) Au_{HF} to 20 dpa, (b) Au_{HF} to 40 dpa, (c) irradiated with Au_{LF} to 20 dpa, (d) irradiated with Au_{LF} to 40 dpa and irradiated with (e) Ag to 20 dpa and (f) Ag to 40 dpa

In all the analyzed cases, the Ar bubble mean size distribution is unimodal and uniform throughout the matrix. The Ar bubble growth behavior as a function of irradiation parameters are further analyzed in Section 5.3.

For a better visualization of the precipitate systems formed during the irradiation experiments in the Ar-implanted samples, TEM micrographs at lower magnifications are presented for the 20 dpa and for the 40 dpa irradiation experiments (Figs. 5.7 and 5.8, respectively).

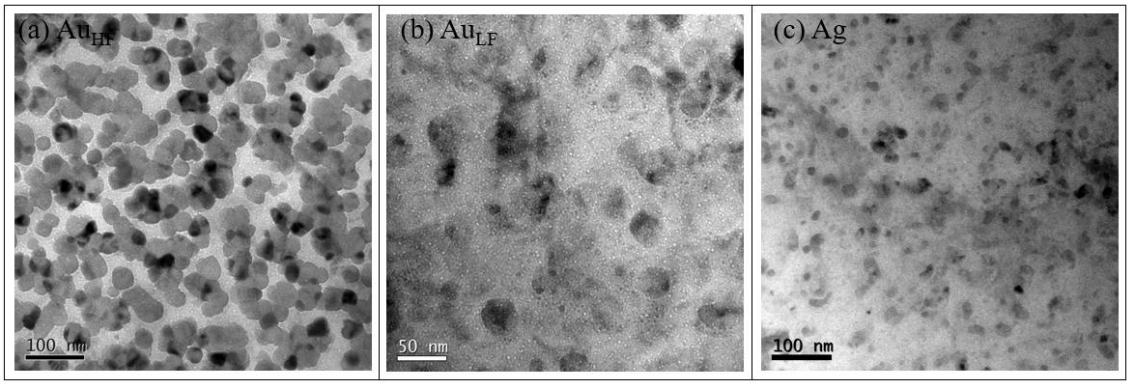

Fig. 5.7 Ar-implanted AISI 316L sample irradiated to ion fluences equivalent to 20 dpa with (a) Au_{HF} ions, (b) Au_{LF} and (c) Ag ions, showing the precipitate system

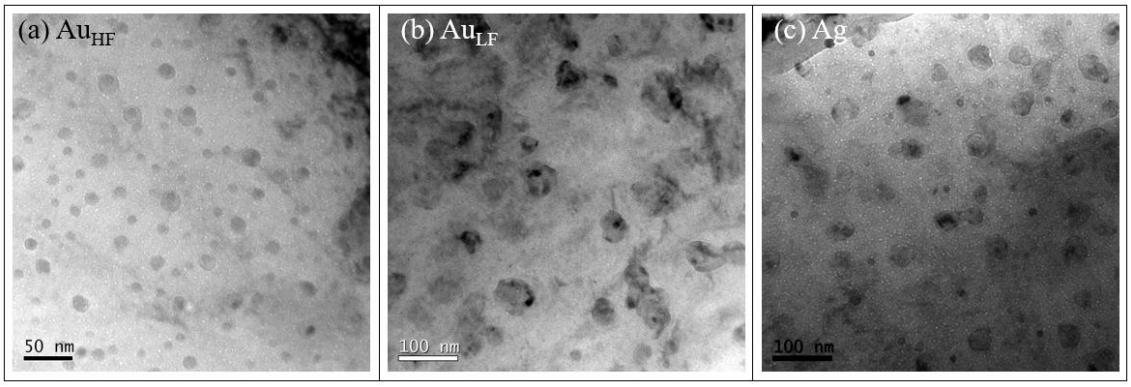

Fig. 5.8 Ar-implanted AISI 316L sample irradiated to ion fluences equivalent to 40 dpa with (a) Au_{HF} ions, (b) Au_{LF} and (c) Ag ions, showing the precipitate system

From the results described above, it is noticed that the Au_{HF} irradiation case presents very distinct results compared to the other samples with and without Ar. This is the only case where no precipitation is observed. In general, the results also show that bubble growth behavior depend on irradiation fluence and on the ion flux, as shown in Fig. 5.6. These results, along with the characterization of the precipitates, are discussed in the next section.

5.3 Discussion

5.3.1 Precipitate formation

The precipitation induced by the present ion irradiation experiments in AISI 316L alloys were analyzed by SAD, EDX and STEM-EDX. These techniques give information about the crystal structure and chemical composition (as described in Chapter 4). The SAD patterns of the Au_{HF}, Au_{LF} and Ag_{LF} irradiations conducted to fluences equivalent to 40 dpa are shown in Figure 5.9.

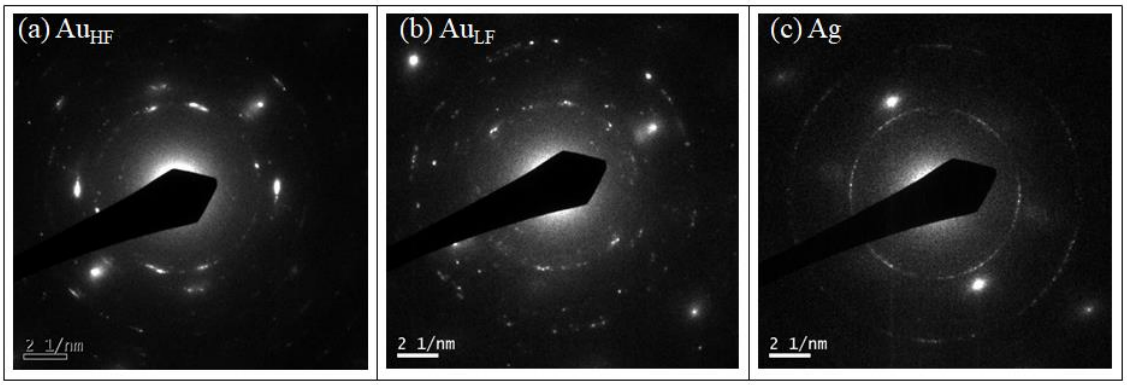

Fig. 5.9 SAD pattern of the Ar-implanted AISI 316L samples irradiated to ion fluences equivalent to 40 dpa with (a) Au_{HF}, (b) Au_{LF} and (c) Ag ions, showing the precipitate system

The EDX measurements from the matrix (Fig. 5.10(a)) and from a single precipitate (Fig. 5.10(b)) of the Au_{HF} irradiated sample with Ar demonstrate that most of the metallic content of the precipitates is similar to the matrix signal except for an enrichment in Cr.

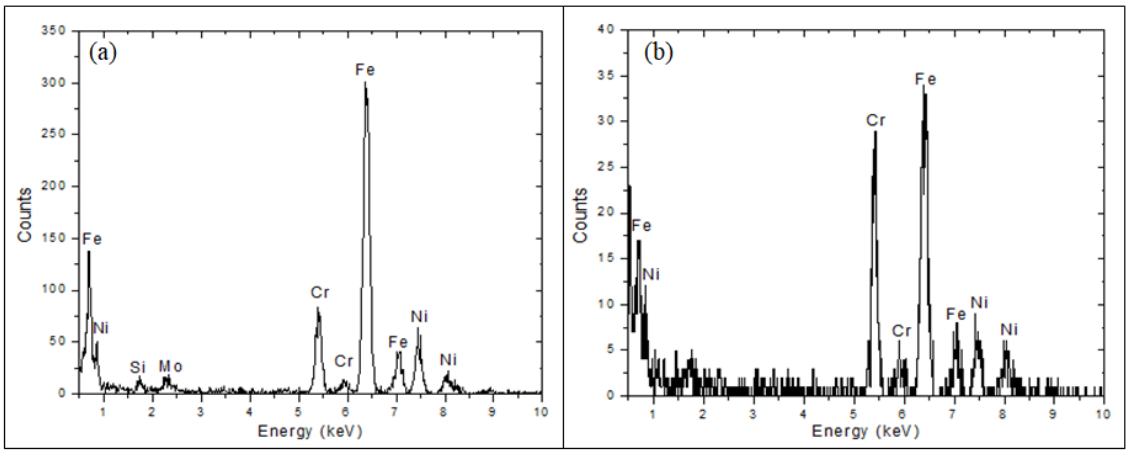

Fig. 5.10 EDX measurement of the Ar-implanted sample irradiated to 40 dpa with Au_{HF} at 550 ºC

The SAD measurements shown in Figs. 5.9 and 5.10 allow the structural characterization, performed more systematically for the Au_{HF} irradiation case. Table 3.1 lists the most common types of precipitates formed by irradiation in austenitic stainless steels. Since the precipitate composition is similar to the matrix, the most probable phases should be the τ ($M_{23}C_6$), η (M_6C) and the MC, where C denotes carbon and M stands for the majoritarian metallic elements (Fe, Cr or Ni). The crystallographic data presented in that table can be used to characterize the precipitates by comparing the experimental diffraction parameters with those calculated from the listed crystall structures. The three phases considered in this study have crystallographic parameters shown in Table 5.1 below:

Table 5.1: Crystallographic data for carbide phases considered in this work [5]

Phase	**Lattice parameter (nm)**	**Symmetry Group**	**Estimated density (g/cm³)**	**Estimated density (at/nm³)**
τ ($M_{23}C_6$)	1.06	Fm-3m (225)	7.877	100.7
η (M_6C)	1.08	Fd3m (227)	7.321	88.9
MC	0.43	Fm-3m (225)	5.67	100.6
Matriz	0.35	Fm-3m (225)	8.02	85.7

The symmetry groups 225 and 227 correspond to the face-centered cubic structure (FCC). By the determination of the Wyckoff positions [4], it was possible to create the atomic model representative of each structure. The Powder Cell code was used to simulate these structures and the necessary diffraction parameters to be compared with the experimental ones. Figures 5.11, 5.12 and 5.13 show the crystal structures and the diffraction data of the allowed planes (Miller index, diffraction angle, interplanar distance and relative peak intensity) for the simulated $M_{23}C_6$, M_6C and MC phases. The simulations were performed considering Fe as the metal content of the structure. This is

done because the atomic scattering factors of the heavy elements (Fe, Cr, Ni) are very similar. The Wyckoff positions were 24d (C) and 96j (Fe) for $M_{23}C_6$, 16d (C) and 96h (Fe) for M_6C and 4a (C) and 4b (Fe) for MC. The densities are: 7.877 g / cm³ ($M_{23}C_6$), 7.321 g / cm³ (M_6C) and 5.67 g / cm³ (MC).

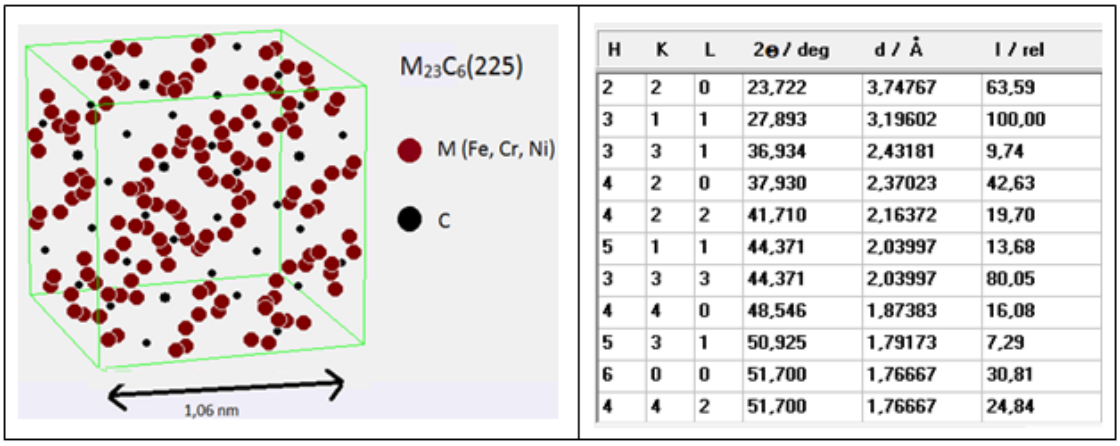

H	K	L	2θ / deg	d / Å	I / rel
2	2	0	23,722	3,74767	63,59
3	1	1	27,893	3,19602	100,00
3	3	1	36,934	2,43181	9,74
4	2	0	37,930	2,37023	42,63
4	2	2	41,710	2,16372	19,70
5	1	1	44,371	2,03997	13,68
3	3	3	44,371	2,03997	80,05
4	4	0	48,546	1,87383	16,08
5	3	1	50,925	1,79173	7,29
6	0	0	51,700	1,76667	30,81
4	4	2	51,700	1,76667	24,84

Fig. 5.11 $M_{23}C_6$ crystal structure simulation and diffraction data of some of the diffraction planes. $M_{23}C_6$ density: 7.877 g/cm³. Wyckoff positions: 24d (C) and 96j (Fe).

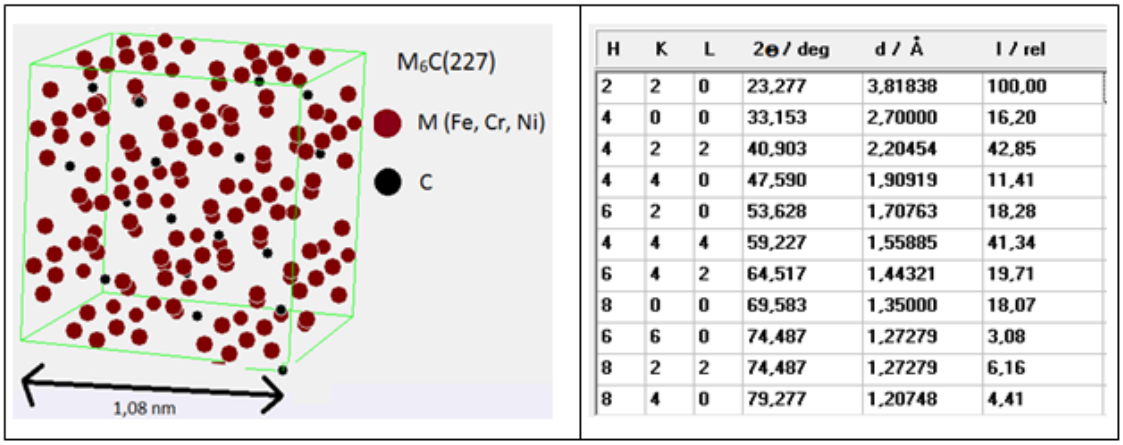

H	K	L	2θ / deg	d / Å	I / rel
2	2	0	23,277	3,81838	100,00
4	0	0	33,153	2,70000	16,20
4	2	2	40,903	2,20454	42,85
4	4	0	47,590	1,90919	11,41
6	2	0	53,628	1,70763	18,28
4	4	4	59,227	1,55885	41,34
6	4	2	64,517	1,44321	19,71
8	0	0	69,583	1,35000	18,07
6	6	0	74,487	1,27279	3,08
8	2	2	74,487	1,27279	6,16
8	4	0	79,277	1,20748	4,41

Fig. 5.12 M_6C crystal structure simulation and diffraction data of some of the diffraction planes. M_6C density: 7.321 g/cm³. Wyckoff positions: 16d (C) and 96h (Fe).

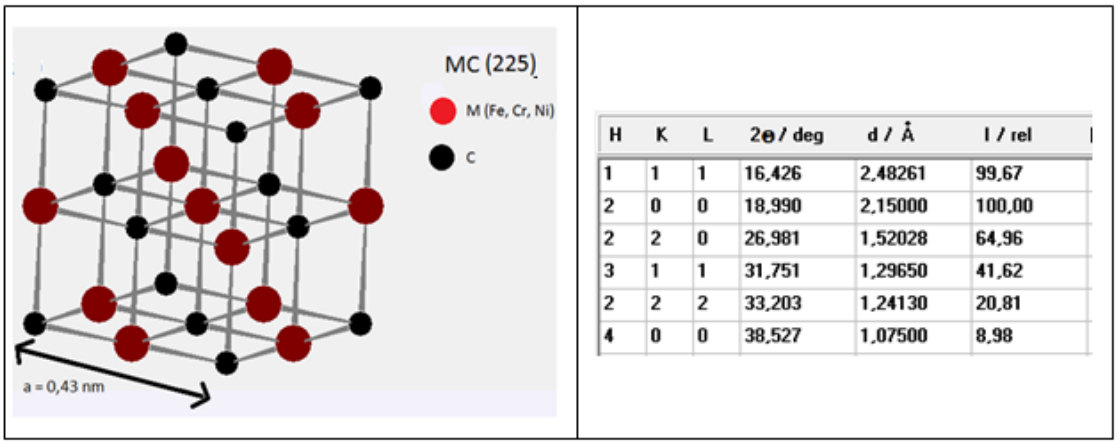

H	K	L	2ϑ / deg	d / Å	I / rel
1	1	1	16,426	2,48261	99,67
2	0	0	18,990	2,15000	100,00
2	2	0	26,981	1,52028	64,96
3	1	1	31,751	1,29650	41,62
2	2	2	33,203	1,24130	20,81
4	0	0	38,527	1,07500	8,98

Fig. 5.13 MC crystal structure simulation and diffraction data of some of the diffraction planes. MC density: 5.67 g/cm³. Wyckoff positions: 4a (C) and 4b (Fe).

The experimental data was determined from a set of SAD patterns as shown in Fig. 5.9. The diameter of each ring was measured at least three times to minimize the error and the mean value of these three measurements was used as the effective ring diameter. Equation 4.5 allows the determination of the interplanar distances corresponding to each diffraction ring. Table 5.2, Table 5.3 and Table 5.4 show the mean values of the ring diameters, 2g, and the interplanar distance, d, equivalent to each ring for the Au_{HF}, Au_{LF} and Ag irradiation cases, respectively.

Table 5.2 Au_{HF} irradiation diffraction data

Ring	2g (1/nm)	d (Å)
1	8.045	2.486
2	9.528	2.099
3	13.396	1.493
4	16.687	1.198
5	19.355	1.033

Table 5.3 Au_{LF} irradiation diffraction data

Ring	2g (1/nm)	d (Å)
1	7.972	2.508
2	9.353	2.138
3	11.769	1.699
4	13.422	1.490
5	13.917	1.437

Table 5.4 Ag irradiation diffraction data

Ring	2g (1/nm)	d (Å)
1	8.187	2.442
2	14.203	1.408

These measurements were then compared to the calculated data, shown in Figs. 5.11, 5.12 and 5.13. For this analysis, the following color code is used:

Color	Meaning
	Proof of the presence of the phase in the sample.
	There is a superposition of the ring with rings related to the phase whose presence was confirmed.
	There is no superposition with the phase whose presence is confirmed, but there is superposition with other possible phases.
	Rings that should appear, but don't.
	Exclusive ring of a single phase; it indicates the presence of the phase, but it is not a confirmation of its presence.
	The diffraction ring does not appear, but it is ignored due to its low relative intensity or due to the high value of d (d > 3.5 Å), which generates rings too close to the center of the diffraction pattern. They are hard to be detected because of the high intensity of the incident beam.

Table 5.5 shows the analysis and identification of the phases in the Au_{HF} irradiated sample. It is observed that of the five rings measured experimentally, all of them correspond to the rings predicted for the MC phase and there is no evidence of the presence of the $M_{23}C_6$ and M_6C phases, as there is no ring exclusive to them.

Table 5.5 Diffraction ring analysis of the Au_{HF} irradiated sample

fase	SG	parâmetro	hkl	d(A)	I (rel)	550 40 dpa			
						2g (1/nm)	d(A)	d(tab)-d(exp)	[d(t)-d(e)]/d(t)x100
M6C	227	10.8 A	220	3,82	100%				
			400	2,7	16.9%				
			422	2,204	42.8%	9,528	2,099	0,105	4,764
			440	1,91	11.41%				
			620	1,71	18.98%				
			444	1,56	11.41%	13,396	1,493	0,067	4,295
			642	1,443	19.71%	13,396	1,493	-0,05	-3,465
			800	1,35	18.07%				
			822	1,27	6,16%	16,687	1,198	0,072	5,669
			862	1,05	3.29%	19,355	1,033	0,017	1,619
M23C6	225	10.6 A	220	3,748	63,59%				
			311	3,19	100%				
			331	2,43	9.74%	8,045	2,486	-0,056	-2,305
			420	2,37	42.63%	8,045	2,486	-0,116	-4,895
			422	2,164	19.7%				
			333	2,03	80,05%	9,528	2,099	-0,069	-3,399
			440	1,87	16,08%				
			531	1,79	7,29%				
			600	1,76	30,81%				
			533	1,6	19.73%				
			444	1,53	7.16%	13,396	1,493	0,037	2,418
			711	1,48	10,14%	13,396	1,493	-0,013	-0,878
			640	1,46	8,22%	13,396	1,493	-0,033	-2,260
			731	1,38	13,28%				
			555	1,216	6,56%	16,687	1,198	0,018	1,480
			860	1,06	5,76%	19,355	1,033	0,027	2,547
MC	225	4.3 A	111	2,48	100%	8,045	2,486	-0,006	-0,242
			200	2,15	100%	9,528	2,099	0,051	2,372
			220	1,52	65%	13,396	1,493	0,027	1,776
			311	1,3	42%	16,687	1,198	0,102	7,846
			222	1,24	21%	16,687	1,198	0,042	3,387
			400	1,075	9%	19,355	1,033	0,042	3,907

Table 5.6 shows the analysis and identification of the phases in the Au_{LF} irradiated sample. In this case, what we observe is that the rings measured experimentally

correspond better to the rings predicted for the MC phase and there is no evidence of the presence of the $M_{23}C_6$ and M_6C phases, as there is no ring exclusive to them.

Table 5.6 Diffraction ring analysis of the Au_{LF} irradiated sample

fase	SG	parâmetro	hkl	d(A)	I (rel)	550 Au LF 40 dpa			
						2g (1/nm)	d(A)	d(tab)-d(exp)	[d(t)-d(e)]/d(t)x100
M6C	227	10.8 A	400	2,7	16.9%	7,972	2,508	0,192	7,111111111
			422	2,204	42.8%	9,353	2,138	0,066	2,995
			440	1,91	11.41%				
			620	1,71	18.98%	11,769	1,699	0,011	0,643274854
			444	1,56	11.41%	13,422	1,49	0,07	4,487
			642	1,443	19.71%	13,917	1,437	0,006	0,416
			800	1,35	18.07%				
			822	1,27	6,16%				
			862	1,05	3.29%				
M23C6	225	10.6 A	220	3,748	63,59%				
			311	3,19	100%				
			331	2,43	9.74%	7,972	2,508	-0,078	-3,210
			420	2,37	42.63%	7,972	2,508	-0,138	-5,823
			422	2,164	19.7%	9,353	2,138	0,026	1,201
			333	2,03	80,05%	9,353	2,138	-0,108	-5,320
			440	1,87	16,08%				
			531	1,79	7,29%				
			600	1,76	30,81%	11,769	1,699	0,061	3,466
			533	1,6	19.73%				
			444	1,53	7.16%	13,422	1,49	0,04	2,614
			711	1,48	10,14%	13,422	1,49	-0,01	-0,676
			640	1,46	8,22%	13,917	1,437	0,023	1,575
			731	1,38	13,28%				
			555	1,216	6,56%				
			860	1,06	5,76%				
MC	225	4.3 A	111	2,48	100%	7,972	2,508	-0,028	-1,129
			200	2,15	100%	9,353	2,138	0,012	0,558
			220	1,52	65%	13,422	1,49	0,03	1,974
			311	1,3	42%				
			222	1,24	21%				
			400	1,075	9%				

For the Ag case, only two diffraction rings were measured (Table 5.4). One d value agrees quite well to that from the (111) plane of the MC phase while the other one agrees better to the (731) plane of the $M_{23}C_6$ phase. We can infer that for the Ag irradiation case both phases could be present, but a better analysis is needed to confirm the nature of the precipitates formed.

The carbon content in the precipitates is significantly higher as compared to the matrix composition. In the MC phase, for example, the C content amounts 50 atomic %. The AISI 316L matrix, however, has a maximum amount of carbon of 0.14 atomic %, which may not be enough to supply the content present in the precipitates. This means that there must be a large amount of carbon atoms should be diffusively supplied from a larger volume, and not only from the layer of interest, which extends only to a depth of around 250 nm. This situation has been previously analyzed but for completeness of the text the results are also presented here [6,7].

If we consider the Au_{HF} irradiation case at 40 dpa for the Ar-implanted sample, we can estimate the amount of carbon in a certain volume in the sample. The histogram shown in Fig. 5.14 show the MC precipitates' mean size distribution in one of the analyzed micrographs.

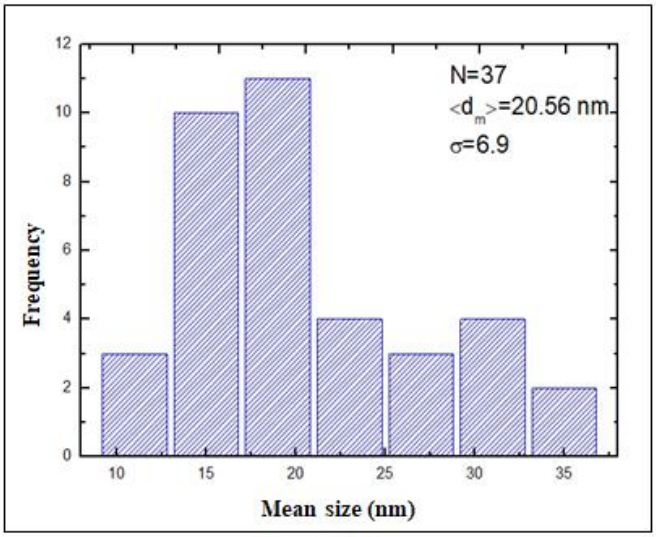

Fig. 5.14 Precipitate size distribution of the Ar-implanted sample irradiated to 40 dpa with Au_{HF}

Considering spherical precipitates with a mean radius of 10.28 nm it is possible to calculate the total volume occupied by the precipitates:

$$V_{MC} = N4\pi\frac{r_m{}^3}{3} = 37x4\pi\frac{10.28^3}{3} = 1.812x10^5\ nm^3,$$

where N is the total number of precipitates considered for the calculation and r_m is the mean radius. The surface contained in the micrograph is A = 131330,12 nm². The precipitates are distributed along the first 250 nm (which is the depth where Ar ions are

implanted). Thus, the matrix volume where the precipitates are observed is V_T = 3.283 x10^7 nm³. The volume fraction occupied by the precipitates in this range of depth within the matrix is given by

$$\frac{V_{MC}}{V_T} = \frac{1.812\ x\ 10^5}{3.283\ x\ 10^7} = 0.00552 = 55.2\%.$$

The unit cell volume of the MC phase $V_{MC}^{C.U} = 0.0795\ nm^3$, ($a_{MC}$ = 0.43 nm), with 2.28 x 10^6 MC unit cells in the total volume V_T. Each unit cell has four carbon atoms to four metallic atoms, because the MC phase is composed by two interlaced FCCs (Fig. 5.13). Thereby, the total number of C atoms contained in the MC precipitate is N_{MC}^{C} = 9.12 x 10^6 atoms.

Now, it must be verified if the amount of carbon present in the matrix is sufficient to combine with the metallic atoms and form the carbide precipitates. Considering that the number of unit cells of the matrix is given by:

$$\frac{V_T - V_{MC}}{V_{Matrix}^{U.C}} = \frac{3.283 \cdot 10^7 - 1.812 \cdot 10^5}{4.52 \cdot 10^{-2}} = 7.223 \cdot 10^8\ matrix\ unit\ cells,$$

and since the austenitic matrix is also from the 225 space group (FCC), the number of matrix atoms is $N_M = 2.89 \cdot 10^9$. Therefore the number of C atoms present in the matrix is $N_{C,M} = 0.0014 \cdot 2.89 \cdot 10^9 = 4.045 \cdot 10^6$, or 0.14 at.% only in 250 nm. This value is smaller than what is needed for the MC phase formation, meaning that for the MC phase to be completely supplied by C atoms these atoms must come from a depth of about 570 nm. The C diffusion coefficient in austenitic stainless steel for a temperature of 550 ºC (T = 823K) can be estimated by the equation given by Thibaux *et al.* [8]:

$$D = 1.23 \cdot 10^{-6} e^{-\frac{15050}{T}} \left[\frac{m^2}{s}\right] = 1.23 \cdot 10^{-6} e^{-\frac{15050}{823}} = 1.4 \cdot 10^{-14} \left[\frac{m^2}{s}\right].$$

The distance traveled by carbon in a steel matrix during a time interval of 6h (21600s), equivalent to the duration of the Au_{HF} irradiation experiment, is given by [9]:

$$x \cong \sqrt{Dt} = \sqrt{1.4 \cdot 10^{-14} \cdot 21600} \cong 1.743 \cdot 10^{-5} m\ \cong 17.43 \mu m,$$

which is a distance much larger than that predicted for the carbon supply in the depth of 250 nm. This means that, even though the matrix is poor in carbon, the precipitation of a second phase rich in carbon created in the region of interest is possible due to the diffusional supply of C atoms.

To further investigate the nature of the precipitates formed in the Au_{LF} and Ag irradiation cases, STEM-EDX measurements were realized. The elemental maps of the Ar-implanted samples irradiated to 40 dpa are shown in Figure 5.15 and Figure 5.16, respectively.

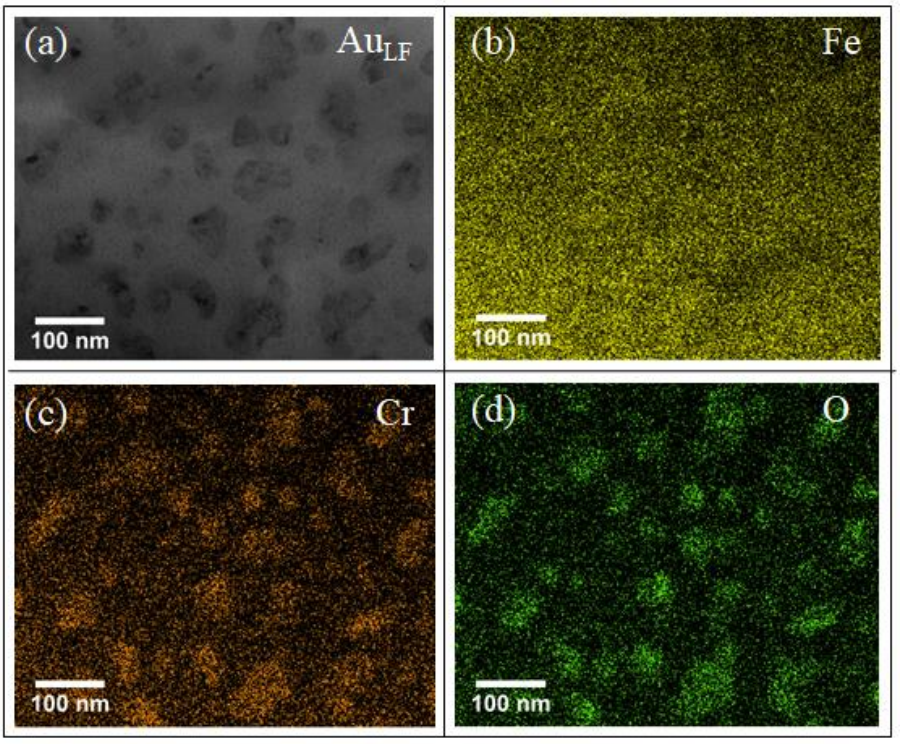

Fig. 5.15 STEM-EDX measurement of the (a) Au_{LF} irradiated sample with Ar showing the elemental maps for (b) Fe, (c) Cr and (d) O

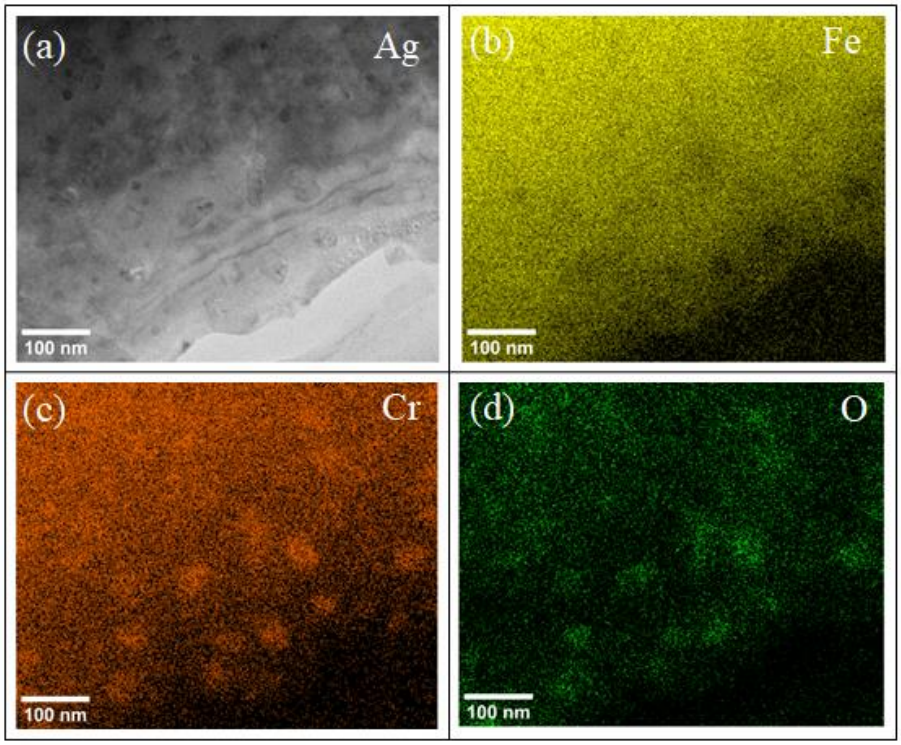

Fig. 5.16 STEM-EDX measurement of the (a) Ag irradiated sample with Ar showing the elemental maps for (b) Fe, (c) Cr and (d) O

From the STEM-EDX elemental maps it is clear that the precipitates formed after the irradiation experiments are rich in Cr and slightly depleted in Fe. The enrichment of Cr and depletion of Fe is characteristic of the metal-carbon phases described in Table 3.1 [5]. However, the EDX measurements show that the precipitates formed during these experiments are also rich in oxygen.

Cr and O-rich precipitates were shown to be formed in AISI 316L samples implanted with O after high temperature thermal annealings [10]. The crystallographic data of CrO is quite similar to that of the MC phase: both are FCC from the same space group (Fm-3m (225)) and their lattice parameters are a = 0.416 nm for CrO and a = 0.43 nm for MC.

Since we have not performed oxygen implantation in these samples, we must consider that its presence in our experiments might be resulted from surface contamination as the samples are exposed to the open atmosphere. Then, when the samples are submitted to ion irradiation, the oxygen atoms could be incorporated into the matrix, and a preferential gettering of O by the Cr-rich MC precipitates occurs by means of a heterogeneous nucleation process. The gettering of O atoms by the Cr-rich

precipitates can be a beneficial phenomenon, since the corrosion resistance of Cr-rich metals is due to the high reactivity of Cr with O. In fact, the solid-gas interface reaction between the two elements produces a thin layer of oxide on the steel surface, rending the oxygen non-reactive. This process is known as Cr passivity [11].

Another important aspect that must be taken into account on precipitate formation is that there was no precipitation in the sample without Ar irradiated with Au_{HF} ions (Fig. 5.3(a)). This fact may be an important indicator of an interdependence of vacancy saturation with the carbide precipitation mechanisms. Hence, to better understand the vacancy supersaturation effect as a function of the irradiation flux and ion mass, an analysis of the irradiation influence on the bubble growth is firstly performed in Section 5.3.2 to support the discussions about the precipitate formation in Section 5.3.3. This is done because the bubble and cavity growth processes are directly correlated with the absorption of vacancies as measured by the bubble sizes.

5.3.2 Influence of ion flux on Ar bubble growth

The irradiation flux and ion mass dependence on vacancy supersaturation can be directly correlated to the growth of bubbles as determined by the size distribution data as shown in Fig. 5.6. Figure 5.17 depicts graphically the values for the mean bubble sizes. The error bars correspond to the error of the mean value, defined as $\sigma/\sqrt{N}$ (where σ is the distribution standard deviation and N is the number of bubbles). This figure shows that the mean bubble sizes not only increase with the irradiation fluence, as expected, but also as a function of the flux and ion mass, which is clearly observed when comparing the data points for similar dpa values.

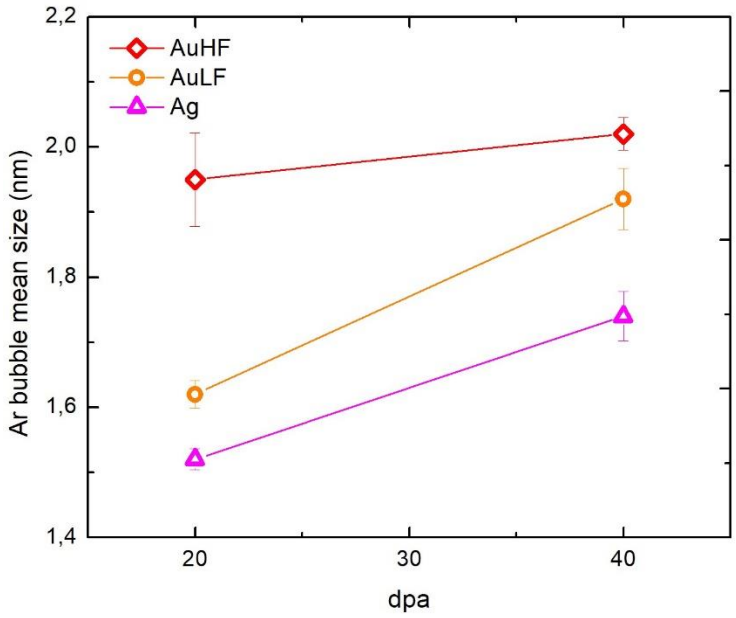

Fig. 5.17 Ar bubble mean size as a function of dpa for Au_{HF}, Au_{LF} and Ag ion irradiations

To discuss the ion irradiation effects on bubble growth it is important to remark that the Ar bubble system is formed by the thermal annealing procedure at 550 ºC/2h after the room temperature Ar implantation process. These two procedures are performed before the ion irradiation experiments. Hence, the effect of the irradiations must be considered on the bubble growth and not on the bubble nucleation process. The bubble growth induced by the thermal annealing treatment can be described either via migration and coalescence (MC), Ostwald ripening (OR), or by both mechanisms acting simultaneously [12]. Under the irradiation processes occurring at high temperature (550 ºC) the Ar bubble growth continues to occur, but now it can be considered that the migration and coalescence and/or OR processes for bubble growth are enhanced by the irradiation (radiation enhanced diffusion) [5].

It has been shown, however, that if we assume that the ion irradiation process affects only the atomic diffusivity behavior, the flux effect on the MC (migration and coalescence) or OR mechanisms can be neglected because the radiation enhanced diffusivities D_{RED} depend very weakly on the ion flux [13]. Therefore, a more consistent interpretation for the bubble growth behavior shown in Fig. 5.17 must be discussed. Bubbles are indeed vacancy sink sites that tend to absorb the excess vacancies from a supersaturated matrix solution. Hence, bubble growth occurs more prominently in

samples irradiated under HF conditions that cause the formation of a supersaturated vacancy solution. The vacancy supersaturation level influences the bubble growth process because it causes the increase of the vacancy chemical potential in the matrix, which intensifies the vacancy absorption process by bubbles. It is important to remark that the HF and LF irradiations were performed to the same dpa level. Hence, the distinct growth behavior is not determined by the total number of vacancies produced during the irradiation process (hence the same dpa), but by the efficiency in the vacancy absorption by the bubbles, which depends fundamentally on the differences in chemical potential. In this sense, the concept of vacancy supersaturation can explain both the irradiation flux effect on the bubble growth and the flux effect. These considerations are important to the discussion of the precipitate formation and growth in the next section.

5.3.3 Influence of vacancy concentration on the precipitate formation process

The characteristic atomic volume in the MC and $M_{23}C_6$ precipitates $\Omega_p \approx 0.99x10^{-2}$ nm^3 is smaller than the one for the austenitic matrix $\Omega_m \approx 1.16x10^{-2}$ nm^3. This means that precipitate nucleation and growth processes require the emission of vacancies and absorption of interstitial atoms to adjust the precipitate-matrix volume mismatch to reduce the strain energy of the matrix. An illustration representative of this concept is shown in Fig. 5.18.

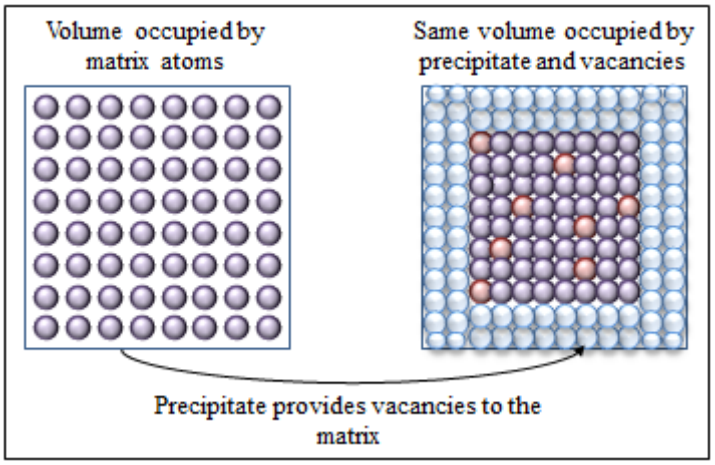

Fig. 5.18 Schematic representation of atomic value mismatch

The effective emission of vacancies by the precipitates can only occur if the matrix has a low concentration of vacancies. In other words, if the matrix is already supersaturated with vacancies, precipitate nucleation can be inhibited because the nucleation process would imply an excessive increase on the matrix free solution energy. The results presented in Figs. 5.4 and 5.5 for 20 and 40 dpa, respectively, show that precipitates are formed in all Ar-implanted samples. This is consistent with the concept that Ar bubbles are sink for vacancies and therefore avoid the formation of a supersaturated vacancy solution during the irradiation process.

For the samples not implanted with Ar, however, the irradiation flux and ion mass should play a role, since we observe precipitation in the low ion flux Au_{LF} and Ag_{LF} irradiated samples, but not in the sample irradiated with Au at a high flux (Au_{HF}).

When an ion impinges on a target sample, it produces a certain number of collision cascades and sub cascades. Within these collision events, vacancies are produced. The number of locally produced vacancies depends on the ion mass. For the same target, heavy ions tend to form denser collision cascades as compared to those produced by light ions (see, e.g., Fig. 3.4 in Chapter 3). As an example, simulations performed via the SRIM code predict that Au irradiation at 5 MeV produces a mean number of vacancies per ion $N_v^{Au} \approx 19000$, which is about 2 times larger than the mean number of vacancies per ion $N_v^{Ag} \approx 9000$ produced in an Ag irradiation at 3.5 MeV. In this sense, for the same flux and fluence, it is expected a smaller amount of excess vacancies for the lighter ion as can be detected by the bubble size measurements shown in Fig. 5.17. If it is assumed that the bubble sizes reflect the number of excess vacancies absorbed during the irradiation process, then we must consider that, during the irradiation, the vacancy supersaturation is indeed much higher for the high flux condition obtained by the Au_{HF} case. Consequently, precipitate nucleation should be more difficult under HF conditions. Hence, for sample not containing Ar bubbles, the irradiation flux effect may explain why precipitate have not formed in the Au_{HF} irradiation case and formed for the Au_{LF} and Ag_{LF} cases. In fact, the Ag_{LF} result is also impacted by the difference in ion mass, which also reflect the number of mean vacancies produced per ion mentioned above.

As opposed to the argument of vacancy supersaturation to explain the formation of precipitates, it can be also considered that, under high flux irradiation conditions, the

rate of precipitate nucleation could be matched by the rate of precipitate dissociation also caused by the irradiation. This would explain why precipitate formation occurs under low flux irradiations and not under high flux conditions. However, the results from the samples containing Ar bubbles, which show that for both, HF and LF irradiation conditions there is the formation of precipitates, plays in favor of the vacancy supersaturation argument.

Finally, it seems important to notice that studies on the dependence of defect evolution, amorphization and precipitation in semiconductors and metals considering the ion flux influence have been performed throughout the years [13–16]. These studies, however, are not conclusive on the sense that different behaviors are observed for each group of experiments, showing that the results are highly dependent on the material which is being analyzed and on the irradiation parameters used, including particle species, energy and fluence range of the irradiation beam. In all of them, however, considerations about vacancy production and annihilation rates are discussed. Notwithstanding, the results of the present study and their interpretation, comparing the behavior of direct observables quantities as bubble sizes and precipitate formation as a function of the ion mass and fluence the same target, provide a systematic and clear explanation for the heavy ion irradiation effects on the microstructure evolution in AISI 316 L alloys.

References

[1] S. Jublot-Leclerc, X. Li, L. Legras, M.L. Lescoat, F. Fortuna, A. Gentils, J. Nucl. Mater. 480 (2016) 436–446.

[2] A. Renault-Laborne, J. Malaplate, C. Pokor, B. Tanguy, Eff. Radiat. Nucl. Mater. 26th Vol. 74 (2014) 1–24.

[3] C. Sun, S. Zheng, C.C. Wei, Y. Wu, L. Shao, Y. Yang, K.T. Hartwig, S.A. Maloy, S.J. Zinkle, T.R. Allen, H. Wang, X. Zhang, Sci. Rep. 5 (2015) 7801.

[4] M.L. Jenkins, M.A. Kirk, Characterization of Radiation Damage by Transmission Electron Microscopy, IoP, Bristol and Philadelphia, 2001.

[5] G.S. Was, Fundamentals of Radiation Materials Science, Springer, 2007.

[6] Í.M. Oyarzabal, M.M. Timm, W.M. Pasini, F.S.M. Oliveira, F. Tatsch, L.

Amaral, P.F.P. Fichtner, in:, MRS Adv., 2018.

[7] Í. Oyarzabal, Efeitos Da Implantação de Ar e Da Irradiação Com Íons de Au Sobre a Formação de Precipitados Em Aço AISI 316L Como Revestimento de Combustível Nuclear, Universidade Federal do Rio Grande do Sul, 2017.

[8] P. Thibaux, A. Métenier, C. Xhoffer, Met. Mater. Trans. A Phys. Met. Mater. Sci. 38 (2007) 1169–1176.

[9] D.A. Porter, Phase Transformations in Metals and Alloys, 2009.

[10] G. Trindade, Formação e Estabilidade de Nanoaglomerados Óxidos No Aço AISI 316L, Universidade Federal do Rio Grande do Sul, 2019.

[11] W.D.J. Callister, Fundamentals of Materials Science and Engineering, 2001.

[12] H. Schroeder, P.F.P. Fichtner, J. Nucl. Mater. 179–181 (1991) 1007–1010.

[13] J.-H. Ke, E.R. Reese, E.A. Marquis, G.R. Odette, D. Morgan, Acta Mater. 164 (2019) 586–601.

[14] A. Claverie, A. Roumili, N. Gessinn, J. Beauvillain, Mater. Sci. Eng. B 4 (1989) 205–209.

[15] S.O. Kucheyev, H. Boudinov, J.S. Williams, C. Jagadish, G. Li, J. Appl. Phys. 91 (2002) 4117–4120.

[16] P. V. Zukovski, K. Kiszczak, D. Maczka, A. Latuszynski, Radiat. Eff. Defects Solids 132 (1994) 11–18.

CHAPTER 6

Ion implantation effects on $CrSi_2$ thin films

This chapter presents the ion implantation study in 280 nm thick $CrSi_2$ thin films. An investigation of the influence of microstructural changes induced by Al and Ne ion implantation on the electrical resistivity of amorphous $CrSi_2$ is performed. Al was chosen because it is an acceptor dopant for $CrSi_2$. Pan *et al*., for example, showed that the electrical resistivity of $CrSi_2$ decreases with increasing Al concentration for a temperature range of 300 – 700 K, while Perumal *et al*. showed that the introduction of Al and Mn as co-substitutors in $CrSi_2$ induces the decrease in both the electrical resistivity and thermal conductivity, leading to an enhancement of the figure of merit when compared to pure $CrSi_2$ [1,2]. On the other hand, inert gases have been used in ion implantation experiments in crystalline thermoelectric materials both to produce defects that saturate dangling bonds, increasing the electrical conductivity, and to serve as scattering centers for phonons, reducing the thermal conductivity. Ne was also chosen because it has less mobility than He ions, for example, and therefore does not tend to diffuse out of the sample even at high temperature implantations, as occurs for the case of He ions implanted in Si [3].

In summary, this chapter presents a study on the microstructural changes induced by ion implantation and their effect on the electrical resistivity. Results comparing non-implanted and implanted samples are discussed in terms of how the matrix responds to different damage levels introduced by ion implantation and how it can affect the charge and heat transport in amorphous thermoelectric materials.

6.1 Microstructure evolution

Figure 6.1 shows a cross-sectional TEM micrograph of the as-deposited $CrSi_2$ thin film. The image depicts also the Si substrate and the SiO_2 thin layer, of about 25 nm in thickness. The S arrow points to the $CrSi_2$ film surface, on which it was deposited a thin carbon layer and a Pt layer (darker contrast in the right) for TEM sample preparation using FIB (as explained in Chapter 4).

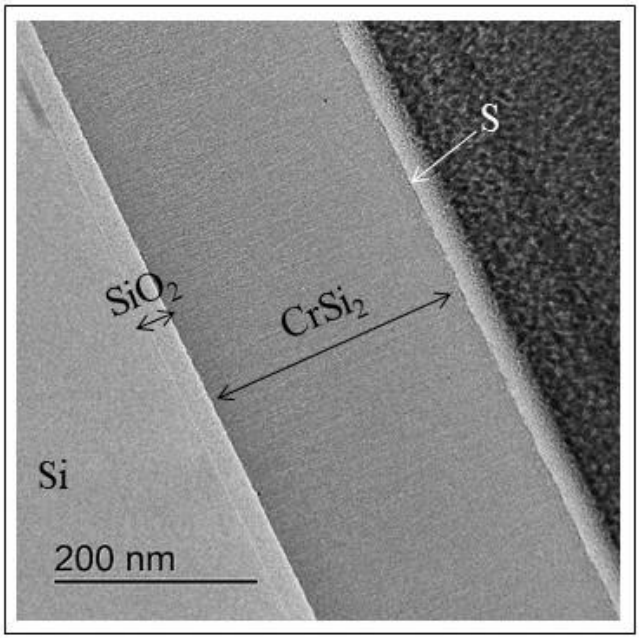

Fig. 6.1 As-deposited 280 nm thick $CrSi_2$ film on SiO_2/Si substrate

Fig. 6.1 presents linear features along the film indicating that the $CrSi_2$ thin film has a columnar structure. This is a known phenomenon in room temperature CVD depositions as predicted by the Thornton model in zone 1 [4]. This effect was also observed in previous studies on $CrSi_2$ [5].

The as-deposited $CrSi_2$ samples were characterized by Selected Area Diffraction (SAD) and Rutherford Backscattering measurements. Figure 6.2 (a) shows a characteristic RBS spectrum from the measurement set. The experimental data is well fitted by a SIMNRA code simulation (continuous line) considering the stoichiometric composition of the compound [6]. The SAD measurements (Fig. 6.2 (b)) show the characteristic diffuse rings of amorphous structures.

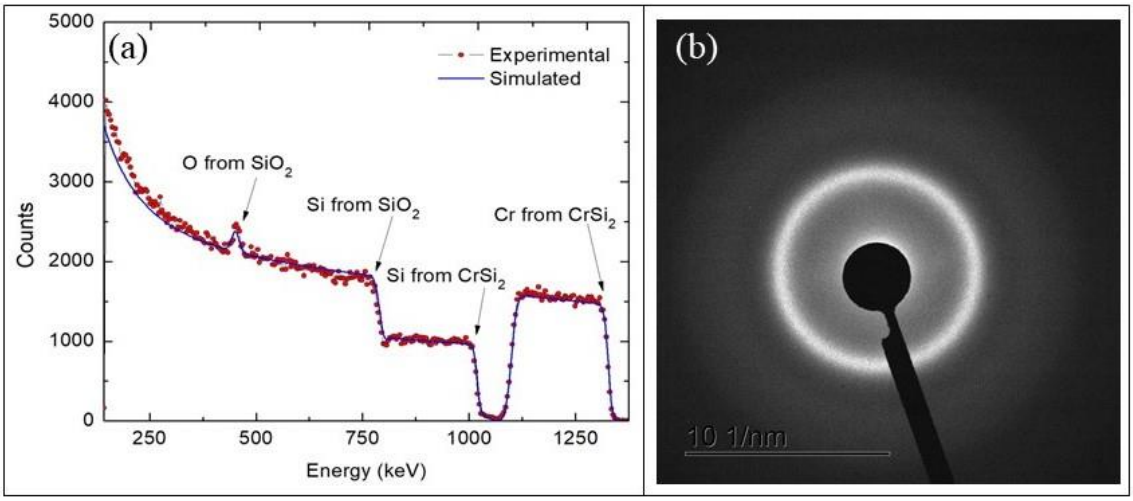

Fig. 6.2 (a) RBS spectrum and (b) diffraction pattern of pristine amorphous $CrSi_2$ samples

6.1.1 Room temperature implantations

In this subsection the results concerning Ne and Al ion implantations held at room temperature are presented. The Al implantations were performed with two different ion fluences to achieve a concentration of ≈ 0.008 at.% (typical doping concentration) in a sample denominated low concentration Al_{LC} and a concentration of ≈ 0.64 at.% in the sample denominated high concentration Al_{HC}. The fluence for the Al_{HC} sample was calculated to achieve the same damage level (about 13 dpa) as in the case of the Ne implantation (atomic concentration is of ≈ 1.0 at.%). The Al_{HC} experiments will be explored in more detail in the Discussions section. The concentration-depth profiles predicted by SRIM simulations for the Ne and Al_{LC} samples are shown in Fig. 4.5. Figure 6.3 shows the TEM micrograph of the room temperature Al_{LC} and Ne-implanted $CrSi_2$ samples.

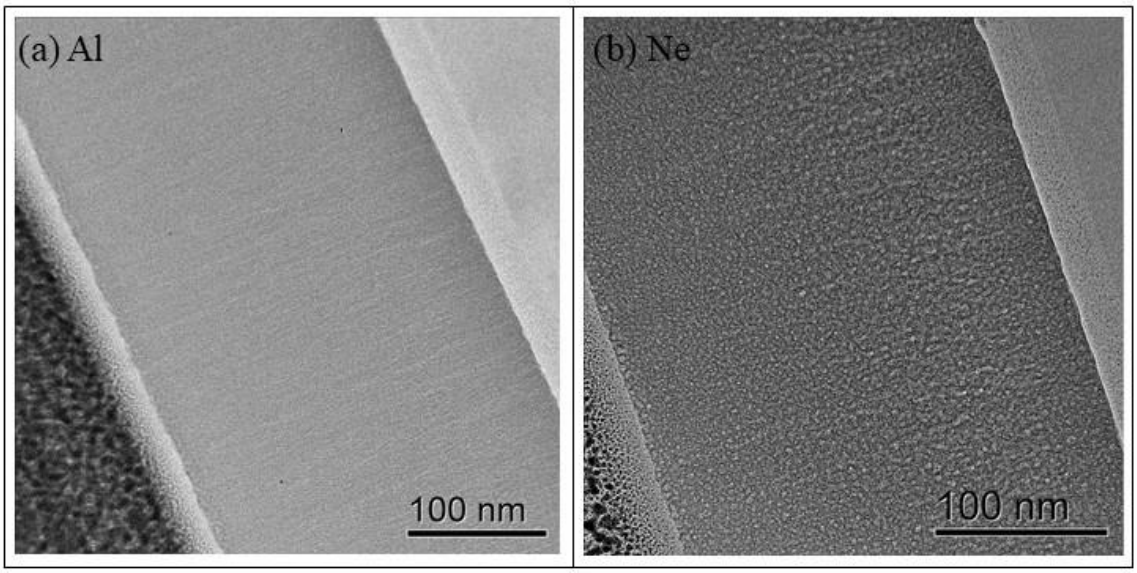

Fig. 6.3 $CrSi_2$ implanted at room temperature with (a) Al_{LC} and (b) Ne

The Ne implantation at room temperature triggered the formation of Ne bubbles all along the $CrSi_2$ film, following the columnar pattern. This can be clearly observed in Fig. 6.3(b) where the bubbles (bright field underfocus conditions) appear as white features surrounded by darker rings. It is important to notice that the images of the as-deposited (Fig 6.1) and Al-implanted (Fig. 6.3 (a)) samples are quite similar. This implies that there was no apparent modification in the $CrSi_2$ microstructure caused by the Al_{LC} implantation induced damage.

The presence of Al and Ne in the samples shown in Fig. 6.3 was assessed via STEM-EDX measurements. Figure 6.4 (a) and (b) shows the EDX signal superimposed with the SRIM concentration-depth profile simulation (dash-dotted line) for the samples implanted with Al and Ne, respectively. In this case, the STEM-EDX measurements was made with the electron beam from the TEM scanning the sample from one extremity to the other in a line, giving a signal of the element of interest as a function of distance/depth in the film. From the difference in the Al concentration-depth profile measured by EDX and predicted by the SRIM code in Fig. 6.4 (a) we can also infer that Al ions also have a similar atomic mobility behavior discussed for the Ne atoms.

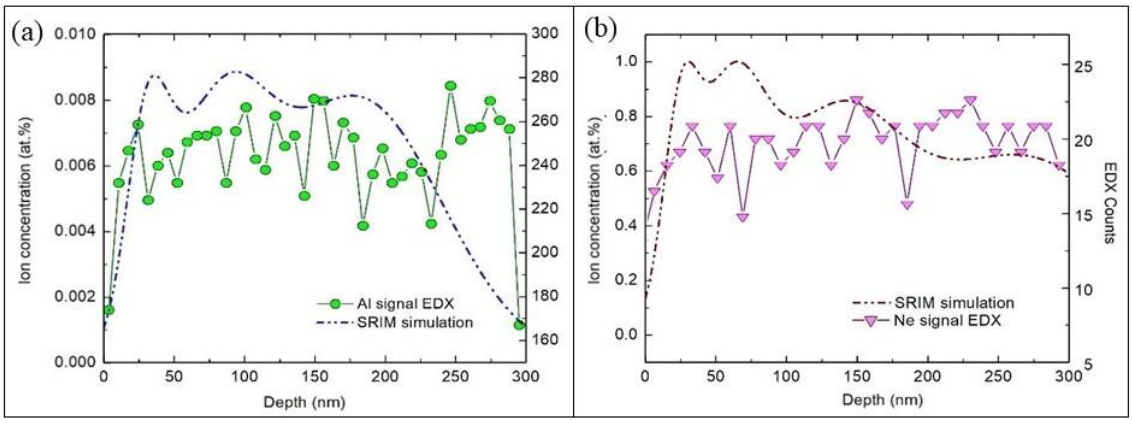

Fig. 6.4 EDX spectrum superimposed with SRIM ion concentration depth profile simulation for (a) Al_{LC} implantation and for (b) Ne implantation

The SAD patterns shown in Figure 6.5 indicate that after room temperature implantations with both Al and Ne ions the samples remain amorphous.

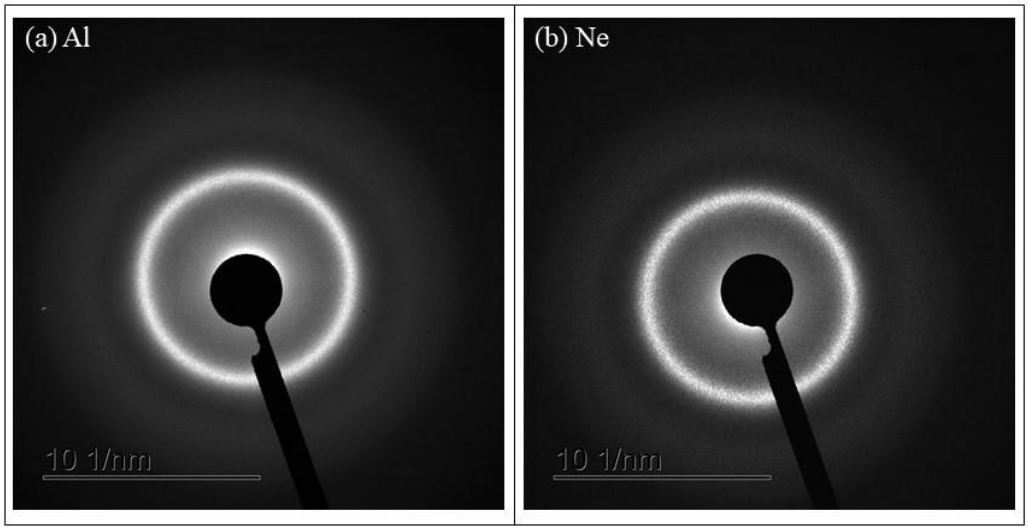

Fig. 6.5 SAD pattern of the $CrSi_2$ sample implanted at room temperature with (a) Al_{LC} and (b) Ne ions

6.1.2 Implantation at 250 ºC

Ne implantation was also performed with the substrate heated at 250 ºC. Figure 6.6 shows a TEM micrograph of the resulting microstructure. The micrograph clearly shows that Ne bubbles are present in the sample, but there are several different additional features that were not observed in the room temperature Ne implantation (Fig. 6.3 (b)). Structures presenting a darker contrast distributed along the $CrSi_2$ film, for example, are characteristic images of crystallites that are strongly diffracting the

electron beam (diffraction contrast imaging conditions). To confirm this interpretation, dark field images were taken from the same area shown in Fig. 6.6. The corresponding micrograph, together with SAD measurements are shown in Figure 6.7 (a) and (b), respectively.

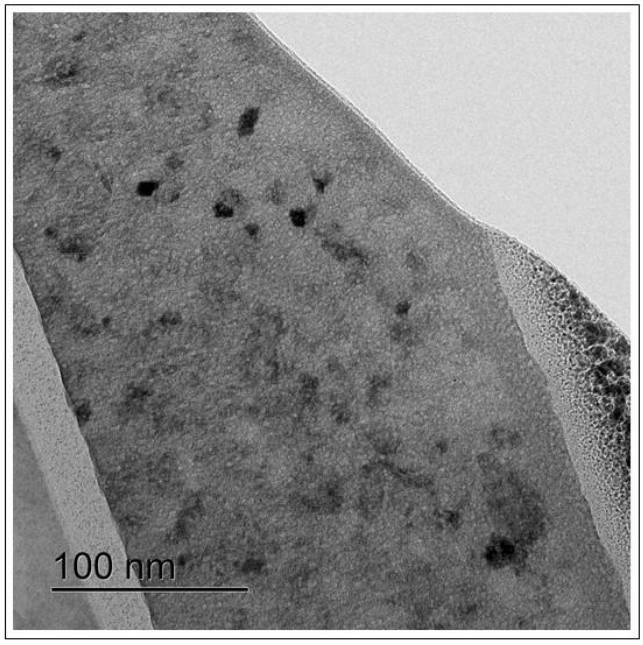

Fig. 6.6 TEM micrograph of the $CrSi_2$ sample implanted with Ne ions at 250 ºC

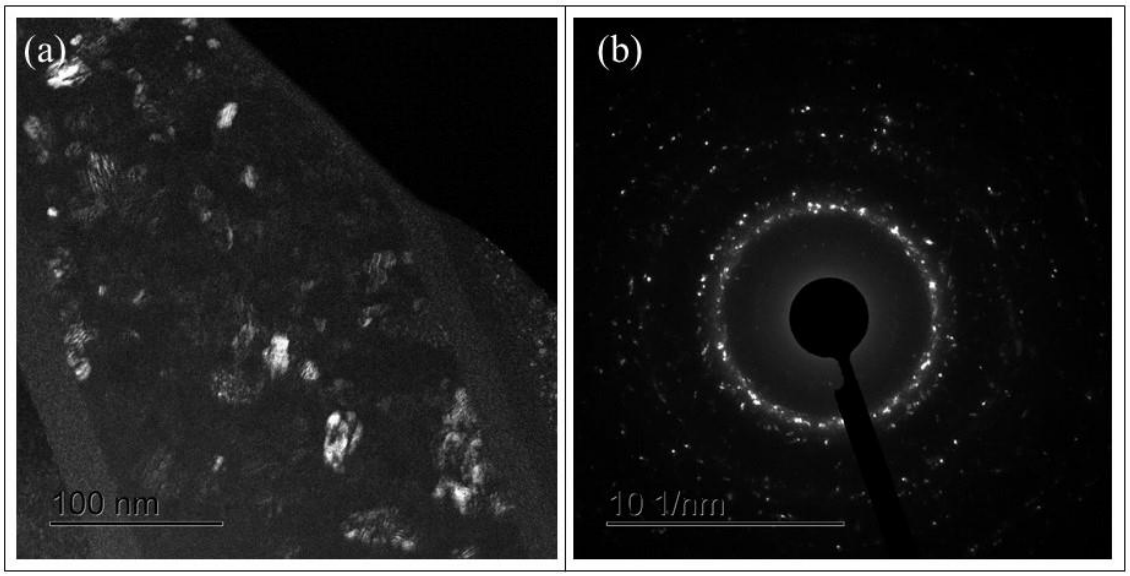

Fig. 6.7 (a) Dark-field TEM micrograph of the $CrSi_2$ sample implanted with Ne ion at 250 ºC and (b) SAD pattern of the same sample

The polycrystalline nature of the structure produced by the 250 ºC Ne implanted $CrSi_2$ sample is now clearly depicted. In Fig. 6.7 (a) the dark-field contrast is serving to light up only a subset of crystals that are Bragg-reflecting at a given orientation. This orientation was chosen by selecting a spot on the diffraction pattern shown in Fig. 6.7 (b). The several brilliant spots seen in the SAD pattern shows that this sample is composed by several nano-crystallites with sizes from 5 to about 30 nm randomly oriented, meaning that the heated implantation induced the crystallization of the $CrSi_2$ film.

The crystallization of amorphous $CrSi_2$ by thermal treatments is known to happen at a temperature of $\approx$ 327 ºC [7]. We have shown, however, that by means of ion implantation this limit can be reduced. This effect can be credited to a radiation-enhanced transformation process and also to the fact that the Ne bubbles and the columnar structures present in the film may act as inhomogeneous nucleation sites for the amorphous to crystalline phase transition [8,9].

Furthermore, the diffraction ring-pattern shown in Fig. 6.7 (b) allows the determination of the majoritarian phase formed during the experiment. In fact, the ring pattern is well fitted to the hexagonal structure of the $CrSi_2$ crystal lattice, with a space group $P6_222$, lattice parameters a = 4.42758 Å and c = 6.36805 Å, Wyckoff positions *3d* (Cr) and *6j* (Si) [10]. Figure 6.8 shows the diffraction pattern fitted to the $CrSi_2$ structure [10]. The (h,k,l) index of the rings is also presented in the figure.

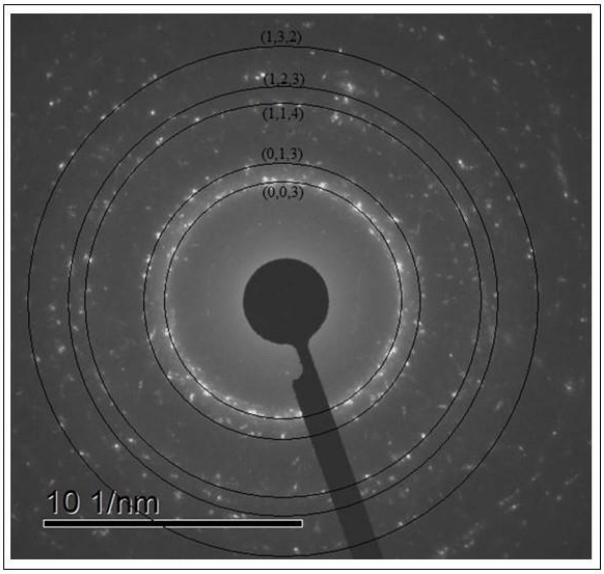

Fig. 6.8 SAD pattern of the $CrSi_2$ sample implanted with Ne ions at 250 ºC fitted to the crystalline structure of CrSi2 (SG $P6_222$, a = 4.42758 Å and c = 6.36805 Å, Wyckoff positions *3d* (Cr) and *6j* (Si))

The EDX measurement performed on this sample shows that Ne is distributed evenly throughout the thickness of the film (Figure 6.9), meaning that even at an implantation temperature of 250 ºC, Ne ions remained in the sample.

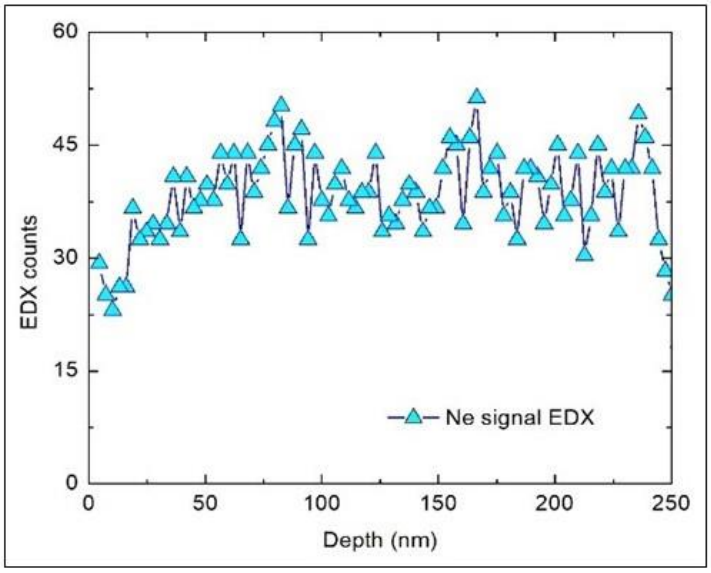

Fig. 6.9 (a) STEM-EDX spectrum showing the Ne signal of the $CrSi_2$ sample implanted with Ne ions at 250 ºC

6.2 Electrical resistivity

Another aspect that was explored on the study of ion implantation in $CrSi_2$ thin films was the response of its electrical properties to the experiments described above. As described in chapter 4, the electrical resistivity of non-implanted and implanted samples was assessed via Hall effect measurements. Figure 6.10 shows the electrical resistivity of these samples as a function of temperature.

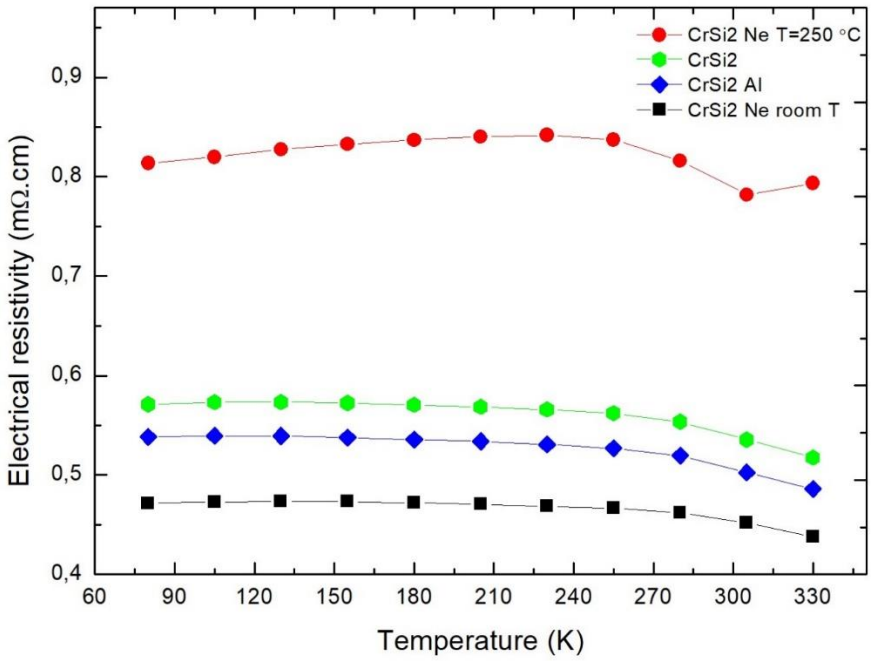

Fig. 6.10 Electrical resistivity measurements as a function of temperature of as-deposited and implanted $CrSi_2$ samples

The Al and Ne implantations performed at room temperature induced a decrease in resistivity as compared to the as-deposited sample, the three showing quite similar temperature dependences. Ne implantation at room temperature was the one that induced the most visible decrease in electrical resistivity. On the other hand, the Ne implantation at 250 ºC substantially increased the resistivity on $CrSi_2$. With these results we have shown that ion implantation can be used effectively to induce modifications on the charge transport in $CrSi_2$. In the next section, we will discuss how these modifications on electrical resistivity occur based on the microstructural changes exposed in Section 6.1 and on ion implantation parameters.

6.3 Discussion

The Al implantation was performed aiming to reproduce a typical doping concentration, since Al atoms are normally used as acceptor dopants for crystalline $CrSi_2$ [2]. Amorphous materials do not behave in the same way as their crystalline counterparts. From the electrical resistivity measurements shown in Fig 6.10, the decrease in electrical resistivity in the Al_{LC} sample (0.008 at.%) can be interpreted as if

the Al ions have induced the formation of more dangling bonds within the amorphous lattice, thus increasing the number of localized states.

On the other hand, the decrease in electrical resistivity is more pronounced for the Ne implanted sample. As an inert gas atom, Ne cannot behave as a dopant, but it can introduce point or small defect clusters that act as charge carriers. In fact, this argument has been previously presented, for example, by Saji *et al*., to explain a decrease in electrical resistivity observed in Bi_2Se_3 samples after H and He irradiation [11]. Another study conducted by Bala *et al*. also consider that the decrease in electrical resistivity for Ag implanted PbTe samples is caused by electrically active defects produced during ion implantation [12], and they correlate the decrease in resistivity to the implantation fluence: the higher the fluence, the higher the amount of defects generated that can be electrically active. Furthermore, Banwell *et al*. performed Ne, Ar and Xe irradiations in crystalline $CrSi_2$ and also obtained a considerable decrease in electrical resistivity [13]. They also explained the result in terms of an increase in free-carrier concentration that arises from completely ionized defects produced by the irradiation.

However, these studies were all performed in crystalline samples, different from our situation. We can generalize these considerations to an amorphous lattice and consider that the atomic displacements caused by the implantation process results in the formation of dangling bonds, that can facilitate the charge transport within the amorphous structure. Considering that this is in fact what happens after the ion implantation in amorphous solids, we can explain the resistivity reduction observed for both room temperature Ne and Al implantation cases using the same arguments, and we can even consider that the more pronounced reduction in electrical resistivity for the Ne implantation is due to the higher amount of defects introduced in the sample by this implantation when compared to the Al implantation. This difference can be measured by means of the amount of displacements per atom (dpa) induced by the impinging ions (as explained in Chapter 3). Figure 6.11 shows the dpa as a function of depth for Ne and Al implantations in $CrSi_2$ discussed until now.

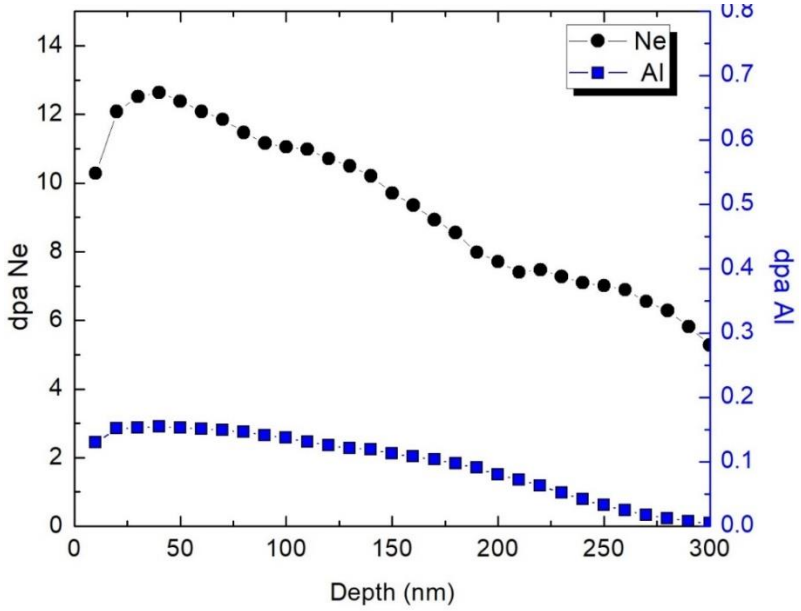

Fig. 6.11 dpa x depth for Ne (left axis) and Al (right axis) ion implantations

Ne implantation performed with the implantation energies and fluences shown in Table 4.3 in Chapter 4 produces about 80 times the amount of dpa of the Al implantation. To test if the difference on the electrical resistivity reduction depicted in Figure 6.10 between Al and Ne room temperature implantations is indeed due to the production of defects and not because of the ion species, a new experiment with Al implantation was performed. In this case, the Al ion fluences were increased in order to achieve about the same damage level induced by the Ne ion implantation (Figure 6.12). The new Al implantation parameters are shown in Table 4.4 in Chapter 4 (Al_{HC}). Besides, two Al implantations with these new values were realized, one at room temperature and another one at 250 ºC.

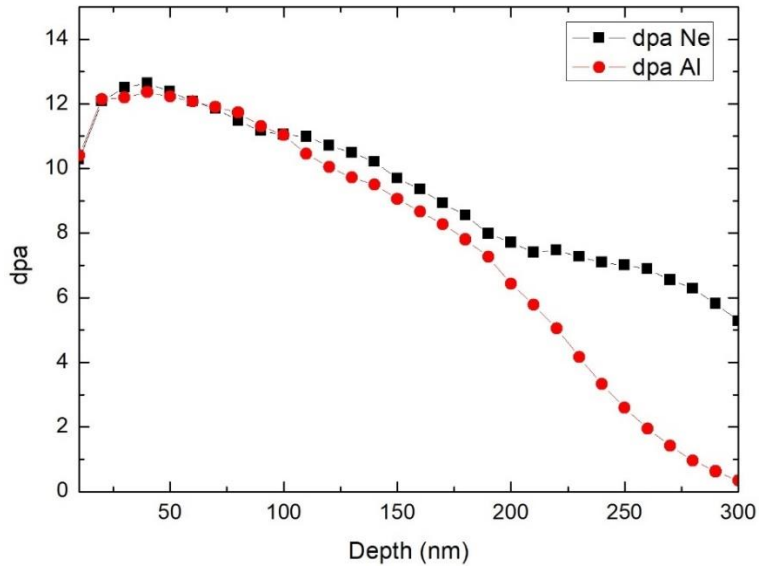

Fig. 6.12 dpa x depth for Ne and new Al ion implantations (Al_{HC})

After the implantations, these samples had their electrical resistivity tested in the same apparatus and conditions than the first implantations. Figure 6.13 shows these new measurements together with the results of the first implantation experiments.

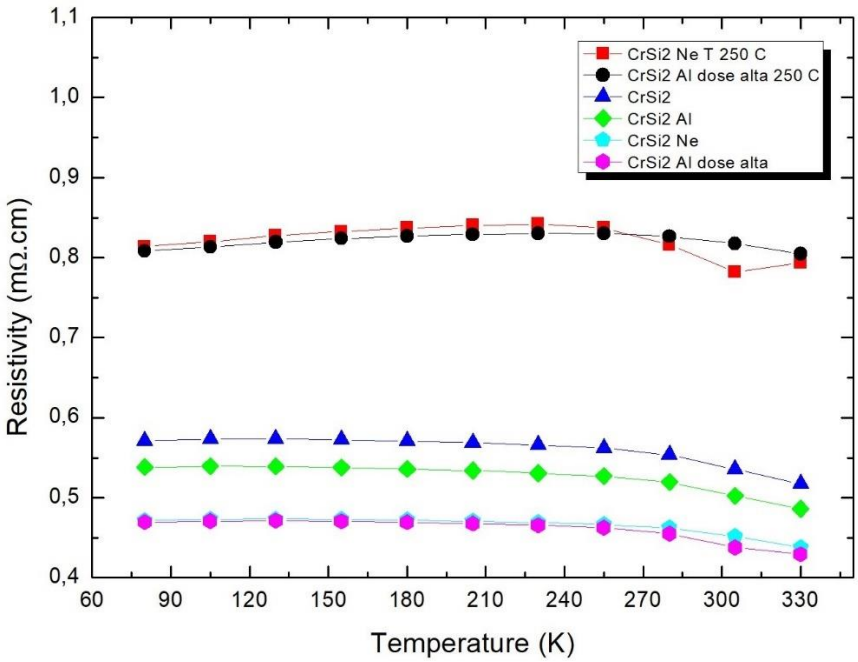

Fig. 6.13 Electrical resistivity measurements as a function of temperature of as-deposited and implanted $CrSi_2$ samples –with new Al implantations

The high dose Al implantations at room temperature and at 250 ºC give practically the same values of electrical resistivity of the Ne implantations. This

experiment shows that it is indeed the influence of ion implantation generated defects that contribute to the modifications on electrical resistivity in amorphous $CrSi_2$ thin films and not the capability of the ion species to participate more effectively as a "dopant" element.

The electrical resistivity measurements for both Ne and high dose Al implantations at 250 ºC show a significant increase in the resistivity values as compared with the as-deposited pristine film. Figure 6.6 shows that the Ne implantation causes the formation of a dense array of a randomly oriented nanocrystalline structures. The TEM microstructural analyses of the new Al implantations have not yet been performed. However, since the dpa profile is quite similar (Fig. 6.12), we can assume that the same recrystallization phenomena also occurred for the high Al fluence implantation case (Al_{HC} sample). This behavior can be explained considering that the formation of a nanocrystallites array introduces interfaces that can selectively scatter charge carriers. Furthermore, if the average size of the nanocrystals is comparable to the de Broglie wavelength of the carriers in the material, the crystallite can be regarded effectively as a point defect or point-like scattering center [14]. In the case of $CrSi_2$ samples, the de Broglie wavelength is $\lambda = 5$ nm, which is comparable to the average crystallite size obtained in our experiment with Ne implantation at 250 ºC.

The increase in electrical resistivity (which means a decrease in electrical conductivity) is not generally sought in studies about the enhancement of thermoelectric materials as it is considered a deleterious aspect to the increase in thermoelectric efficiency (see e.g. the discussion in Chapter 2). There are studies, however, that show that there can be an increase in the Seebeck coefficient related to the increase in scattering centers in $CrSi_2$ samples that pass from amorphous to (poly)crystalline state, reaching its maximum value at a crystallite size of 100 nm [7]. For example, Novikov *et al*. shows that nanocrystal interfaces in stoichiometric $CrSi_2$ thin films contribute largely not only to the increase of electrical resistivity, but also to the decrease of the thermal conductivity, thus causing the enhancement of the thermopower/Seebeck coefficient [14].

Besides, we must also consider that the implantation temperature increases the mobility of defects produced by Ne and Al ions and can induce their agglomeration. The increase in electrical resistivity occurs because these defect clusters reduce of the

mobility of the charge carriers. For example, it has been shown that deep-level related defects introduced by ion implantation in semi-conductors such as GaAs and GaN leads to the electrical and optical isolation required for the application of these materials in LEDs, semiconductor lasers and field effect transistors [15–17]. Uzan-Saguy *et al*. also credit the increase in electrical resistivity in *n*-type GaN by 11 orders of magnitude to the damage created by nuclear collisions after H and He implantation [18]. Moreover, Binari *et al*. report on the increase in resistivity in GaN due to defects formed during He implantation that can either trap or reduce the mobility of carriers [19]. In our case we assume, however, that it is the lattice disorder at the nanocrystallite-matrix interface regions the main cause for the increase on electrical resistivity. Although thermal conductivity has not been yet measured in the present study, we can speculate that the combination of the nanocrystallites and the Ne bubble could still imply on the improvement of the thermoelectric properties if the effects on phonon scattering provides a significant reduction on thermal conductivity, thus enhancing the σ/κ ratio. The same hypothesis could be applied for the 250 ºC Al implantation, although in this case no bubbles would be present and only the influence of the crystallites on thermal conductivity would be investigated. In fact, comparing the electric resistivity behavior from Ne and Al implantation it becomes clear that, for the same damage levels and same implantation temperature (Fig. 6.13), the presence of bubbles does not affect significantly the electrical resistivity. Nevertheless, since the bubbles represent a discontinuity on the solid structure of the matrix, they may act as efficient scattering centers for the phonons. Therefore, the phononic component of the thermal conductivity may also decrease, thus reducing the thermal conductivity and further increasing the thermoelectric figure of merit.

At this point, however, it seems worth to point out that there are some researches that consider that the lattice defects produced by ion implantation/irradiation processes cause the increase of the resistivity in semiconducting crystals. Recently, for example, Tureson *et al*. analyzed the influence of room temperature Mg implantation on the thermoelectric properties of ScN and they observed an increase in electrical resistivity and a decrease in thermal conductivity. They explain the increase in resistivity considering that the defects induced by the implantation process contribute to scatter the charge carriers causing a significant reduction in their mobility [20].

In the case of amorphous lattices, atomic displacements induced by ion implantation may not produce lattice defects acting as strong scattering centers for charge carriers, suggesting that the properties of amorphous thermoelectric materials can be more extensively tailored by means of ion implantation/irradiation processes. Their effective application, however, will strongly depend of the long-term thermal stability of the obtained structure.

To summarize, in this chapter we have shown the Al and Ne implantation effects on microstructure and electrical resistivity of $CrSi_2$ amorphous thin films. The results show that it is possible to induce significant changes on the electrical resistivity behavior of this material by means of a careful adjustment of implantation parameters, and that the microstructural changes can potentially affect another important aspect of thermoelectricity, the thermal conductivity.

References

[1] Z.J. Pan, L.T. Zhang, J.S. Wu, Effects of Al doping on the transport performances of CrSi2 single crystals, Scr. Mater. 56 (2007) 257–260. doi:10.1016/j.scriptamat.2006.10.027.

[2] S. Perumal, S. Gorsse, U. Ail, B. Chevalier, R. Decourt, A.M. Umarji, Effect of co-substitution of Mn and Al on thermoelectric properties of chromium disilicide, J. Mater. Sci. 48 (2013) 227–231. doi:10.1007/s10853-012-6732-4.

[3] E. Oliviero, S. Peripolli, L. Amaral, P.F.P. Fichtner, M.F. Beaufort, J.F. Barbot, S.E. Donnelly, Damage accumulation in neon implanted silicon, J. Appl. Phys. 100 (2006). doi:10.1063/1.2220644.

[4] J.A. Thornton, Influence of apparatus geometry and deposition conditions on the structure and topography of thick sputtered coatings, J. Vac. Sci. Technol. 11 (1974) 2–7. doi:10.1116/1.1312732.

[5] A. Moll, Elaboration et étude des propriétés thermoélectriques du disiliciure de chrome sous forme de monocristal, de couche mince et de nanofil, Université de Montpellier, 2018.

[6] M. Mayer, SIMNRA User's Guide, Rep. IPP 9/113, Max-Planck-Institut Für Plasmaphys. Garching, Ger. (1997).

[7] D.M. Rowe, ed., Thermoelectrics Handbook: macro to nano, Taylor & Francis Group, New York, 2006.

[8] G.S. Was, Fundamentals of Radiation Materials Science, Springer, 2007.

[9] D.A. Porter, Phase Transformations in Metals and Alloys, 2009. doi:10.1017/CBO9781107415324.004.

[10] T. Dasgupta, J. Etourneau, B. Chevalier, S.F. Matar, A.M. Umarji, Structural, thermal, and electrical properties of CrSi2, J. Appl. Phys. 103 (2008). doi:10.1063/1.2917347.

[11] A. Saji, S. Ampili, S.H. Yang, K.J. Ku, M. Elizabeth, Effects of doping, electron irradiation, H+ and He+ implantation on the thermoelectric properties of Bi2Se3 single crystals, J. Phys. Condens. Matter. 17 (2005) 2873–2888. doi:10.1088/0953-8984/17/19/005.

[12] M. Bala, A. Bhogra, S.A. Khan, T.S. Tripathi, S.K. Tripathi, D.K. Avasthi, K. Asokan, Enhancement of thermoelectric power of PbTe thin films by Ag ion implantation, J. Appl. Phys. 121 (2017). doi:10.1063/1.4984050.

[13] T.C. Banwell, X.A. Zhao, M.A. Nicolet, Effects of ion irradiation on conductivity of CrSi2 thin films, J. Appl. Phys. 59 (1986) 3077–3080. doi:10.1063/1.336931.

[14] S. V. Novikov, A.T. Burkov, Grain boundary scattering contribution to the thermopower in Cr-Si nanocrystalline films, J. Phys. Conf. Ser. 769 (2016). doi:10.1088/1742-6596/769/1/012069.

[15] A.V.P. Coelho, M.C. Adam, H. Boudinov, Deep levels fine structure in proton implanted p-type GaAs, J. Phys. D. Appl. Phys. 43 (2010). doi:10.1088/0022-3727/43/20/205104.

[16] D. Haase, M. Schmid, W. Kürner, A. Dörnen, V. Härle, F. Scholz, M. Burkard, H. Schweizer, Deep-level defects and n-type-carrier concentration in nitrogen implanted GaN, Appl. Phys. Lett. 69 (1996) 2525–2527. doi:10.1063/1.117727.

[17] S.O. Kucheyev, H. Boudinov, J.S. Williams, C. Jagadish, G. Li, Effect of irradiation temperature and ion flux on electrical isolation of GaN, J. Appl. Phys. 91 (2002) 4117–4120. doi:10.1063/1.1455154.

[18] C. Uzan-Saguy, J. Salzman, R. Kalish, V. Richter, U. Tish, S. Zamir, S. Prawer, Electrical isolation of GaN by ion implantation damage: Experiment and model, Appl. Phys. Lett. 74 (2002) 2441–2443. doi:10.1063/1.123874.

[19] S.C. Binari, H.B. Dietrich, G. Kelner, L.B. Rowland, K. Doverspike, D.K. Wickenden, H, He, and N implant isolation of n-type GaN, J. Appl. Phys. 78 (2002) 3008–3011. doi:10.1063/1.360712.

[20] N. Tureson, M. Marteau, T. Cabioch, N. Van Nong, J. Jensen, J. Lu, G. Greczynski, D. Fournier, N. Singh, A. Soni, L. Belliard, P. LEklund, A. e Febvrier, Effect of ion-implantation-induced defects and Mg dopants on the thermoelectric properties of ScN, Phys. Rev. B. 98 (2018) 1–9. doi:10.1103/physrevb.98.205307.

[21] H. Schroeder, P.F.P. Fichtner, On the coarsening mechanisms of helium bubbles

- Ostwald ripening versus migration and coalescence, J. Nucl. Mater. 179–181 (1991) 1007–1010. doi:10.1016/0022-3115(91)90261-5.

CHAPTER 7

Conclusions

In this work, we investigated the effects on the microstructure caused by ion implantation and ion irradiation in materials for nuclear and thermoelectric applications. Transmission electron microscopy observations, selected area diffraction and energy dispersive X-ray spectroscopy measurements were the main techniques used to analyze the microstructure modifications.

In the case of nuclear materials, a more basic understanding of the effects of heavy ion irradiation is still necessary to predict the materials stability in radiation harsh environments. The present study provides original experimental results and attempts to explain the atomic mechanisms involved on the development of precipitate reactions and growth of bubble systems. The investigations comprise the effects caused by Au and Ag irradiations in solution annealed AISI 316L austenitic stainless steel samples considered as a model case material for nuclear fuel cladding and reactor first wall. The samples were irradiated at 550 °C and their microstructure evolution was investigated as a function of irradiation flux and fluence for damage levels about 20 and 40 dpa. Comparing the microstructure evolution observed in pristine solution annealed samples with the behavior found in samples containing a dense array of small Ar bubbles (mean diameters around 1 nm), the experimental results and their interpretation allows for the following conclusions:

i) under high temperature (550 °C) heavy ion irradiation to a rather elevated damage level (20 or 40 dpa), carbide precipitation reactions lead to the formation of $M_{23}C_6$ and the majoritarian 1:1 metal-carbon (MC) phase rich in chromium, as properly characterized by SAD and EDX measurements;

ii) the MC precipitates are also rich in oxygen. The oxygen enrichment is explained considering the formation of 1:1 chromium-oxygen (CrO) compound presenting the same structure and a very similar lattice parameter of the MC structure. The oxygen supply occurs via radiation enhanced diffusion

process from the surface oxide layers produced when the samples are exposed to the open atmosphere;

iii) the precipitation reaction can be inhibited under high flux (HF) irradiation conditions, implying that a supersaturated solid solution of vacancies is produced;

iv) the presence of a dense array of bubbles in the matrix permits the formation of the MC precipitates even under HF conditions. The precipitation reaction occurs because the bubbles tend to absorb the excess vacancies and therefore vacancy supersaturation is not achieved;

v) as opposed to the high flux irradiation conditions, irradiations at low flux (LF) allows the development of precipitate reactions;

vi) the growth of bubbles is also influenced by the ion mass and flux. The bubble sizes increase with the fluence and, for the same damage level, also increase with the irradiation flux and ion mass. This is also explained assuming the build-up of supersaturated vacancy solid solutions which affects the chemical potential of the local bubble-matrix system. The results explaining the growth of the bubbles are consistent and reinforce the interpretation explaining the formation of the carbide precipitates.

In the case of thermoelectrics materials, the study also provides a set of original results on the ion implantation/irradiation effects influencing the microstructure and electrical resistivity of $CrSi_2$ amorphous thin films. The results obtained can potentially lead to the improvement of the thermoelectric energy conversion efficiency of amorphous films, a material with an interesting application niche in combination with photovoltaic devices. It was shown that Al and Ne implantations induced important modifications in the $CrSi_2$ electrical resistivity behavior. The study was conducted considering implantations at room temperature or at 250 ℃ at distinct energies and fluences to form a plateau-like concentration-depth profile to concentration levels of 0.008 at.% and 1 at.%. The results obtained and their interpretation lead to the following conclusions:

i) room temperature implantations of Al and Ne ions do not change the amorphous structure of the film but lead to the decrease in the electric

resistivity. This behavior is attributed to the production of electric active defects (dangling bounds) in the amorphous lattice, which increases the number of charge carriers in the conduction band similarly to the effect of doping.

ii) In the case of the Ne ion implantation, there is the formation of Ne bubbles. This occurs because, during the implantation, the implanted atoms are mobile due to radiation enhanced diffusion effects. The atomic mobility renders the agglomeration of Ne atoms at the free volumes within the columnar structure of the film caused by the deposition process. The presence of these bubbles does not affect the electric resistivity, which presents similar values of the Al implantation to the equivalent fluence.

iii) The formation of Ne bubbles within the amorphous lattice represents a promising point to be further explored. It does not affect the electric resistivity behavior but, as a discontinuity in the atomic lattice, it can lead to a phonon scattering processes decreasing the thermal conductivity **κ** and therefore further increasing the thermoelectric energy conversion efficiency.

iv) The Al implantation at room temperature introduces the same modification in the film resistivity as obtained by the Ne atoms. This means that the Al atoms are not behaving as dopants, but rather producing implantation induced electric active dopants.

v) Ne implantation at 250 ℃ causes the formation of a dense array of $CrSi_2$ crystallites with characteristic sizes from 5 to 20 nm. This recrystallization effect occurs in a temperature ≈ 80 ℃ less that the thermally induced amorphous to crystal transition temperature for bulk samples. The formation of the nanocrystallites causes the increase of the electric resistivity, an effect attributed to the electron scattering events at the amorphous-crystal interfaces. We speculate that, in spite of the increase of the resistivity **ρ**, the thermoelectric energy conversion efficiency may still increase since the decrease of **κ** can be larger and therefore overcompensate the increase of **ρ**.

In essence, the ion implantation experiments conducted in amorphous $CrSi_2$ films seems to open new ways to explore amorphous structures to tailor the electric and thermal

conductivities in materials with potential interest for thermoelectric applications.

Finally, both studies presented in this thesis still have many features that can be explored. The major difficulty in our study in AISI 316L is that we could only observe the final stages of the steel's microstructure after irradiation and, from this stage, try to dig out how the interactions between interstitials and vacancies occur in the event of a collision cascade. For the case of nuclear materials, for example, a deeper investigation about the vacancy production rate should be made. One option could be, for example, to investigate these systems by irradiations with intermediate ion fluences and other ion fluxes. Furthermore, this could also be achieved by means of the observation of the ion implantation induced modifications *in-situ*, which can be done, for example, with an ion implanter line connected to a TEM microscope. Even in that case, however, other ion irradiation parameters would have to be used other than the ones explored in this study, since there are few laboratories with ion beam techniques integrated with a TEM microscope providing the use of heavy ions and the possibility to perform TEM observations with sufficiently large magnification and resolution. Regarding the $CrSi_2$ study, the obvious next step is to analyze the thermal conductivity of the implanted samples and to test other implantation conditions, for example, high energy and high concentration implantations. More systematic TEM investigations on the Al_{HC} samples must also be performed. Moreover, the study on thermoelectricity should also be extended to other amorphous and crystalline silicon based materials and even silicon itself.

The studies presented in this thesis encompass only a small fraction of the possibilities offered by ion implantation experiments in materials for energy applications. In the recent years, great efforts are continuously being made by researchers of many fields trying to find emergency solutions for the energy production and storage problem. It was with this objective in mind that the investigations performed in the scope of this thesis were developed. Although we have not applied our experiments directly for the development of energy generation/storage devices, we expect that the studies here presented will contribute for future advances in basic physics research for the design of new efficient and resistant components for thermoelectricity and nuclear energy devices.

List of publications

1. Í. M. Oyarzabal, M. M. Timm, W. M. Pasini, F. S. M. de Oliveira, F. Tatsch, L. Amaral, P, F. P. Fichtner. Influence of Ar implantation on Precipitation in Au ion irradiated in AISI 316L solution annealed alloy. *MRS Advances*, vol. 3, Issue 31, 2018.

2. M. M. Timm, Í. M. Oyarzabal, F. Tatsch, L. Amaral, P. F. P. Fichtner. Au and Ag ion irradiation effects on the carbide precipitation and Ar bubble formation in solubilized AISI 316L alloys. *Nuclear Inst. And Methods in Physics Research B*, vol. 458, pp. 174-178, 2019.